ADSORPTION EQUILIBRIA AND MASS TRANSFER IN POROUS ADSORBENTS

By

Trenton Marcus Tovar

Dissertation
Submitted to the Faculty of the
Graduate School of Vanderbilt University
in partial fulfillment of the requirements
for the degree of

DOCTOR OF PHILOSOPHY
in

Chemical Engineering
May, 2016
Nashville, Tennessee

Approved:

M. Douglas LeVan, Ph.D.

Paul E. Laibinis, Ph.D.

Kenneth A. Debelak, Ph.D.

Eugene J. LeBoeuf, Ph.D.

To my wife and son

ACKNOWLEDGEMENTS

I'd like to thank Dr. LeVan for his guidance on this research as well as my labmates, Dushyant Barpage, Lucas Mitchell, and Tim Giesey, for help throughout my time at Vanderbilt. I'd also like to acknowledge Jared DeCoste, John Mahle, and Greg Peterson at the Edgewood Chemical Biological Center for helpful talks in our monthly teleconferences. I'd also like to thank my friends and family for their support and my wonderful wife, without whom this dissertation would not have been possible.

Funding for this research was from DTRA through ECBC.

TABLE OF CONTENTS

Page

LIST OF TABLES

LIST OF FIGURES

CHAPTER I

INTRODUCTION

Adsorption is an interfacial phenomenon in which intermolecular forces create a region near the surface in which the adsorbed fluid has different properties than the bulk fluid. This region is known as the adsorbed phase, and for solid adsorbents it is unique for each combination of adsorbate and adsorbent pair. The variation in the adsorbed phase between different adsorbates is the basis for many gas-phase separations including simple fixed-bed adsorption or more complex pressure-swing adsorption processes.

For adsorbent based separations, much of the research focuses on the synthesis, characterization, and application of porous adsorbents. Porous adsorbents represent a wide array of materials including activated carbons, clays, structured or amorphous silicas, metal oxides, aluminosilicate frameworks (zeolites), metal-organic frameworks (MOFs), or polymers. Many of these materials can be modified by metal impregnation or specific functional groups to enhance catalytic or sorption processes. Despite the variation in structure and composition, two critical properties for every adsorbent are adsorption equilibria and mass transfer rates, i.e., how much and how fast it can adsorb. Factors that can greatly influence these two properties include physical characteristics of the adsorbent, such as surface area and morphology, chemical properties that lead to strong intermolecular interactions between the adsorbent and a specific adsorbate, and operating conditions of the system. For the efficient design of adsorbent based separations, detailed knowledge of adsorption equilibria and mass transfer rates across a broad range of operating conditions is required.

Adsorption equilibria is defined as the quantity of molecules associated with a solid surface

that is in equilibrium with a bulk fluid phase. It is typically measured by adsorption isotherms in which loading is measured as a function of pressure at a constant temperature. Two ways of measuring adsorption isotherms are volumetric and gravimetric methods. In a volumetric system, a buffer region of known volume is charged with adsorbate gas to a desired pressure; a valve is then opened to expose a region containing an adsorbent sample, with free space predetermined by helium expansion, and allowed to equilibrate. Excess loading is calculated from the equilibrated pressure based on a gas law. Gravimetric systems expose an adsorbent sample to a desired gas pressure and calculate loading from the mass increase in the sample. Both methods are simple and accurate ways to measure adsorption equilibria.

Mass transfer in porous materials is a complex process. This is due to the presence of multiple mass transfer mechanisms that are dependent on adsorbent morphology. In very small micropores, defined as pores with a diameter below 2 nm, adsorbate molecules are always under the influence of forces from the adsorbent surface. As a result, intermolecular interactions and steric effects become the dominant forces for diffusion.[1] In large macropores, pores with diameter greater than 50 nm, surface forces play very little role and mass transfer is much more like bulk diffusion where collisions between adsorbate molecules typically occur more frequently than with the pore wall. In between 2 nm and 50 nm are mesopores; in this transitional area, surface forces are not yet dominant but collisions between the adsorbate and adsorbent surface occur more often resulting in Knudsen diffusion.

Many amorphous adsorbents, such as activated carbon, silica, or alumina, have wide pore size distributions that include micropores, mesopores, and macropores, and it is often difficult to determine the relative contribution of diffusion in each region. Well-ordered or crystalline adsorbents, such as zeolites, MOFs, or molecular sieves, usually have narrow pore size

distributions in the micropore region. However, these adsorbents are often synthesized in powder form, which is not desirable for industrial processes and requires pelletization that leads to bi-disperse adsorbents with macropore interstices between small microporous regions. This processing of adsorbents can also lead to damage of the outermost crystallites which may result in collapse or blockage of some pores, thereby reducing diffusivity across a thin layer and creating a barrier resistance.[1] For multi-component systems, in addition to diffusion mechanisms inside the particle, there is also the possibility of external resistance through a fluid film boundary layer between the particle surface and bulk fluid. Another complication to measuring diffusion rates is the impact from temperature gradients generated by heat of adsorption.

Given the complexities of mass transfer in porous adsorbents, a myriad of experimental techniques have been developed to measure diffusion rates. These methods include NMR,[2] quasi-elastic neutron scattering,[3] uptake rates,[4] chromatography,[5] differential adsorption bed,[6] zero-length column,[7] and frequency response.[8-10]

Frequency response, which is used in this dissertation, is a perturbation technique which introduces small, typically sinusoidal, oscillations around the equilibrium set point of a system variable. The response of a second variable is measured, and rate data can be extracted through a mathematical model. As the periodic measurements are not dependent on initial conditions, experimental error is reduced and data are highly reproducible. Frequency response is a powerful technique as it introduces an additional degree of freedom, since measurements can be taken over a range of frequencies, which helps decouple the impacts of multiple diffusive mechanisms, allowing for determination of a rate-limiting mass transfer mechanism.

The first frequency response technique was a batch technique developed by Yasuda[8] in which the system volume was perturbed and the corresponding pressure change was measured.

Volume-swing frequency response (VSFR) has been used to study adsorption, diffusion, and reactions.[8,11,12] Heats of adsorption have been shown to impact diffusion measurements and result in bimodal response curves.[13] Detailed models for both isothermal and non-isothermal conditions for VSFR have been developed.[14] Flow through techniques, such as pressure-swing frequency response (PSFR) and concentration-swing frequency response (CSFR), can help mitigate heat effects. PSFR introduces a pressure perturbation in an adsorption bed and measures the corresponding change in flow rate.[9] CSFR introduces an inlet stream to an adsorption that has constant total flow rate but with a sinusoidal concentration swing and the response variable is the concentration of the effluent stream.[10] General models to describe various mass transfer mechanisms have been developed for both flow through techniques.[15]

The focus of this research is to apply fundamental adsorption principles in the measurement and understanding of adsorption equilibria and mass transfer for specific applications of interest. Chapter 2 uses CSFR to measure diffusion rates of a series of C_{10} hydrocarbons in BPL activated carbons. The C_{10} adsorbates have different ring, branched, and bridging structures that may lead to steric effects on diffusion in the micropores of an amorphous adsorbent. Previously, shape-selective separations had only been shown in well-ordered materials where size exclusion created molecular sieving effects.[16] In amorphous adsorbents with wide pore size distributions, only impacts of increasing carbon number, thereby adding additional intermolecular interactions, had been shown to greatly affect diffusion.[17] Adsorption isotherms are also measured using gravimetric methods and used to analyze concentration dependent diffusivities using the Darken theory.

Chapter 3 uses CSFR to measure diffusion rates of CO_2 in large single crystals of a MOF, Cu-BTC. Traditional synthesis methods of Cu-BTC create micron size crystals in a powder form.

This leads to very fast uptake rates that make accurate diffusion measurements difficult. Slowing uptake by creating pellets only leads to the measurement of macropore diffusion,[18] which is affected by macroscopic properties of the pellet and not microscopic properties of the MOF pores. A new synthesis was used to generate millimeter size single crystals of Cu-BTC. The orders of magnitude increase in the diffusion length scale allows for much more accurate measurement of diffusion coefficients. Furthermore, the single crystal morphology guarantees that measured diffusion rates are from diffusion in the micropores of the MOF.

Chapter 4 uses CSFR to measure diffusion rates in a series of UiO-66 pellets. Unlike many MOFs, UiO-66 is extremely stable. It is also easily functionalized which has led to interest in its use as an adsorbent for gas-mask filters. The impact of pelletizing on diffusion properties is studied for pellets pressed at different pressures with varying thicknesses. The impact of amine functionalization of the UiO-66 pellets is also explored for adsorption of CO_2 and ethane.

Chapter 5 uses a volumetric apparatus to explore the potential of several MOFs for the storage of oxygen. High pressure oxygen storage may cause safety concerns; therefore, it is desirable to maintain oxygen tank capacity while reducing pressure. Tanks filled with an adsorbent can accomplish this, but it is desirable to find the best candidate for this application. Oxygen isotherms for several MOFs are measured up to 140 bar to determine the adsorbent working capacity. These results are compared to similar isotherms measured on an activated carbon and a zeolite. Heats of adsorption arre calculated from isotherms measured at different temperatures. Stability of the MOFs under high pressure oxygen is tested after multiple adsorption and desorption cycles.

Chapter 6 discusses the synthesis of an adsorbent for use as a CO_2 scrubber under water saturated conditions. An alternative to gas masks that filter the surrounding air is a closed-loop

rebreather apparatus that recycles the users exhaled oxygen. To prevent the lethal build-up of CO_2, a scrubber must be used to remove the CO_2. There are several obstacles for an effective CO_2 adsorbent in this type of system; the adsorbent must have high capacities at low CO_2 partial pressures, work at low temperatures with minimal heats of adsorption, and maintain capacities at 100% relative humidity. A novel adsorbent that deposits LiOH inside the pores of highly porous carbons was tested for CO_2 capacity using a breakthrough apparatus to simulate conditions in a tactical rebreather.

Finally, Chapter 7 summarizes the major conclusions of this work and provides recommendations for future research.

Much of the work throughout this dissertation is the result of collaborative research efforts. This includes collaborators from industry, academia, and government facilities. Contributions from different collaborators will be described in detail in the introductions of each chapter and any data from these sources that is presented in this dissertation will be acknowledged.

References

1. Karger, J.; Ruthven, D. M.; Theodorou, D. N. *Diffusion in Nanoporous Materials*. Weinheim: Wiley-VCH, **2012**.
2. Mair, R. W.; Wong, G. P.; Hoffman, D.; Hurlimann, M. D.; Patz, S.; Schwartz, L. M.; Walsworth, R. L. Probing porous media with gas diffusion NMR. *Phys. Rev. Lett.* **1999**, 83, 3324-3327.
3. Jobic, H.; Bee, M.; Caro, J.; Bulow, M.; Karger, J. Molecular self-diffusion of methane in zeolite ZSM-5 by quasi-elastic neutron scattering and nuclear magnetic resonance pulsed field gradient technique. *J. Chem. Soc., Faraday Trans.* **1989**, 85, 4201-4209.
4. Barrer, R. M.; Clarke, D. J. Diffusion of some n-paraffins in zeolite A. *J. Chem. Soc., Faraday Trans.* **1974**, 70, 535-548.
5. Haynes, H. W.; Sarma, P. N. A model for the application of gas chromatography to measurements of diffusion in bidisperse structured catalysts. *AIChE J.* **1973**, 19, 1043-1046.
6. Yang, R. T.; Chen, Y. D.; Yeh, Y. T.; Prediction of cross-term coefficients in binary diffusion: Diffusion in zeolite. *Chem. Eng. Sci.* **1991**, 46, 3089-3099.
7. Brandani, S.; Jama, M.; Ruthven, M. D. Diffusion, self-diffusion and counter-diffusion of benzene and p-xylene in silicalite. *Micropor. Mesopor. Mater.* **2000**, 35, 283-300.
8. Yasuda, Y. Determination of vapour diffusion coefficients in zeolite by the frequency response method. *J. Phys. Chem.* **1982**, 86, 1913-1917.
9. Wang, Y.; Sward, B. K.; LeVan, M. D. New Frequency Response Method for Measuring Adsorption Rates via Pressure Modulation: Application to Oxygen and Nitrogen in a Carbon Molecular Sieve. *Ind. Eng. Chem. Res.* **2003**, 42, 4213-4222.

10. Wang, Y.; LeVan, M. D. Mixture Diffusion in Nanoporous Adsorbents: Development of Fickian Flux Relationship and Concentration-Swing Frequency Response Method. *Ind. Eng. Chem. Res.* **2007**, 46, 2141-2154.
11. Yasuda, Y. Frequency response method for study of the kinetic behavior of a gas-surface system. 2. An ethylene-on-zinc oxide system. *J Phys Chem.* **1976**, 80, 1870–1875.
12. Yasuda, Y. Frequency response method for study of the kinetic details of a heterogeneous catalytic reaction of gases. 1. Theoretical treatment. *J Phys Chem.* **1993**, 97, 3314–3318.
13. Sun, L. M.; Meunier, F. On the heat effect in measurements of sorption kinetics by the frequency response method. *Chem Eng Sci.* **1993**, 48, 715–722.
14. Jordi, R. G.; Do, D. D. Analysis of the frequency response method applied to non-isothermal sorption studies. *Chem Eng Sci.* **1994**, 49, 957–979.
15. Wang, Y.; LeVan, M. D. Master Curves for mass transfer in bidisperse adsorbents for pressure-swing and volume-swing frequency response methods. *AIChE J.* **2011**, 57, 2054-2069.
16. Huddersman, K.; Klimczyk, M. Separation of Hexane Isomers on Zeolites Mordenite and Beta. *J. Chem. Soc., Faraday Trans.* **1996**, 92, 143-147.
17. Do, H. D.; Do, D. D.; Prasetyo, I. On the surface diffusion of hydrocarbons in microporous activated carbon. *Chem. Eng. Sci.* **2001**, 56, 4351-4368.
18. Liu, J.; Wang, Y.; Benin, A. I.; Jakubczak, P.; Willis, R. R.; LeVan, M. D. CO_2/H_2O Adsorption Equilibrium and Rates on Metal-Organic Frameworks: HKUST-1 and Ni/DOBDC. *Langmuir* **2010**, 26, 14301-14307.

CHAPTER II

STERIC EFFECTS ON THE DIFFUSION OF C_{10} HYDROCARBONS IN BPL ACTIVATED CARBON

2.1 Introduction

Adsorption of organic compounds is critical for various applications. Filtration of pollutants from both air and water is a major concern, while separation and purification of organic compounds is of vital importance to many industrial processes. Regardless of application, knowledge of adsorption capacities and diffusion rates is required for the efficient design of any adsorbent-based separation system. These parameters vary greatly depending on both the adsorbate and adsorbent being studied.

Branching and cyclic moieties in organic molecules can introduce steric effects that have a large impact on diffusional properties in some microporous adsorbents. These steric effects have been well studied in adsorbents that contain well-ordered pore structures with a narrow pore size distribution such as zeolites or carbon molecular sieves. Denayer et al.[1] used chromatographic techniques to study diffusion of branched C_5-C_8 alkanes on zeolite beta, ZSM-5, ZSM-22, zeolite Y, and mordenite. Results showed competitive or selective adsorption depending on zeolite type and showed that linear alkanes could be separated using columns of ZSM-22 and beta zeolites. Huddersman and Klimczyk[2] found that hexane isomers could be separated by the zeolite mordenite. Jobic et al.[3] used pulsed field gradient NMR and zero-length column techniques to measure n-alkane transport in zeolite 5A, finding that diffusivities decreased as carbon number increased. In a carbon molecular sieve, Laredo et al.[4] found that higher degrees of branching in

octane isomers increased mass transfer rates.

While shape selective separations in well ordered-adsorbents has been well studied, far fewer studies have investigated steric effects on diffusion in adsorbents that are amorphous and have a wide pore size distribution, like activated carbon. Do[5] has studied hydrocarbon diffusion in activated carbons noting that diffusion could occur along two separate pathways, through graphite-like microcrystalline structures or between spaces in the graphitic units. It was found that diffusion through the graphite layers is more important for larger alkanes. In addition to impacts of various diffusion mechanisms, Mangun et al.[6] showed that pore size distribution in a series of air activated carbon fibers can have a large impact on adsorption capacities of different linear alkanes and with larger pore sizes leading to higher uptake rates of n-butane. Jimenez-Cruz et al.[7] studied diffusion of n-heptane and the branched 2-methylheptane in activated carbon prepared by pyrolysis of the polymer PVDC. The two compounds could be separated by inverse gas chromatography but the slower diffusion of 2-methylheptane was attributed to an increase in carbon number, and additional van der Waals interaction with the carbon and not due to steric effects from branching.

Recently Wang et al.[8] used concentration swing frequency response to measure diffusion rates of linear alkanes in BPL activated carbon. They found a monotonic decrease in diffusion coefficient as carbon number increases. The diffusion coefficients also had a strong concentration dependence; a similar trend was seen by Do.[9] In addition to the series of linear alkanes, diffusion of the two C_{10} molecules 2,7-dimethyl octane and cyclodecane were compared with decane. When normalized by gas phase concentration, the branched and cyclic compounds showed no decreases in diffusion rate due to steric effects.

The purpose of this work is to expand upon the study of Wang et al.[8] by using concentration

swing frequency response to measure diffusion rates of different C_{10} adsorbates on BPL activated carbon to explore steric hindrance effects in amorphous adsorbents. The adsorbates chosen were α-pinene, decalin, and limonene, which have different degrees of branching or cyclic moieties; detailed chemical structures are described later. The fluorocarbon, perfluorodecalin was also investigated. By focusing solely on C_{10} hydrocarbons, the effect of carbon number is eliminated as a variable, which permits focus on the effect of molecular shape. To the best of our knowledge, this is the first such study of purely adsorbate structure on diffusion rate in an amorphous adsorbent.

The work performed in this chapter was done in collaboration with researchers at the Edgewood Chemical Biological Center (ECBC). Adsorption isotherms for the C_{10} molecules on BPL activated carbon were measured by John Mahle at ECBC. Density functional theory (DFT) simulations were performed by Craig Knox at ECBC to optimize molecular geometries and obtain molecular descriptors for quantitative structure-activity relationship (QSAR) correlations to measured diffusion coefficients. Diffusion measurements were performed at Vanderbilt.

2.2 Experiments and data analysis

2.2.1 *Materials*

The adsorbent used in this study was BPL activated carbon (Calgon Carbon Corp., lot no. 4814-5) in 6x16 mesh form with particle diameters of approximately 2 mm. It has a surface area of ~1000 m^2/g and is predominantly microporous with pore sizes ranging from 5-25 Å. Research grade helium from Air Liquide was used as a carrier gas. Decane (99%), α-pinene (98%), r-limonene (97%), a mixture of cis- and trans-decalin (>99%), and a mixture of cis-and trans-perfluorodecalin (95%) were used as received from Sigma Aldrich.

2.2.2 *CSFR measurements*

Figure 2.1 shows a schematic of the CSFR apparatus. Before exposure to each adsorbate, 25 mg of adsorbent was regenerated at 250 ºC under vacuum for 8 hours. After regeneration, the adsorbent was placed in the adsorbent bed under vacuum at room temperature with a 1 sccm He flow drawn through the bed for 16 hours. The liquid hydrocarbon was loaded into two sparger vessels in series that were placed in a temperature controlled water bath. A helium stream flowed through the sparger vessels with the pressure controlled by a MKS Baratron type 640 pressure controller to generate a saturated adsorbate feed stream. A second helium stream was mixed with the adsorbate feed stream prior to the adsorbent bed. The adsorbate gas concentration fed to the adsorbent bed was determined by the combined flowrates of stream 1 and 2, which were controlled by MKS mass flow controllers. The adsorbent bed was maintained at 1 bar by another MKS Baratron pressure controller. The effluent gas from the adsorbent bed was sampled by an Agilent 5975 mass spectrometer.

A constant, unperturbed feed was passed through the bed until the system reached steady state at the desired gas-phase concentration. Then, the flowrates of the two He streams were set to undergo sinusoidal perturbations 180 degrees out of phase. In order to maintain linearity of the system, the amplitude of the flowrate perturbations for both streams was small, about 10% of the flowrate of the saturated adsorbate stream. The resulting feed stream to the adsorbent bed had constant total flowrate with a sinusoidal adsorbate concentration swing around the steady state concentration. The sinusoidal perturbations were performed over a frequency range of 0.0001 to 0.01 Hz. The amplitude of the concentration swing into the bed was known by mass balance and was compared to the amplitude leaving the bed calculated from the concentration measured by the mass spectrometer. A plot of the amplitude ratio (AR), i.e., the exiting amplitude of the gas-

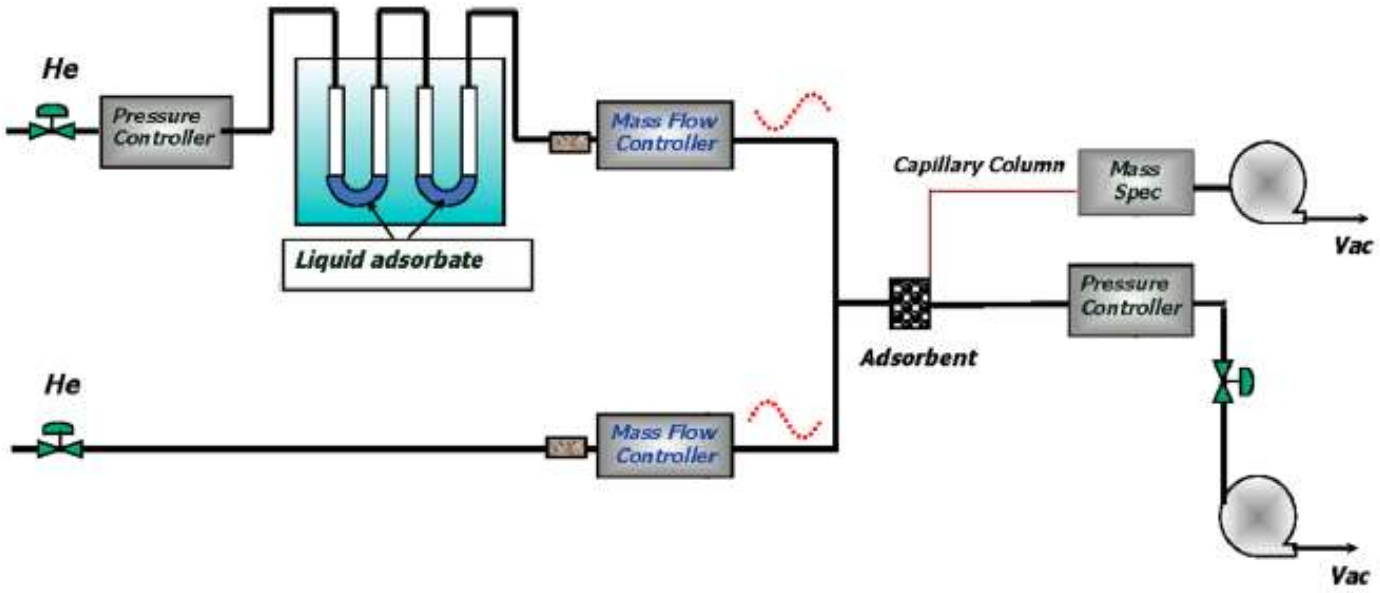

Figure 2.1: CSFR apparatus adapted from Wang et al.[8]

phase concentration oscillations over the entering amplitude, versus the frequency of oscillation was used to determine rate limiting mechanisms and diffusion rate parameters through comparison to a mathematical model.

Detailed mathematical models for a CSFR apparatus have been described elsewhere;[10] however, a brief description is provided here. For a linearized system with a sinusoidal input variable, the response variable will also be sinusoidal and the amplitude ratio is given by the modulus of the complex transfer function.[11] Transfer functions for the CSFR apparatus have been derived by Laplace transform of mass balances around the mixing and adsorbent bed regions.

The transfer function for the mixing and adsorbent bed regions is given by[10]

$$G_T = \frac{\bar{c}_{out}}{\bar{c}_{in}} = \frac{\alpha_m \alpha_b}{(s+\alpha_m)\left[s\left(1+\frac{m}{V_b c_0} G_n\right)+\alpha_b \right]} \tag{2.1}$$

where α is the ratio of flowrate to region volume (m for mixing region, b for adsorbent bed), m is the adsorbent mass, V_b is the bed volume, c_0 is the steady state gas-phase concentration, and G_n is the adsorbed phase transfer function. The adsorbed phase transfer function relates how the gas-phase adsorbate adsorbs and diffuses through the adsorbent particles.

Through G_n, different diffusive rate models such as micropore diffusion and barrier resistance (LDF) have been derived and can be plugged into Eq. 2.1 to give a total system transfer function. The BPL activated carbon particles are roughly spherical, for which the micropore diffusion model is given by

$$\frac{\partial n}{\partial t} = \frac{1}{r^2}\frac{\partial}{\partial r}\left(D_s r^2 \frac{\partial n}{\partial r} \right) \tag{2.2}$$

$$n = n^* \; at \;\; r = R \tag{2.3}$$

$$\frac{\partial n}{\partial r} = 0 \;\; at \;\; r = 0 \tag{2.4}$$

where n is the adsorbed phase concentration, n^* is the equilibrium adsorbed concentration which is known from equilibrium isotherms, r is the radial coordinate, R is the radius of the microporous domain, D_s is the surface diffusivity, and t is time. The LDF model is given by

$$\frac{\partial n}{\partial t} = k(n^* - n) \tag{2.5}$$

where k is the linear driving force mass transfer coefficient. Solving equations 2.2 and 2.5 by Laplace transform gives the adsorbed transfer function[10]

$$G_n = \frac{\overline{n}}{\overline{P}} = 3K\frac{D_s}{R^2}\frac{1}{s}\left[\sqrt{\frac{R^2}{D_s}}\sqrt{s}\coth\left(\sqrt{\frac{R^2}{D_s}}\sqrt{s}\right) - 1\right] \tag{2.6}$$

for micropore diffusion and

$$G_n = \frac{\overline{n}}{\overline{P}} = \frac{Kk}{s+k} \tag{2.7}$$

for the LDF model where K is the local isotherm slope. Plots of amplitude ratio versus frequency can be fitted using the total transfer function to determine the controlling mechanism and rate parameters.

2.2.3 *Isotherm measurements*

The isotherms measured at ECBC used a gravimetric adsorption method that used a known vapor concentration at a constant total flow of 1 slpm using air as the diluent to an adsorbent sample suspended from a microbalance. A schematic of the apparatus is presented in Figure 2.2. The gas-phase concentration was established by mixing a fraction of the air in a vapor-liquid contactor to achieve saturation. Details of this gas-liquid contactor operation are described elsewhere.[12] The adsorbent sample was placed in a fine mesh, wire basket which hung from one arm of a Cahn D200 microbalance. A counterweight was hung from the other arm. A

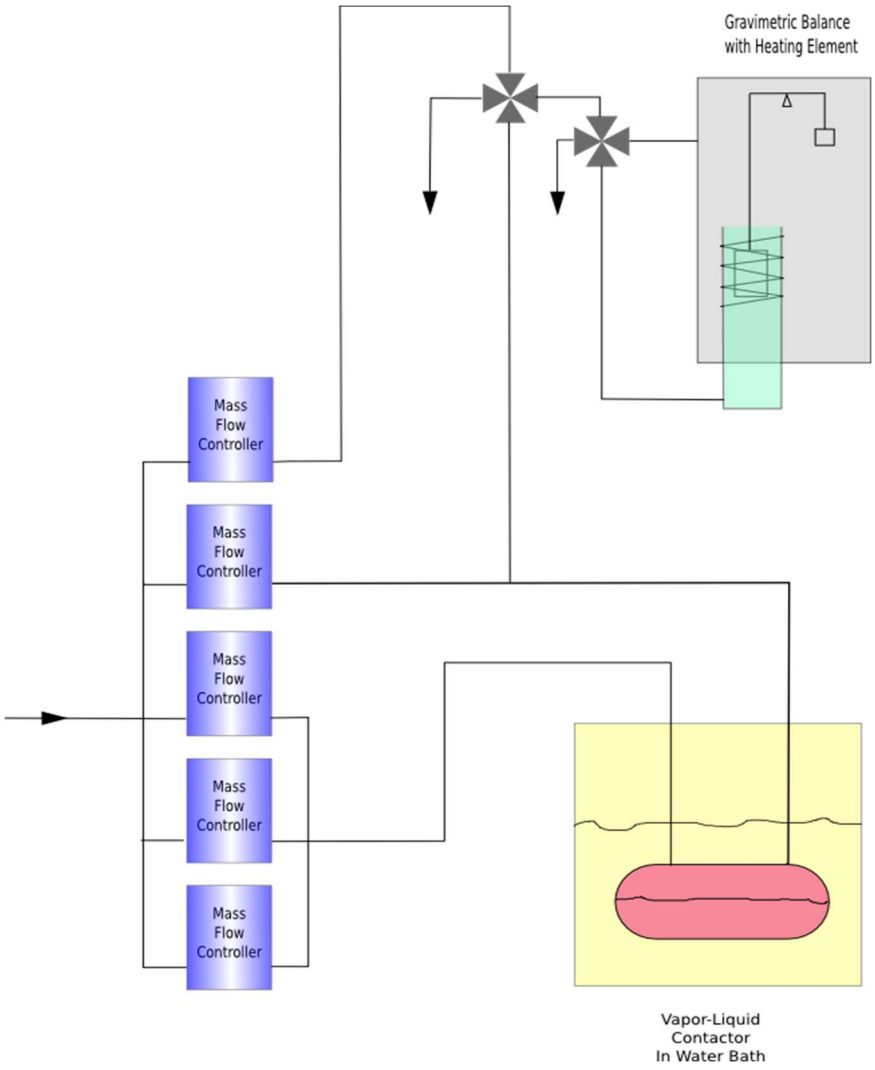

Figure 2.2: Gravimetric adsorption equilibrium apparatus.

novel glass arm was attached to the head of the microbalance. The vapor flow entered the top port of this glass housing. The gravimetric basket could be removed by lifting it off the suspension wire from the open bottom end of the housing. A bottom attachment of the glass housing was installed once the basket was placed on the hangdown wire. This lower glass assembly contained a NiChrome wire heating element that surrounded the suspended basket and did not interfere with the movement of the basket. It also contained an exit port and an interface for the heater leads and a thermocouple. The tip of the thermocouple was positioned within millimeters of the bottom of the basket. One 4-port switching valve was used to select whether the challenge was either clean purge or chemical containing air. Another 4-port valve selected whether the flow was directed to the bed or bypassed it.

A computer program was used to establish flow controller settings, the switching valve positions and the gravimetric balance output. The program also was used to conduct timed sequences and test equilibration criteria. Typically, the system was operated by loading the adsorbent with a high concentration, near saturation, until the adsorbent was equilibrated. The temperature of the sample was then raised to drive off some of the adsorbed vapor, and then the sample was allowed to cool as a lower concentration was then passed to the sample. The concept was that it takes a long time to deliver enough mass to load the sample at low concentrations, therefore, by approaching equilibrium from a partially loaded sample the equilibration time can be reduced. Care was taken to identify conditions such that the equilibrium point was approached from the adsorption side. The heating element can also be used to perform the equilibration routine at elevated temperatures.

The Dubinin-Astakhov (DA) micropore filling model was used to fit the adsorption isotherms and is given by[13]

$$C_{\mu} = \frac{W_0}{V_m} \exp\left[-\left(\frac{RT}{E} \ln\left(\frac{P_s}{P} \right)^n \right) \right] \tag{2.8}$$

where W_0 is the micropore volume of the adsorbent, V_m is the adsorbate molar volume, E is the characteristic adsorption energy, and n is a heterogeneity factor. W_0, E, and n were regressed for each isotherm individually.

Using the regressed diffusion coefficients from the CSFR experiments and the adsorption isotherms, a Darken analysis was used to predict a corrected diffusivity in the Henry's law regime for each adsorbate. The Darken model is derived by writing micropore flux in terms of a chemical potential gradient with the end result given by

$$D_s = D_0 \Gamma = D_0 \frac{d \ln P}{d \ln n} \tag{2.9}$$

where D_0 is the corrected diffusivity and the thermodynamic correction factor Γ is given by the chord over the slope of the adsorption isotherm at a specified concentration.

2.2.4 *QSAR modeling*

To search for correlations between the measured diffusivities and the molecular structure and properties of the compounds, DFT calculations were performed at ECBC using Gaussian (G09, revision C.01) with the B3LYP functional and the 6-31g(d,p) basis set.[14] To avoid the computational expense and complexity of directly simulating the adsorbate molecules on and around various surfaces within the adsorbent pores, simple gas-phase geometry optimized structures of the adsorbates were used to approximate bulk molecular structure while searching for possible structure-activity relationships. For rigid molecules with few torsional degrees of freedom (e.g., α-pinene), the simple gas-phase structures should approximately mimic the relevant adsorbed structures in terms of correlated behavior; for flexible molecules with many torsional degrees of freedom (e.g., decane), the adsorbed structures may differ significantly from the gas-

phase structures. Simple molecular properties (descriptors or correlation variables) were calculated using these optimized gas-phase structures and then correlated to the measured diffusivities. The following correlation variables were calculated: radius of gyration, dipole moment (using partial charges obtained from the Mulliken population analysis),[15] molecular volume, solvent-accessible surface area (using a probe radius of 1.5 Angstroms characteristic of N_2),[16] aspect ratio (widest dimension divided by 2nd widest dimension), and an approximate steric metric referred to as the minimum pore slot area (2nd x 3rd) widest dimensions), which represents the smallest rectangular pore (slot) that the molecule can readily fit through. Visual Molecular Dynamics (VMD) and Gaussian were used for these calculations, and VMD was used for rendering all images of the optimized structures.[17] Additional correlation variables were used, such as the molecular weight, molecular topology (e.g., # of double bonds, # of rings, # of flexible torsions, etc.), and experimental properties reported in the literature (e.g., boiling point, density, vapor pressure, etc.).

2.3 Results and Discussion

The molecules studied in this paper are n-decane, α-pinene, decalin, limonene, and perfluorodecalin. These molecules have ten carbon atoms arranged in different configurations to vary the degree of branching and ring structures. Figure 2.3 shows the three-dimensional molecular structure for α-pinene, cis- and trans-decalin, and limonene. Both limonene and α-pinene have a single six-membered ring with a double bond inside the ring. Limonene has more branching with an isopropenyl group where as α-pinene has multiple methyl groups. While neither ring is planar, α-pinene has a bridging carbon which gives it a more three-dimensional shape. Decalin has two six-membered rings fused along one carbon-carbon bond. Both rings are

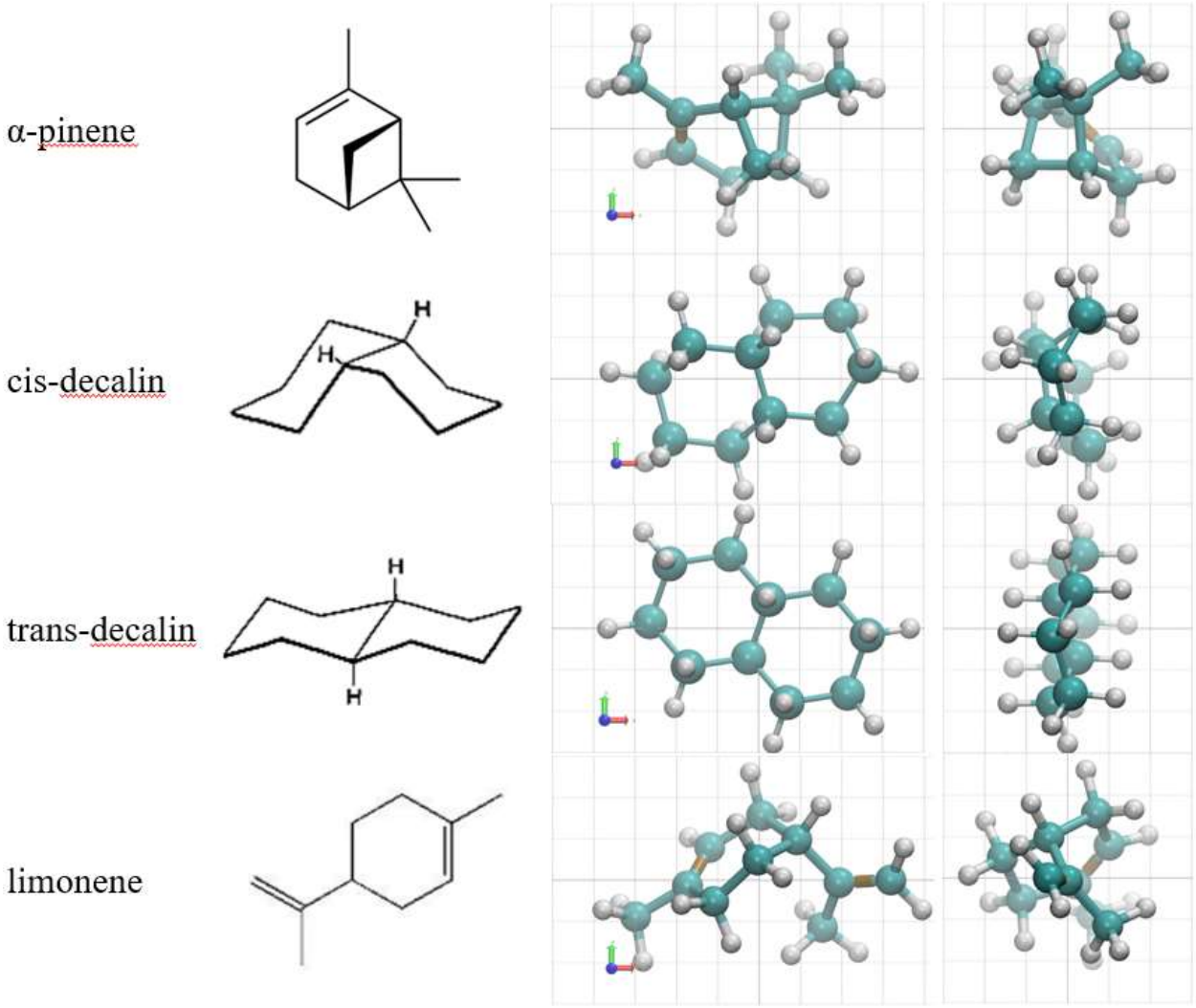

Figure 2.3: Atomic structure of α-pinene, cis- and trans-decalin, and limonene. VMD images are viewed along the shortest dimension to help visualize aspect ratio and then rotated 90° to be viewed along the longest dimension to help visualize the minimum pore slot area.

saturated and exist in cis- and trans- geometric isomers along the fused bond. Molecular descriptors for the stereoisomers are similar and the sample used was a mix of the two. Perfluorodecalin is similar to decalin with all hydrogen molecules replaced by fluorine.

By using different adsorbed-phase transfer functions in the mathematical model, the CSFR technique can easily distinguish the limiting diffusive mechanism. Figure 2.4 shows a typical experimental CSFR curve of amplitude ratio versus frequency for a gas phase concentration of 1000 ppm of α-pinene on BPL activated carbon. In addition to the data points, two curves are shown, one using the micropore diffusion model and the other using the linear driving force model. The micropore diffusion model, based on Fickian diffusion, describes the surface diffusion of molecules once they adsorb inside micropores; whereas, the LDF model has been associated with surface barriers where resistance is due to an inability of the molecule to enter the pore space. In this system, the micropore diffusion model accurately fits the experimental data while the LDF model clearly does not recover the shape of the curve, thus establishing micropore diffusion as the rate limiting mechanism. This result is in agreement with previous CSFR results for hydrocarbon adsorbates on BPL activated carbon.[8]

Isothermal models were used for both the micropore diffusion and linear driving force. It has been shown that unlike the traditional volume-swing frequency response, flow through techniques like pressure-swing and concentration-swing can help mitigate heat of adsorption effects.[18,19] It should be noted that in a linearized system, macropore diffusion has the same functional form as micropore diffusion in the mathematical model and would fit the data equally well. However, based on the predominantly microporous pore size distribution of BPL activated carbon as well as previous CSFR findings for linear alkanes that showed that the regressed macropore diffusion coefficients were not consistent with binary gas-phase diffusion coefficients,

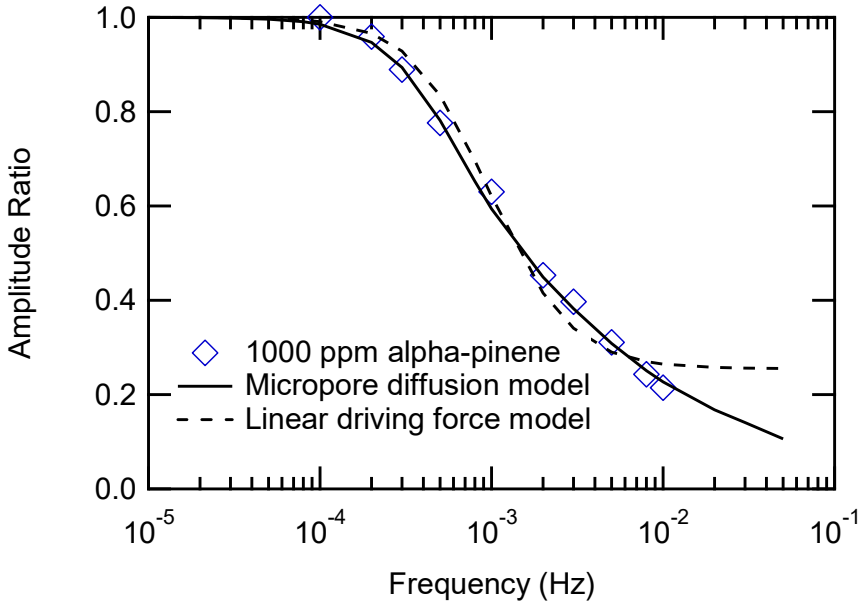

Figure 2.4: Comparison of the micropore diffusion and linear driving force models for fitting experimental data for 1000 ppm α-pinene on BPL activated carbon.

the diffusion of low volatility hydrocarbons on BPL activated carbon is found to be micropore diffusion controlled.[8]

Due to the small cyclic perturbations, the CSFR technique is highly accurate and repeatable. The amplitude ratio measurements are based on a cycling frequency and not dependent on an initial start time, thereby eliminating any source of human error in the experiment. Figure 2.5 shows an error analysis for the same 1000 ppm α-pinene data as in Figure 2.4. Error bars for each data point represent a 95% confidence interval calculated from a minimum of 4 replicate cycles at each frequency. The error bars for each data point are less than 5% relative error. In general, the slower frequency data points have larger error bars since the slower frequency data takes much longer to collect and therefore averages fewer replicates. Another possible source of error is temperature fluctuations in the room that are on the same time scale as the longer oscillations. Three fits were used to describe the data; one is a fit using the average values of the amplitude ratio while the other two curves are fit through the upper and lower 95% confidence limits. The regressed local isotherm slope values were 90, 105, and 115 mol/(kg·bar) and the surface diffusion parameters, D_s/R^2, were 1.5×10^{-4}, 1.2×10^{-4} and 9×10^{-5} s^{-1} for the fits through the upper confidence limit, average values, and lower confidence limit respectively. These results were typical for the CSFR experiments and show an approximate 20% error in the measured values. For the rest of the paper, only the average amplitude ratio data points and parameters from the fit through the averages will be given.

Figure 2.6 shows CSFR curves measured for α-pinene, decalin, perfluorodecalin, and limonene. Experiments were performed at multiple gas-phase concentrations for each adsorbate in the range of 100 ppm to 1000 ppm. Each experiment was performed with a flow rate of 20 sccm and a sample mass of ~25 mg. All fits are based on the isothermal micropore diffusion

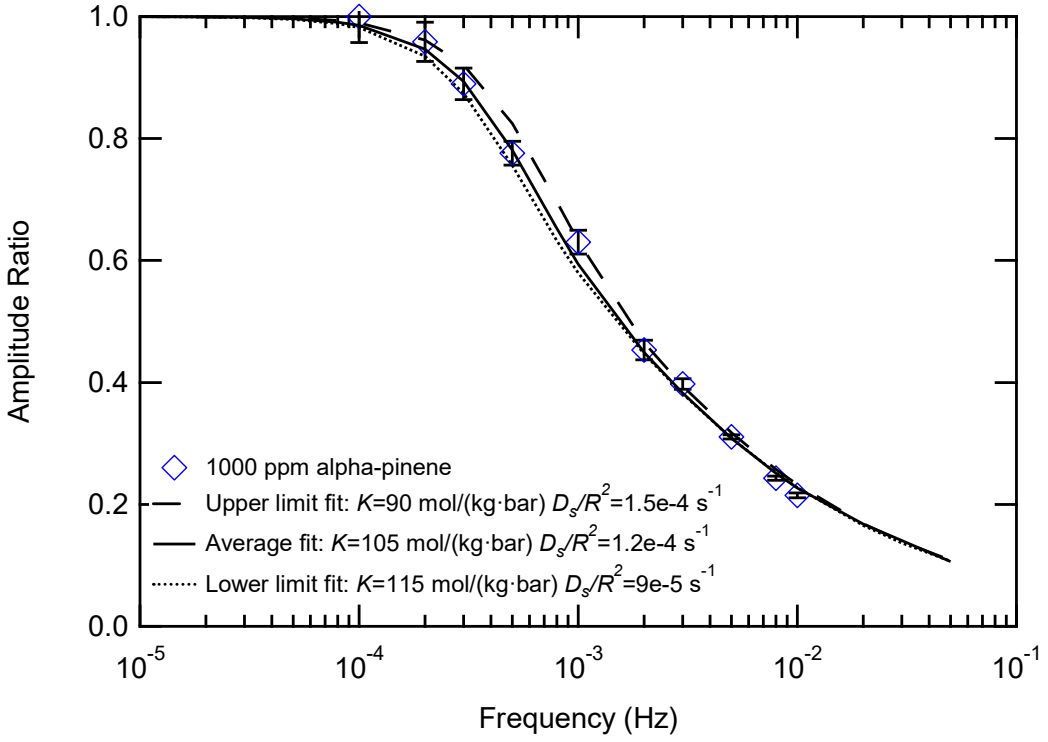

Figure 2.5: Example of error analysis for CSFR curves using the 1000 ppm α-pinene data.

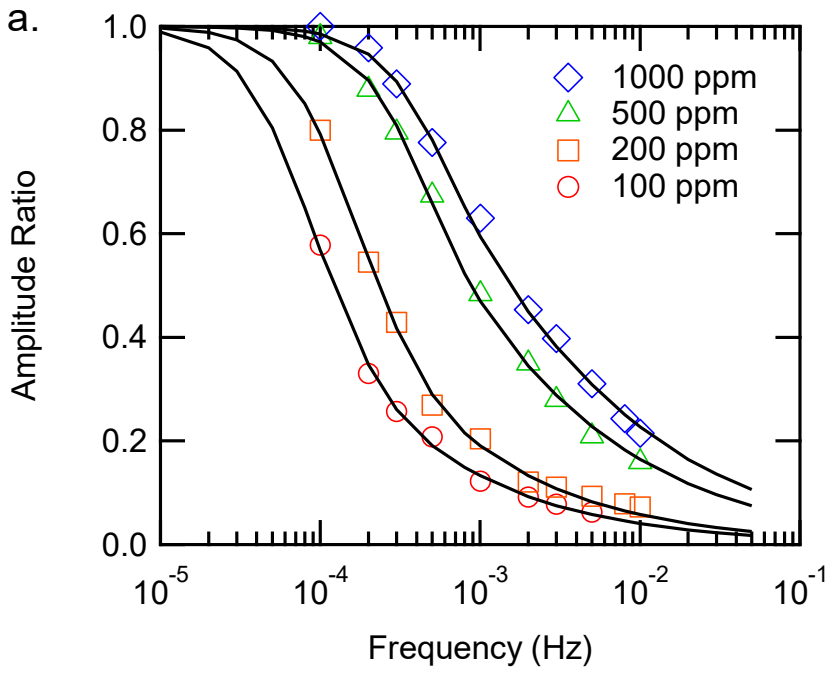

Figure 2.6: CSFR data for (a) α-pinene, (b) decalin, (c) limonene, and (d) perfluorodecalin.

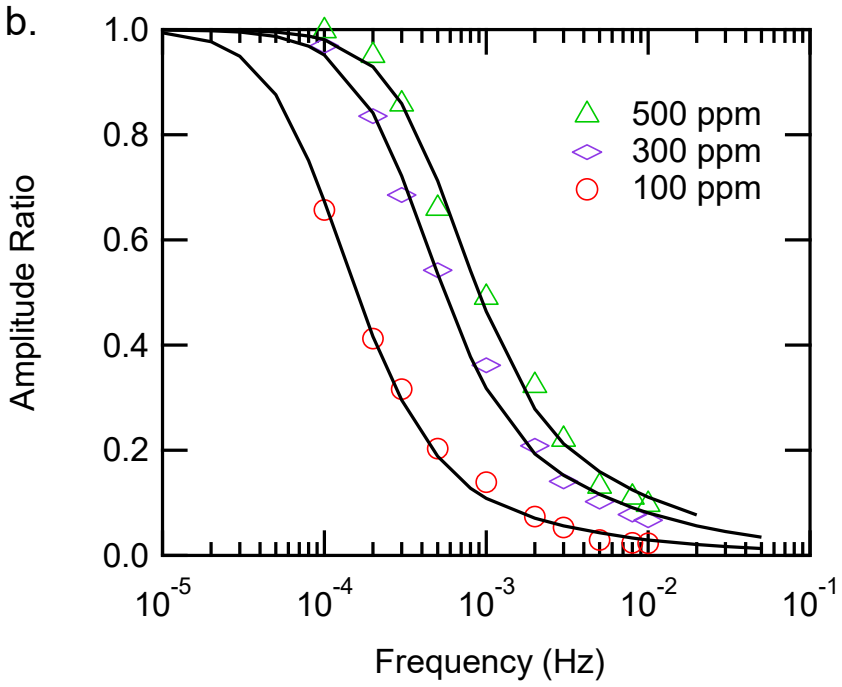
b.
1.0
0.8
0.6
0.4
0.2
0.0
Amplitude Ratio
500 ppm
300 ppm
100 ppm
10-5
10-4
10-3
10-2
10-1
Frequency (Hz)

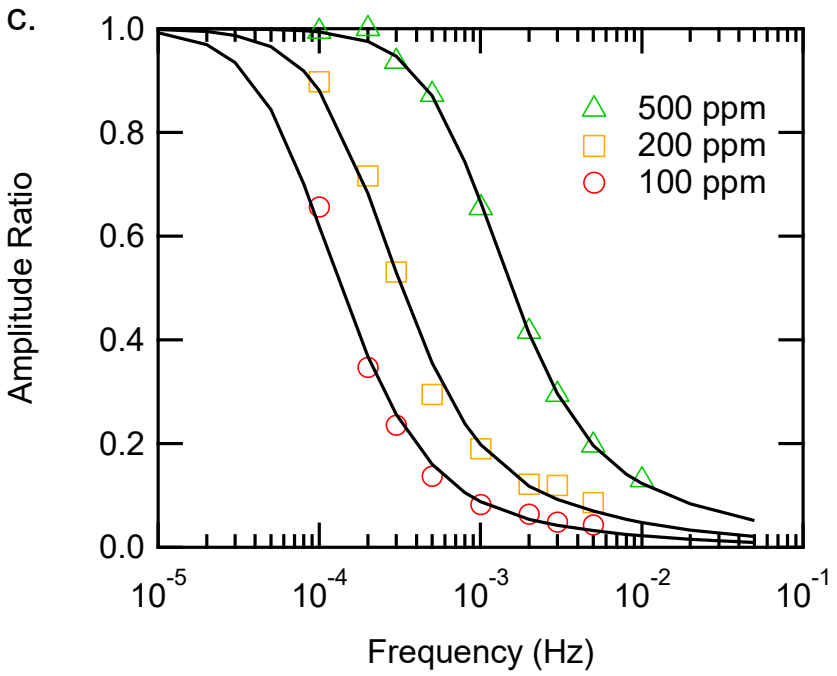
c.
1.0
0.8
0.6
0.4
0.2
0.0
Amplitude Ratio
500 ppm
200 ppm
100 ppm
10-5
10-4
10-3
10-2
10-1
Frequency (Hz)

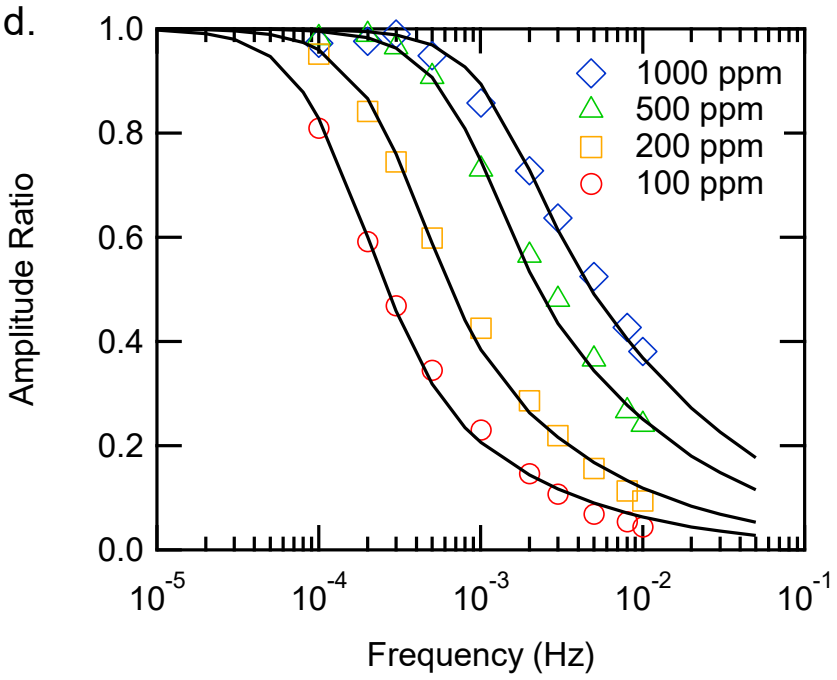
d.
Amplitude Ratio
1.0
0.8
0.6
0.4
0.2
0.0
1000 ppm
500 ppm
200 ppm
100 ppm
10-5
10-4
10-3
10-2
10-1
Frequency (Hz)

Table 2.1: Measured diffusion coefficients, isotherm slopes, and Darken thermodynamic correction factors for α-pinene, decalin, perfluorodecalin, and limonene.

	α-Pinene				*Decalin*				*Perfluorodecalin*				*Limonene*			
Conc	D_s/R^2	Γ	K CSFR	K Isotherm	D_s/R^2	Γ	K CSFR	K Isotherm	D_s/R^2	Γ	K CSFR	K Isotherm	D_s/R^2	Γ	K CSFR	K Isotherm
(ppm)	(1/s)		(mol/kg·bar)		(1/s)		(mol/kg·bar)		(1/s)		(mol/kg·bar)		(1/s)		(mol/kg·bar)	
100	0.00004	20	1129	1461	0.00013	31	894	956	0.00008	17	514	967	0.00018	25	1050	1268
200	0.00007	25	586	599					0.00013	18	208	475	0.00022	26	431	612
300					0.00022	42	249	242								
500	0.00010	37	164	167	0.00031	52	152	119	0.00028	19	62	182	0.00084	29	189	226
1000	0.00012	55	105	56					0.00041	21	32	85				

model and accurately describe the data for each adsorbate at each gas-phase concentration. Table 2.1 summarizes the two fitted parameters, K and D_s/R^2, for each CSFR curve from Figure 2.6.

There are two trends in the data that are consistent for each of the adsorbates. Since hydrocarbons on activated carbon give favorable isotherms, the isotherm slopes will decrease as the gas-phase concentration increases. The regressed isotherm slopes from the CSFR experiments all show this expected relationship. The second trend for each of the adsorbates is the increase in diffusion coefficient as concentration increases. The concentration dependence on surface diffusion is a known phenomenon.[20-24] In heterogeneous adsorbents, stronger adsorption sites will be occupied first and adsorbed molecules cannot diffuse easily. As surface concentration increases, lower energy adsorption sites are occupied and diffusion coefficients increase.

Figure 2.7 shows adsorption isotherms for n-decane, α-pinene, limonene, decalin, and perfluorodecalin on BPL activated carbon. Limonene, decalin, and α-pinene have the highest adsorption capacities, reaching over 3 mol/kg. The linear alkane decane has a higher molar volume resulting in a lower capacity. The fluorocarbon is a larger compound and has the lowest capacity of the tested adsorbates reaching a maximum loading of approximately 1.9 mol/kg.

The isotherm fits in Figure 2.7 are based on the Dubinin-Astakhov model, and the regressed fitting parameters are given in Table 2.2. The micropore volume of BPL activated carbon measured by nitrogen physisorption is 500-550 cm^3/kg which is consistent with the regressed W_0 for each adsorbate. For adsorbents with very narrow pore size distributions, the heterogeneity factor n is equal to or greater than 3, and systems where n is below 3 are deemed heterogeneous.[13] Each regressed n is less than 3, which is consistent with the heterogeneous nature of activated carbon. It should be noted that the Dubinin-Astakhov model does not have the correct behavior in the Henry's Law regime. However, despite the low gas-phase concentration, the adsorption affinity

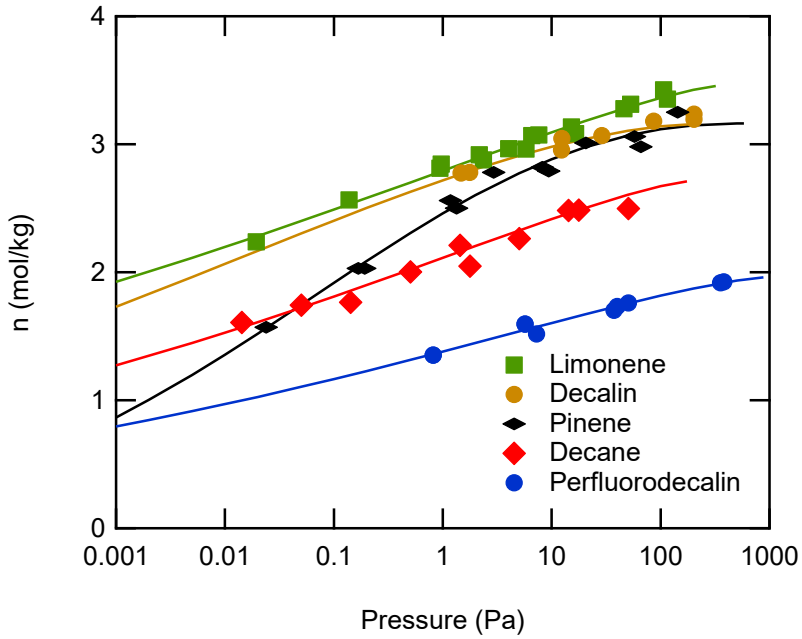

Figure 2.7: Adsorption isotherm data for limonene, decalin, α-pinene, decane, and perfluorodecalin on BPL activated carbon.

Table 2.2: Dubinin-Astakhov parameters for adsorption isotherms of limonene, decalin, α-pinene, decane, and perfluorodecalin.

Adsorbate	*Wo* (cm^3/kg)	*E* (*kJ/mol*)	*n*	P_s (25 °C) (*Pa*)	V_m (cm^3/mol)
limonene	560	47	1.29	320	162
decalin	487	41	1.67	205	154
α-pinene	502	29	2.23	582	159
decane	531	37	1.31	196	196
perfluorodecalin	472	36	1.34	879	241

for the C_{10} adsorbates is so high that the isotherm measurements as well as the frequency response experiments are well outside the Henry's Law limit. A Toth isotherm model was also considered and produced similar fits through the data range of the adsorption isotherms.

To validate the CSFR results, the regressed isotherm slopes from the CSFR experiments can be compared to the slopes of measured adsorption isotherms. These values are shown side by side in Table 2.1. For the hydrocarbon adsorbates, these two values are similar across the measured concentration range. For perfluorodecalin, the isotherm slope values measured by CSFR are lower than slopes calculated from adsorption equilibria. This result may indicate some effects of size exclusion in smaller micropores.

Figure 2.8 shows a plot of the regressed micropore diffusion coefficients as a function of concentration. As expected, the diffusion coefficients for each adsorbate increase as the concentration increases; however, there are significant differences in the concentration dependence of diffusion constants between the different adsorbates. It should be noted that a linear relation between diffusivity and concentration is not expected and the fitted lines are simply a guide through the data. The decane and limonene diffusion data show the largest concentration dependence. Decalin and perfluorodecalin have a lower concentration dependence and are similar to each other. Of the measured adsorbates, α-pinene shows the least diffusion dependence on concentration.

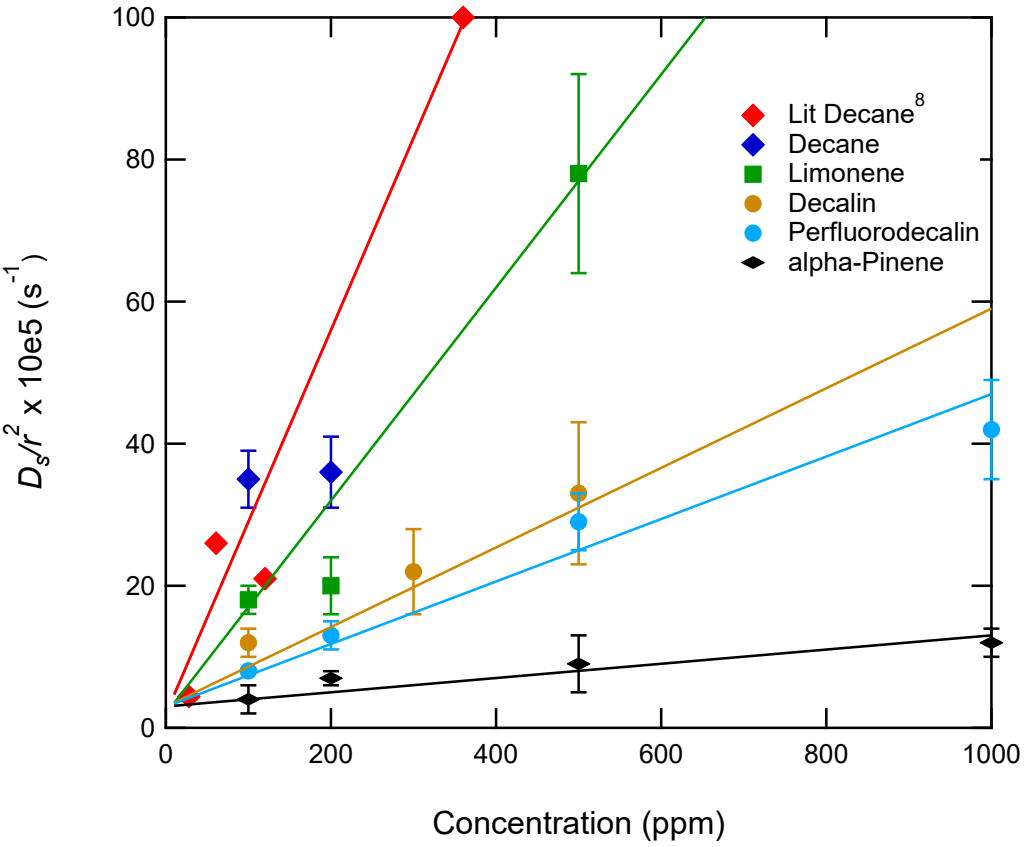

Figure 2.8: Surface diffusion data as a function of gas phase concentration for decane, limonene, decalin, perfluorodecalin, and α-pinene.

A Darken analysis was used to attempt to describe the concentration dependence of the diffusion coefficients. The Darken relation, given by eq. 2.9, describes diffusion coefficients measured at a given concentration by a corrected diffusivity in the Henry's law regime and a thermodynamic correction factor that can easily be calculated from adsorption equilibrium data. Table 2.1 lists the Darken thermodynamic correction factor for each adsorbate at each gas-phase concentration. Dividing the measured diffusion coefficient by the correction factor yields an approximation for the lower limit of diffusion in the Henry's law regime, which is of interest for filter performance at low concentrations. Ideally, the increase in the diffusion coefficient as a function of concentration should be mirrored by a similar trend in the thermodynamic correction factor. For C_{10} adsorbates on BPL activated carbon, the Darken model does not necessarily describe the data well. Pinene shows the lowest concentration dependence with only a two-fold increase in the measured diffusion coefficient from a gas-phase concentration of 100 to 1000 ppm, which is close to the increase in the Darken factors predicted from the adsorption isotherm. However, for limonene the diffusion coefficient increases by a factor of 5 while the Darken factor only increases by about 20%. This result is similar for decalin and perfluorodecalin and shows that in general that hydrocarbon diffusion on activated carbon has a much larger concentration dependence than that predicted by the Darken model. This trend has also been observed for the diffusion of ethane, propane, n-butane, n-hexane, benzene and ethanol on activated carbon.[5,9] The average corrected diffusivity (D_0/R^2) were calculated as 1.74×10^{-5}, 1.48×10^{-5}, 1.15×10^{-5}, 5.13×10^{-6}, and 2.43×10^{-6} s^{-1} for decane, limonene, perfluorodecalin, decalin, and α-pinene, respectively. For BPL activated carbon, the micropore diffusion length scale is over the whole particle;[8] with particle sizes of approximately 2 mm, this results in diffusivities between 2×10^{-12} and 2×10^{-11} m^2/s.

The order of magnitude difference is significant, and it is important to understand why certain compounds diffuse more slowly.

Assuming a micropore filling model in which the condensed adsorbed phase is liquid like, the measured diffusion coefficients can be compared to predicted self-diffusion coefficients. Table 2.3 gives some properties of each molecule and values of liquid phase self-diffusion coefficients predicted by the Wilke-Change, Tyn-Calus, and Nakanishi methods.[25] Similar to the CSFR results, decane and limonene have the highest self-diffusion coefficients. However, the predicted self-diffusion coefficient for α-pinene is faster than decalin and perfluorodecalin, which is opposite of the measured values. This clearly indicates that the differences in the diffusion coefficients measured by CSFR are not simply due to intermolecular interactions between the adsorbate molecules and represent a more complex interaction involving the adsorbent.

Table 2.3: Liquid phase properties for each compound and predicted liquid phase self-diffusion coefficients.

Adsorbate	*MW (g/mol)*	*V_m (cm^3/mol)*	*η (cP)*	*Wilke-Chang (cm^2/s)*	*Tyn-Calus (m^2/s)*	*Nakanishi (m^2/s)*
limonene	136.2	162.0	0.9	1.3×10^{-09}	1.2×10^{-09}	1.4×10^{-09}
decane	142.3	196.0	0.9	1.2×10^{-09}	1.2×10^{-09}	1.3×10^{-09}
α-pinene	136.2	158.8	1.3	9.5×10^{-10}	8.8×10^{-10}	9.7×10^{-10}
decalin	138.3	154.3	2.5	5.0×10^{-10}	4.6×10^{-10}	5.1×10^{-10}
perfluorodecalin	462.0	241.0	5.1	3.5×10^{-10}	2.1×10^{-10}	2.3×10^{-10}

Comparing the molecular structures of the different adsorbates may provide more insight on why certain compounds diffuse more slowly. To aide in this, QSAR correlations were used to find certain molecular aspects that trend well with the corrected diffusivities. The different molecular descriptors that were considered were molecular weight, boiling point, density, molar volume, vapor pressure, radius of gyration, solvent accessible surface area, dipole moment, number of double bonds, number of rings, atoms shared between rings, flexible torsions, widest

dimension, 2nd widest dimension, 3rd widest dimension, aspect ratio, and minimum pore slot area, i.e. cross-sectional area. Figure 2.9 shows an example QSAR plot of the number of atoms shared between rings and Table 2.4 describes how highly correlated the molecular descriptors are using the R^2 value from a linear best fit.

The two descriptors most correlated to diffusivity are the number of rings in a molecule and the number of atoms shared between rings with R^2 values of 0.70 and 0.85 respectively. Both of these descriptors are negatively correlated such that an increase in these values causes a decrease in diffusivity. Intuitively this makes sense as ringed structures are bulky and could lead to steric hindrance effects. The next highly correlated descriptors are the widest dimension and radius of gyration. These descriptors, which are interrelated, show a positive correlation with diffusivity;

Table 2.4: QSAR correlations of corrected diffusivity for several molecular descriptors.

Molecular Descriptor	*R^2 correlation*
Number of atoms shared between rings	0.8451
Number of rings	0.7008
Widest dimension	0.662
Radius of gyration	0.5603
Number of flexible torsions	0.5095
Aspect ratio	0.4956
Solvent accessible surface area	0.4145
Second widest dimension	0.2387
Vapor pressure (25 °C)	0.1992
Molar volume	0.1883
Minimum pore slot area (cross-sectional area)	0.1302
Dipole moment	0.0929
Third widest dimension	0.0644
Molecular weight	0.0123
Boiling point	0.0111
Number of double bonds	0.0029
Density	2×10^{-5}

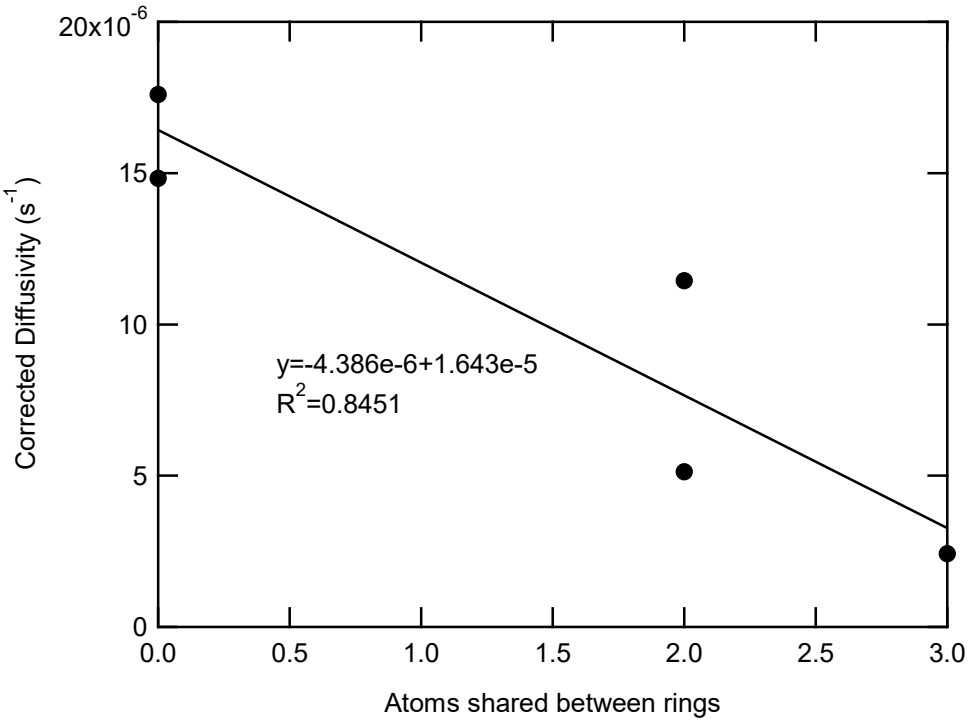

Figure 2.9: Example QSAR correlation for corrected diffusivity to the number of atoms shared between two rings in a molecule.

thus, longer, less compact molecules diffuse faster. These two sets of descriptors seem to be at odds in describing how molecular size impacts diffusivity. Liu et al.[26] found that uptake of substituted phenols in activated carbon fibers was dependent on a second widest dimension. However, QSAR's for the 2nd widest dimension and cross-sectional area show no correlation to the diffusivity data.

What these QSAR correlations reveal is that diffusion of the C_{10} molecules is likely not limited purely by size exclusion steric effects. Since the majority of BPL pore sizes are above 10 Å, which is larger than the dimensions of the adsorbates, any true size exclusion sieving effects are likely negligible. The two effects based on molecular shape are compactness and rigidity. The QSAR for radius of gyration indicates that the more compact molecules diffuse more slowly. This is possibly due to increased van der Waals interaction with the adsorbent surface for molecules where all of the carbons are more tightly packed; and are therefore more likely to have multiple interactions regardless of the orientation of the molecule as it approaches the surface.

The biggest impact on diffusion is molecular rigidity based on the QSAR correlations for ringed structures. Decane bonds are highly flexible which allows the molecule to contort and move more easily through pore spaces. The six-membered ring of limonene increases rigidity, while decalin and perfluorodecalin have two six membered rings further increasing rigidity. The structure of α-pinene introduces a bridged-ring structure which further decreases molecular flexibility. These trends in rings and molecular flexibility clearly have the highest correlation to diffusion of C_{10} molecules in BPL activated carbon. These insights are useful as rules for predicting diffusivity among isomers.

2.4 Conclusions

A concentration-swing frequency response apparatus was used to study diffusion rates of several C_{10} hydrocarbons in BPL activated carbon. Micropore diffusion was the rate limiting mass transfer mechanism for each adsorbate at various concentrations. Predicted local isotherm slopes from the CSFR experiments agreed well with those calculated from adsorption isotherms. The diffusion coefficients were found to be highly concentration dependent, and a Darken analysis was used to predict a lower limit for diffusivity in the Henry's law regime. The lower limit of diffusion for C_{10} hydrocarbons in BPL activated carbon is about 10^{-11} m^2/s, although values can be several orders of magnitude faster at higher concentrations. The order from fastest to slowest diffusion was n-decane > limonene > perfluorodecalin > decalin > α-pinene. QSAR correlations were performed to relate diffusivity to specific molecular aspects. Size exclusion based sieving effects were not observed as the wide pore size distribution of BPL activated carbon was larger than any molecular dimensions; however, the steric factors of molecular rigidity and compactness showed good correlation with diffusivity.

References

1. Denayer, J. F.; Souverijns, W.; Jacobs, P. A.; Martens, J. A.; Baron, G. V. High-Temperature Low-Pressure Adsorption of Branched C_5-C_8 Alkanes on Zeolite Beta, ZSM-5, ZSM-22, Zeolite Y, and Mordenite. *J. Phys. Chem. B* **1998**, 102, 4588-4597.
2. Huddersman, K.; Klimczyk, M. Separation of Hexane Isomers on Zeolites Mordenite and Beta. *J. Chem. Soc., Faraday Trans.* **1996**, 92, 143-147.
3. Jobic, H.; Karger, J.; Krause, C.; Brandani, S.; Gunadi, A.; Methivier, A.; Ehlers, G.; Farago, B.; Haeussler, W.; Ruthven, D. M.; Occelli, M. L. Diffusivities of n-Alkanes in 5A Zeolite Measured by Neutron Spin Echo, Pulsed-Field Gradient NMR, and Zero Length Column Techniques. *Adsorption* **2005**, 11, 403-407.
4. Laredo, G. C.; Meneses, E.; Castillo, J.; Marroquin, J. O.; Jimenez-Cruz, F. Adsorption Equilibrium and Kinetics of Branched Octane Isomers on a Polyvinylidene Chloride-Based Carbon Molecular Sieve. *Energy Fuels* **2008**, 22, 2641-2648.
5. Do, D. D. A model for surface diffusion of ethane and propane in activated carbon. *Chem. Eng. Sci.* **1996**, 51, 4145-4158.
6. Mangun, C. L.; Daley, M. A.; Braatz, R. D.; Economy, J. Effect of Pore Size on Adsorption of Hydrocarbons in Phenolic-Based Activated Carbon Fibers. *Carbon*. **1998**, 36, 123-129.
7. Jimenez-Cruz, F.; Hernandez, J. A.; Laredo, G. C.; Mares-Gallardo, M. T.; Garcia-Gutierrez, J. L. Adsorption of n-Heptane and 2-Methylheptane in the Gas Phase on Polyvinylidene Chloride-Based Microporous Activated Carbon. *Energy Fuels* **2007**, 21, 2929-2934.
8. Wang, Y.; Mahle, J. J.; Furtado, A. M. B.; Glover, T. G.; Buchanan, J. H.; Peterson, G. W.; LeVan, M. D. Mass Transfer and Adsorption Equilibrium for Low Volatility Alkanes in BPL Activated Carbon. *Langmuir* **2013**, 29, 2935-2945.

9. Do, H. D.; Do, D. D.; Prasetyo, I. On the surface diffusion of hydrocarbons in microporous activated carbon. *Chem. Eng. Sci.* **2001**, 56, 4351-4368.
10. Wang, Y.; LeVan, M. D. Nanopore Diffusion Rates for Adsorption Determined by Pressure-Swing and Concentration-Swing Frequency Response and Comparison with Darken's Equation. *Ind. Eng. Chem. Res.* **2008**, 47, 3121-3128.
11. Stephanopoulos, G. *Chemical Process Control: An Introduction of Theory and Practice*. Prentice-Hall, INC.: Englewood Cliffs, New Jersey, **1984**.
12. Butrow, A. B.; Buchanan, J. H.; Tevault, D. E. Vapor Pressure of Organophosphorus Nerve Agent Simulant Compounds. *J. Chem. Eng. Data* **2009**, 54, 1876-1883.
13. Do, D. D. *Adsorption Analysis: Equilibria and Kinetics*. Imperial College Press: London, **1998**.
14. A. D. Becke, "Density-functional thermochemistry. III. The role of exact exchange," J. Chem. Phys., 98 (1993) 5648-52.
15. Mulliken, R. S. (1955). "Electronic Population Analysis on LCAO-MO Molecular Wave Functions. I". The Journal of Chemical Physics 23 (10): 1833–1840.
16. A. Varshney, F. P. Brooks, W. V. Wright, Linearly Scalable Computation of Smooth Molecular Surfaces, IEEE Comp. Graphics and Applications, v. 14 (1994) pp. 19-25.
17. Humphrey, W., Dalke, A. and Schulten, K., "VMD - Visual Molecular Dynamics", J. Molec. Graphics, 1996, vol. 14, pp. 33-38.
18. Glover, T. G.; Wang, Y.; LeVan, M. D. Diffusion of Condensable Vapors in Single Adsorbent Particles Measured via Concentration-Swing Frequency Response. *Langmuir* **2008**, 24, 13406-13413.

19. Wang, Y.; LeVan, M. D. Master Curves for Mass Transfer in Bidisperse Adsorbents for Pressure-Swing and Volume-Swing Frequency Response Methods. *AIChE J.* **2011**, 57, 2054-2069.

20. Sudo, Y.; Misic, D. M.; Suzuki, M. Concentration dependence of effective surface diffusion coefficient in aqueous phase adsorption on activated carbon. *Chem. Eng. Sci.* **1978**, 33, 1287-1290.

21. Ehrlich, G.; Stolt, K. Surface Diffusion. *Ann. Rev. Phys.Chem.* **1980**, 31, 603-637.

22. Seidel, A.; Carl, P. S. The concentration dependence of surface diffusion for adsorption on energetically heterogeneous adsorbents. *Chem. Eng. Sci.* **1989**, 44, 189-194.

23. Chen, Y. D.; Yang, R. T. Concentration dependence of surface diffusion and zeolitic diffusion. *AIChE J.* **1991**, 37, 1579-1582.

24. Kapoor, A.; Yang, R. T. Contribution of concentration-dependent surface diffusion to rate of adsorption. *Chem. Eng. Sci.* **1991**, 46, 1995-2002.

25. Poling, B. E.; Prausnitz, J. M.; O'Connell, J. P. *The Properties of Gases and Liquids, 5th ed.* McGraw-Hill: New York, New York, **2001**.

26. Liu, Q.-S.; Zheng, T.; Wang, P.; Jiang, J.-P.; Li, N. Adsorption isotherm, kinetic and mechanism studies of some substituted phenols on activated carbon fibers. *Chem. Eng. J.* **2010**, 157, 348-356.

CHAPTER III

DIFFUSION OF CO_2 IN LARGE SINGLE CRYSTALS OF Cu-BTC

3.1 Introduction

Metal-organic frameworks (MOFs) contain metal clusters interconnected by organic linkers that form highly porous crystalline networks.[1] MOFs typically have high surface areas with some reported of over 6000 m^2/g.[2-6] In addition to high surface areas and porosities, MOFs exhibit a high degree of tunability of physical and chemical properties by varying the metal centers and organic linkers. The number of possible combinations are vast, and simulations have created a database of over 100,000 hypothetical MOFs.[7] As a result of these properties, extensive research has been done on MOFs for applications in separations,[8] gas storage,[9] catalysis,[10] and sensing.[11]

One area of particular interest is the capture of CO_2. Due to concerns over global climate change brought on by anthropogenic CO_2 emissions, MOFs have been studied as next-generation adsorbent materials for carbon capture and sequestration.[12] This includes research on CO_2/N_2 separation for post-combustion CO_2 removal from flue gas, CO_2/H_2 separation for pre-combustion capture, CO_2/CH_4 separation for natural gas upgrading, direct air capture, and storage. MOF related research in this area has been prolific, and several reviews have been published.[12-14]

Cu-BTC, also known as HKUST-1, has been a widely studied MOF for CO_2 adsorption. The structure consists of coordinatively unsaturated copper sites connected by benzene-1,3,5-tricarboxylate linkers, which creates the main 3D network of 9 Å pores.[15] It also contains side pockets only accessible through a 3.5 Å window.[16] At 1 bar, dry Cu-BTC has a CO_2 capacity of up to 5.6 mol/kg,[17] although it has been shown that different synthesis methods can significantly

impact CO_2 adsorption.[18] For storage purposes, CO_2 capacities have been reported up to 17 mol/kg at high pressure.[19] Cu-BTC changes color upon exposure to water, from dark blue to light blue, and coadsorption of small amounts of water have been found to increase CO_2 capacities due to additional quadrupolar interactions.[20] Selectivities for adsorption-based separations of CO_2 have been reported. CO_2/H_2 selectivities are well above 100 across a wide pressure range.[21] CO_2/N_2 selectivities are lower, ranging from 20 to 40,[20,22,23] and CO_2/CH_4 selectivities are below 10.[20,24,25]

Despite the amount of research on CO_2 adsorption in Cu-BTC, a major deficiency in the literature is the measurement of diffusion rates. This gap is not specific to Cu-BTC but is prevalent throughout the MOF literature where the bulk of kinetic-based separation studies is focused on MOF-based membranes.[26] Some CO_2 diffusion constants have been reported for a few MOFs: Salles et al.[27] measured diffusion rates ranging from 10^{-8} to 10^{-9} m^2/s over a range of loadings on MIL-47(V), Sabouni et al.[28] reported $7x10^{-12}$ m^2/s at 298 K for CPM-5, and Saha et al.[29] reported diffusion constants on the order of 10^{-9} m^2/s for MOF-177. For MOF-5, Saha et al.[29] found the diffusion coefficient to be around 10^{-9} m^2/s, while Zhao et al.[30] found the diffusion constants to be an order of magnitude faster, in the range of 10^{-8} m^2/s. Further complicating diffusion measurements is the presence of different diffusive mechanisms depending on adsorbent morphology. The impact of surface barriers on MOF thin films was explored by Heinke et al.[31] Fletcher et al.[32] found a linear driving force behavior for CO_2 in $Ni_2(4,4'\text{-bipy})_3(NO_3)_4$, but macropore diffusion was determined to be the controlling resistance for Co/DOBDC and Ni/DOBDC pellets by Hu et al.[33] using the zero-length column technique and for Cu-BTC pellets by Liu et al.[34] using concentration-swing frequency response (CSFR).

In this chapter, we report a new synthesis technique for large single crystals of Cu-BTC on the order of 1 mm in size. The crystals are characterized and their properties are compared to Cu-

BTC powders from traditional solvothermal synthesis. Diffusion of CO_2 is measured by the CSFR technique to determine rate controlling mechanisms and diffusion constants, and rate behavior is compared with that in an activated carbon. Due to the single crystal morphology of the Cu-BTC particles and the several order of magnitude increase in the diffusion length scale compared to powders, accurate diffusion constants for CO_2 in the micropores of Cu-BTC are obtained.

The work performed in this chapter was done in collaboration with researchers at North Carolina State University (NC State). The Cu-BTC single crystals were synthesized and characterized by Junjie Zhou, Billy Nunn, and Heather Barton in Professor Gregory N. Parson's laboratory. CO_2 isotherm and diffusion measurements were performed at Vanderbilt.

3.2 Experiments

3.2.1 Materials

Commercial adsorbents used in this study were Cu-BTC powder purchased from Sigma Aldrich and BPL activated carbon (lot no 4814-5) in 6x16 mesh form obtained from Calgon Carbon Corp. Research grade helium, pure CO_2, and 1% CO_2 in He were purchased from Air Liquide.

A low temperature solvothermal method was used to synthesize large Cu-BTC single crystals at NC State. Copper nitrate trihydrate ($Cu(NO_3)_2 \cdot 3H_2O$) was dissolved in deionized water. Benzene-1,3,5-tricarboxylic acid (H_3BTC) was dissolved in ethanol (slight heating was needed to fully dissolve this organic linker). The $Cu(NO_3)_2$ solution was first mixed with *N,N*-dimethylformamide (DMF) in a 20 mL scintillation vial. The H_3BTC solution and glacial acetic acid (modulator) were subsequently added to the mixed solution as well. The scintillation vial was then placed in a furnace where the reaction was allowed to proceed at 55 °C for 3 days. After the

solvothermal synthesis, the Cu-BTC crystals were removed by hand from the glass surface of the vial. All the crystals were soaked in ethanol for at least 3 days for solvent exchange.

3.2.2 Crystal Characterization

Cu-BTC single crystals were imaged at NC State using an Olympus BX60 optical microscope equipped with a ProgRes C5 camera. Optical microscopic images were captured and analyzed with ProgRes® CapturePro 2.8.8 software. SEM images of Cu-BTC crystal were taken at NC State with an FEI Phenom® bench-top SEM. Crystals were mounted on conductive carbon taps and sputter-coated with 5-10nm of Au-Pd before imaging. X-ray diffraction patterns of the Cu-BTC single crystals were collected using a PANalytical Empyrean X-ray diffractometer. BET surface area of Cu-BTC single crystals and powders was measured at NC State using a Quantachrome Autosorb-1C surface area and pore size analyzer. 10 mg of Cu-BTC was vacuum dried at room temperature for 12-18 h before the measurement of N_2 adsorption isotherm. BET surface area was calculated based on the isotherm within the P/P_o range of 0.02-0.10. Thermogravimetric analysis (TGA) was measured at NC State with a Discovery TGA from TA Instruments.

Pure CO_2 isotherms were measured at Vanderbilt using a Rubotherm gravimetric analyzer. A sample was degassed at 25 °C for approximately 12 hours using a turbo molecular pump until no weight change was detected. The sample was then dosed with CO_2 at a specified pressure and allowed to equilibrate until no more weight change was detected. After equilibration, the CO_2 pressure was increased to the next specified value. This process was repeated for the pressure range of the isotherm, from 0.5 to 800 mmHg. The CO_2 loading was calculated by the weight gain of the sample at each pressure step.

3.2.3 Diffusion Measurement

CO_2 diffusion was measured using the concentration-swing frequency response apparatus shown in Figure 2.1. Approximately 15-20 mg of adsorbent was regenerated for 8 hours under vacuum (at 25 °C for Cu-BTC cyrstals, at 250 °C for BPL activated carbon) for accurate weight measurement. The sample was loaded into a shallow bed and placed under vacuum at room temperature with a 1 sccm He flow for 16 hours. Then a CO_2 stream was mixed with the He stream upstream of the adsorbent bed. Both streams were controlled with MKS mass flow controllers, and the ratio of the two flow rates determined the gas-phase concentration. The pressure in the adsorbent bed was controlled at 1 bar by a MKS Baratron pressure controller, and effluent gas from the adsorbent bed was sampled by an Agilent 5975 mass spectrometer.

To run an experiment, the system was allowed to reach steady-state as determined by a constant signal from the mass spectrometer. Then the mass flow controllers were used to introduce sinusoidal perturbations to the flowrates of each stream but 180 degrees out of phase. This resulted in a feed stream to the adsorbent bed that has a constant flow rate with a sinusoidal concentration swing around the desired steady-state gas-phase concentration.

The perturbations were performed at different frequencies in the range of 0.001 to 0.1 Hz. The collected data are presented as plots of the amplitude ratio (AR) as a function of the perturbation frequency, where the AR is calculated from the amplitude of the gas exiting the adsorbent bed divided by the amplitude of the gas entering the adsorbent bed. The diffusion mechanism and rate parameters can be extracted by fitting the data to a mathematical model derived from transfer functions. Detailed mathematical models for a CSFR apparatus have been described elsewhere.[35,36]

3.3 Results and Discussion

3.3.1 Crystal Characterization

Figure 3.1 shows the optical micrographs and SEM images of the Cu-BTC single crystals. Truncated cube and truncated octahedron shapes were observed for this ***fcu***-type MOF crystal. The octagon (or square) facets represent the planes viewed down the <100> directions, while the hexagon-shape facets correspond to the planes along the <111> directions. The size of Cu-BTC crystals obtained from a 3-day synthesis ranges from 500 μm to 1.3 mm. These crystals were sorted by size for later CO_2 diffusion studies.

The quality of the Cu-BTC single crystals was characterized using XRD, BET, and TGA. Figure 3.2 shows the XRD patterns for the crystal planes parallel to (100) and (111) respectively. The peak positions match well with the corresponding peaks present in the simulated powder diffraction pattern and reported powder patterns in the literature.[37] The fact that only peaks associated with targeted parallel crystal planes appear in the diffraction patterns and that optical micrographs show negligible defects confirm the formation of high-quality single crystals.

BET surface area and pore volume for the Cu-BTC single crystals were measured and compared with the Cu-BTC fine powder prepared from 85 °C solvothermal synthesis. The surface area is 1980 and 1825 m^2/g for the single crystals and the fine powder respectively. Pore volumes are 0.85 and 0.79 cm^3/g for the large crystals and powder samples respectively. Both the surface area and pore volume compare well with values from the literature.[20]

TGA was used to evaluate the thermal stability of the Cu-BTC single crystals, Figure 3.3. Cu-BTC powder shows a steeper initial mass drop compared to the large crystals due to the shorter diffusion length in small particles for solvent evaporation. We also noticed that the mm-scale crystal exhibits a sharper mass decrease than the fine powder in the decomposition regime (300-

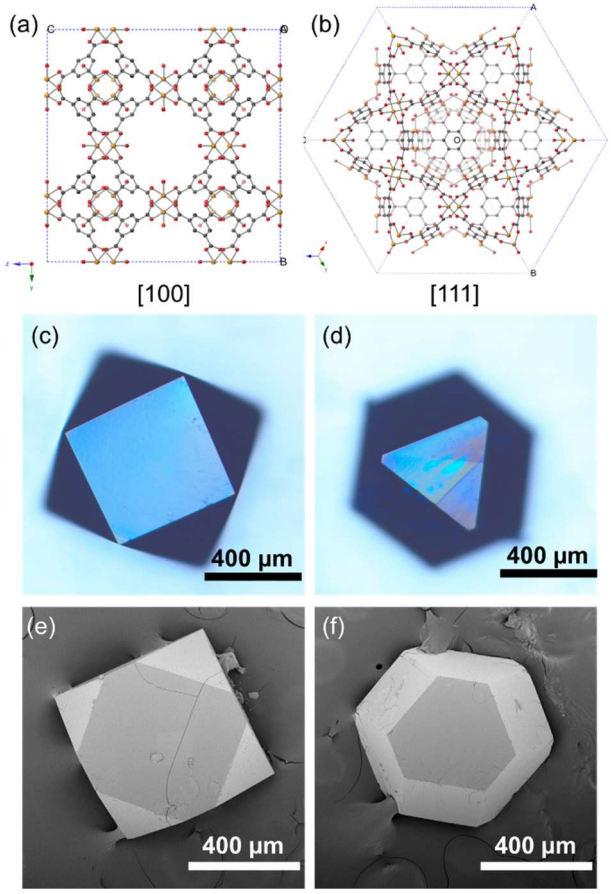

Figure 3.1 Molecular representation of the Cu-BTC MOF along the (a) [100] direction and (b) [111] direction. Color code: Cu (yellow); O (red); C (black); H (not shown). Optical microscopic (c,d) and SEM images (e,f) of Cu-BTC single crystals taken at NC State.

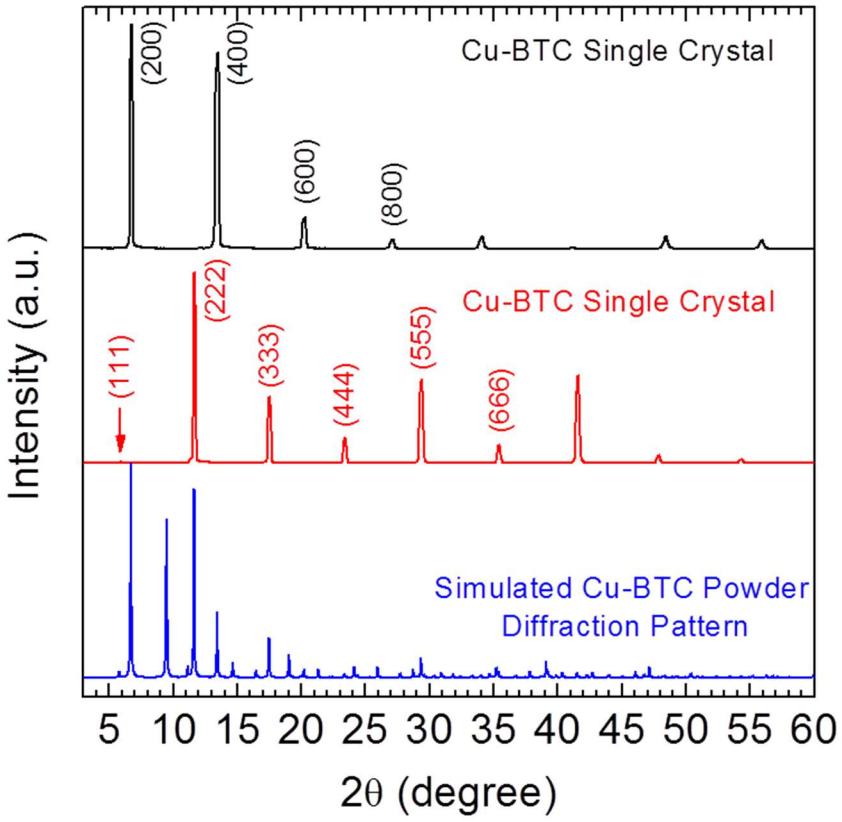

Figure 3.2 XRD patterns measured at NC State of a Cu-BTC single crystal for the planes parallel to (100) (black) and the planes parallel to (111) (red), and simulated powder diffraction pattern for Cu-BTC.

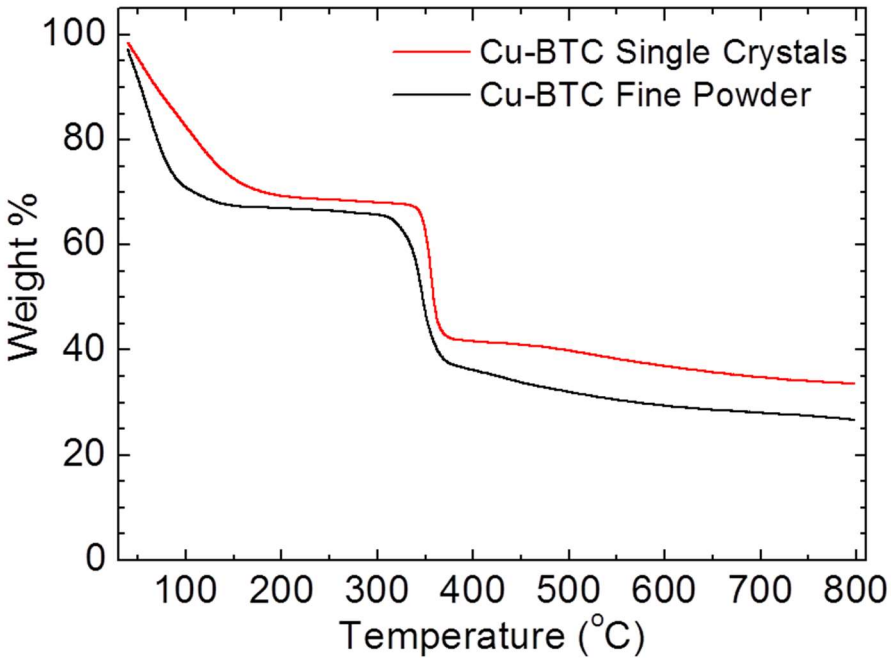

Figure 3.3 Thermogravimetric analysis for Cu-BTC single crystals (red) and fine powder (black) measured at NC State.

385 °C), possibly because of slower heat transfer and less impurities in the large crystals. Our measured decomposition temperature regime also agrees well with reported values,[18,25] indicating the good quality of these MOF crystals.

3.3.2 Crystal Growth Mechanism

The crystal size was measured after specific growth times (1-5 d), and Figure 3.4 shows that the size of the largest crystal increases as a function of synthesis time. At the beginning of the synthesis, no crystals form during the nucleation period while secondary building units (SBUs) of Cu-BTC MOF start to form in the solution. As the reaction proceeds and the SBU concentration reaches supersaturation (after ~1 d), heterogeneous nucleation occurs on the wall of the scintillation vial as it is more thermodynamically favorable and the crystal size quickly ramps up to ~1.3 mm at 3 days. The crystal growth rate depends on the SBU concentration and stops once the concentration drops below the supersaturation point after ~4 days, indicating the termination of crystal growth.

While previous work reported the use of nitric acid to inhibit the deprotonation of H_3BTC linker and thus slow down the crystal growth rate in order to achieve large single crystals,[38] our method is more effective and reproducible by using a supersaturated concentration of MOF reactants and an acetic acid modulator. The formation of an acetate complex competes with the generation of SBU in the solution, allowing the slow and steady growth of our single crystals. By avoiding high acidity of the precursor solution, we also obtained high crystal quality as shown above.

3.3.3 Diffusion Measurements

To ensure that CO_2 adsorption in the single crystals is similar to powder samples, a CO_2 isotherm was measured and compared with literature values. Figure 3.5 shows a CO_2 isotherm for

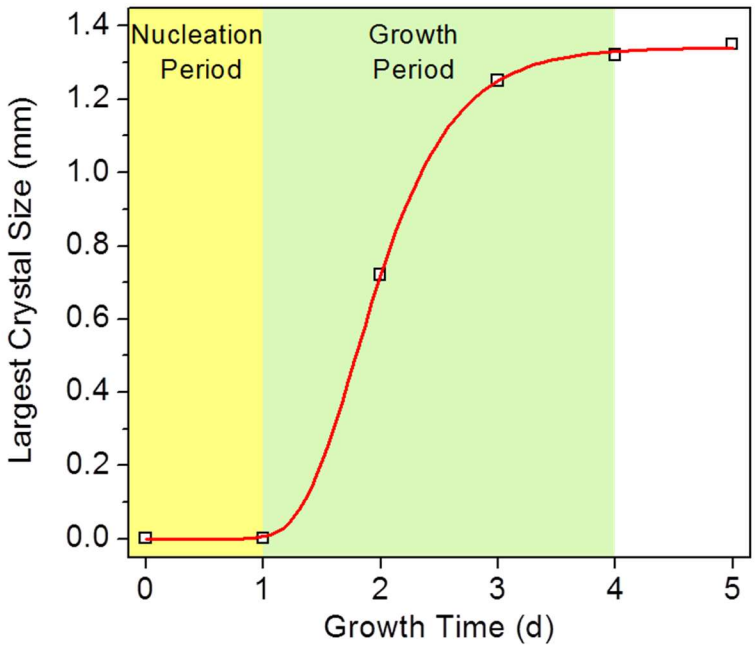

Figure 3.4 Increase of Cu-BTC crystal size as a function of reaction time measured at NC State.

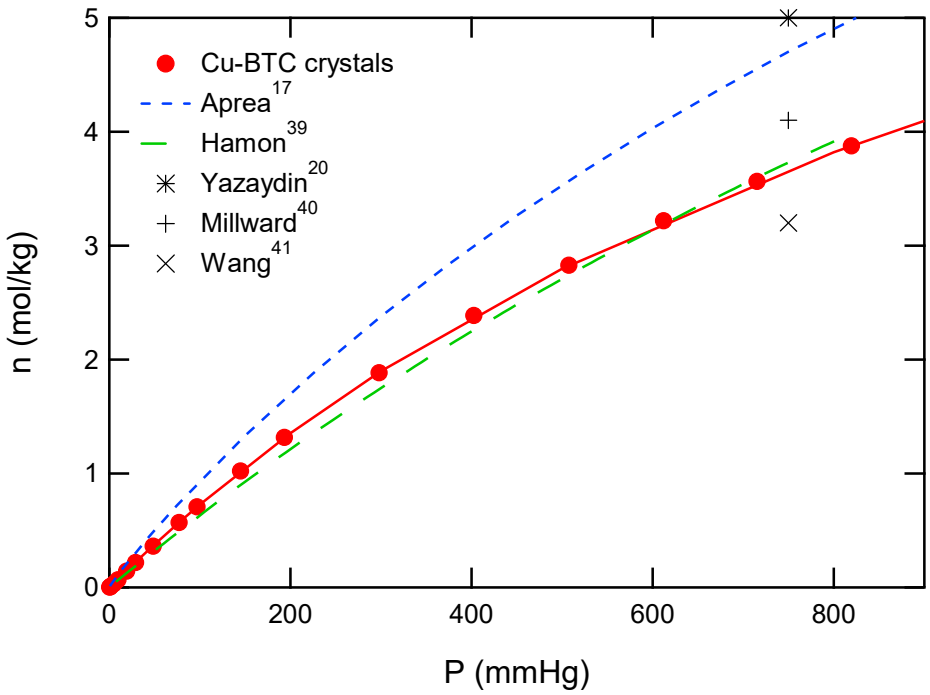

Figure 3.5 Gravimetric CO_2 isotherm on large Cu-BTC single crystals at 298 K fit by a Toth isotherm model. Also shown are data points from literature isotherms of CO_2 on powder Cu-BTC at 298 K.

the Cu-BTC crystals at 25 °C. The adsorbent sample used was a mix of various crystal sizes. A Toth isotherm model fits the data well. Also plotted on the figure are CO_2 isotherm data on Cu-BTC powder from the literature. Curves show isotherms based on fitting parameters for a Langmuir fit from Hamon et al.[39] and a Sips fit from Aprea et al.[17] Select data points at 1 bar were also taken from Yazaydin et al.,[20] Millward and Yaghi,[40] and Wang et al.[41] Due to the high porosity of Cu-BTC, most isotherms in the literature focused on higher pressure data; however, it is clear that the isotherm on the large single crystals compares favorably with powder samples at lower CO_2 pressures. This is important as the diffusion measurements were made at low CO_2 concentrations.

Figure 3.6 shows CSFR curves for Cu-BTC single crystals and for a powder Cu-BTC sample at a gas-phase concentration of 0.5% CO_2. Fits based on a micropore diffusion model are shown; for the single crystal sample the micropore diffusion model accurately describes the data but cannot describe the data for the powder sample. When comparing the curves, the powder sample has a much steeper slope, which indicates faster uptake. Even though the two samples have the same pore structure and the same intermolecular interactions with CO_2, and therefore the same micropore diffusion constant, the diffusion length scale of the powder samples is much smaller due to the micron-sized crystals. This decreases the importance of micropore diffusion in the sample and increases the influence of other diffusive mechanisms, such as a surface barrier or external mass transfer. The presence of other significant diffusive mechanisms explains why the micropore diffusion model fails to fit the powder data well. The diffusion length scale can be increased by pressing the powder into a pellet, but that introduces interstices between the crystals and adds macropore diffusion in those spaces, which is then the potentially dominant mass transfer mechanism.[34] For the millimeter size single crystals, the orders of magnitude increase in the

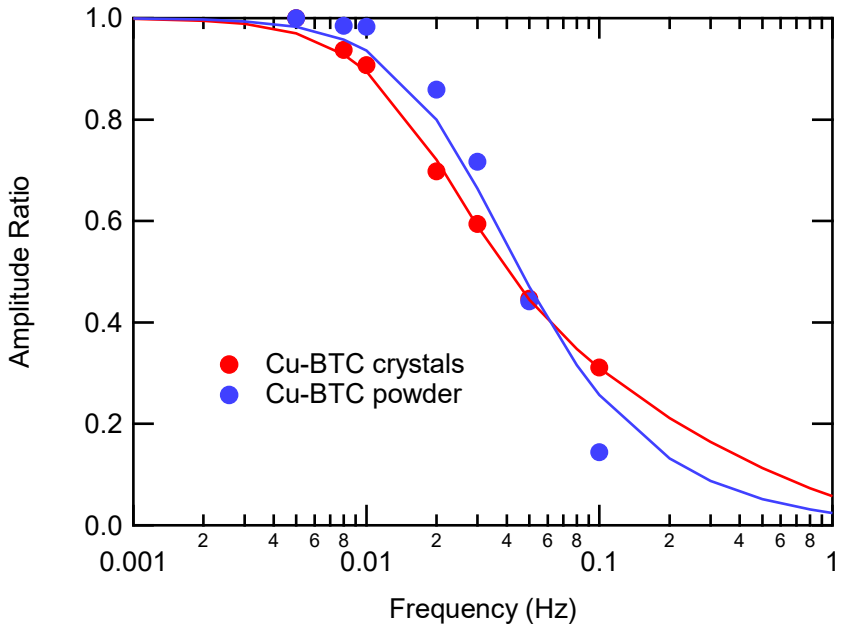

Figure 3.6. Amplitude ratio curves for CSFR experiments on large Cu-BTC single crystals versus a powder sample.

micropore diffusion length scale makes it the dominant rate limiting mass transfer mechanism, ensuring that measured diffusion coefficients are from diffusion in the micropores of the MOF.

Figure 3.7 shows CSFR curves at various gas-phase concentrations on a sample of Cu-BTC crystals that are approximately 0.7 mm in diameter. The steady state gas-phase concentrations were 0.1%, 0.5%, and 10% CO_2 and the micropore diffusion model accurately fits the data at each concentration. The curves are nearly identical for the 0.1 and 0.5% experiments while the 10% curve is shifted to higher amplitude ratios.

The micropore diffusion model uses a two parameter fit; the regressed values are the local isotherm slope, K, and the micropore diffusion coefficient parameter D_s/R^2, where R is the diffusion length scale. Table 3.1 reports the CSFR fitting parameters for the CSFR curves at each concentration as well as for a similar set of experiments on BPL activated carbon, shown in Figure 3.8. BPL is a predominantly microporous activated carbon, and the micropore diffusion model has been found to accurately describe the diffusion of various compounds in BPL.[42] The regressed CSFR isotherm slopes are also compared to slopes calculated from the Toth fit of the CO_2 isotherm measured on the Cu-BTC crystals from Figure 3.5. The CSFR K values are slightly higher than those measured by the CO_2 isotherm but the trends are very similar. For the 0.1% and 0.5% experiment, the isotherm slopes are not significantly different, which agrees with the near linear shape of the CO_2 isotherm at such low concentrations. For the 10% experiment, there is a significant decrease in the isotherm slope for both the CSFR regressed value and the values calculated from the adsorption isotherm.

Interesting trends are apparent in the diffusion coefficients. For the single crystal Cu-BTC samples, there is no significant difference from the 0.1% to the 10% sample. For BPL activated carbon, a near order of magnitude increase in the diffusion coefficient is found as the gas-phase

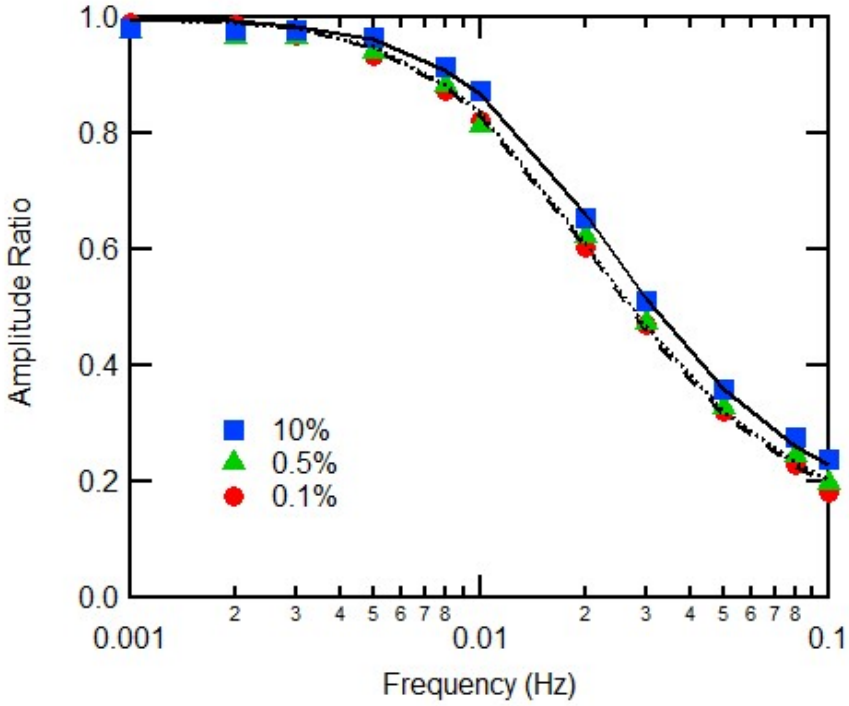

Figure 3.7 CSFR curves at various CO_2 concentrations on Cu-BTC crystals of approximately 0.7 mm.

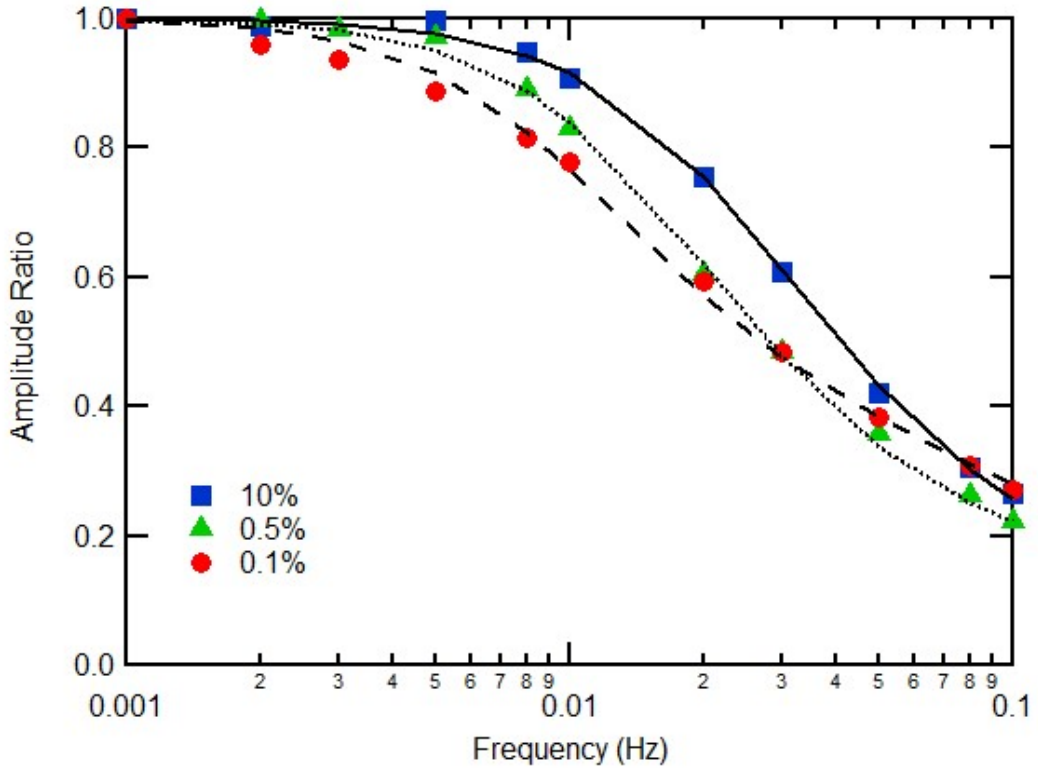

Figure 3.8 CO_2 CSFR curves on BPL activated carbon at varying concentrations.

Table 3.1 Micropore diffusion fitting parameters for 0.7 mm Cu-BTC single crystals and BPL activated carbon at different CO_2 concentrations.

	Cu-BTC CSFR		*BPL CSFR*		*Cu-BTC isotherm*
Conc	K	D_s/R^2	K	D_s/R^2	K
%	(mol/kg·bar)	(1/s)	(mol/kg·bar)	(1/s)	(mol/kg·bar)
0.1	6.9	0.0090	4.9	0.0024	5.9
0.5	6.7	0.0086	4.2	0.0072	5.8
10	5.8	0.0089	2.8	0.0142	5.1

concentration increases from 0.1% to 10%. These trends make sense based on the heterogeneity of the samples. Cu-BTC is a crystalline material that has many uniform sites. Thus, the interaction between the adsorbate and the adsorption sites for CO_2 molecules that adsorb at low pressure will still be similar for additional CO_2 molecules that adsorb at higher pressures. This agrees well with literature. From Wang et al.[41] the heat of adsorption of CO_2 decreases about 10% from the zero loading value and then remains virtually constant as loading increases. The activated carbon is very heterogeneous, so the first CO_2 molecules will adsorb to stronger adsorption sites and will diffuse more slowly than at higher pressures.

In comparison with the MOF, the BPL activated carbon particles were larger, approximately 2 mm in diameter. After normalizing by the diffusion length scale, the diffusion coefficient for the single crystals is significantly slower than in the activated carbon. This could be due to strong intermolecular interaction between CO_2 and the open metal sites of Cu-BTC. It could also be due to the small uniform 9 Å pores of Cu-BTC, whereas the activated carbon has a wide distribution of pore sizes.

Due to the single crystal morphology, the micropore diffusion length scale is the full dimension of the particle. As such, CSFR experiments that vary the particle size will give different D_s/R^2 parameters but should still calculate similar micropore diffusion coefficients when normalized by particle size. Three different sets of Cu-BTC crystals with particle sizes of 0.7±0.1

mm, 1±0.1 mm, and 1.3±0.1 mm were prepared. Figure 3.9 shows CSFR curves at 0.5% CO_2 for each set of crystals and micropore diffusion fitting parameters are given in Table 3.2. The regressed isotherm slopes show good agreement between the different crystal sizes. The D_s/R^2 values are expected to decrease as the crystal size increases; however, the 1.3 mm crystals show an increase compared to the 1 mm crystals.

Table 3.2 Micropore diffusion fitting parameters for various Cu-BTC crystal sizes at 0.5% CO_2.

Crystal Size (mm)	*K (mol/kg·bar)*	*D_s/R^2 (1/s)*	*D_s (m^2/s)*
0.7	6.7	0.0086	4.1×10^{-10}
1	6.4	0.0041	3.2×10^{-10}
1.3	7.1	0.0056	6.4×10^{-10}

One possible reason for the discrepancy in the D_s/R^2 trend is that the model assumes a spherical particle shape that may not accurately represent the crystals. The particle size of each crystal was determined by measuring the longest dimension. However, the crystal growth is not uniform in every direction which can result in diffusion length scales that are smaller than expected. Figure 3.10 shows crystal mass as a function of the longest measured dimension. It was found that a power law fit the data well with an exponent of 2.14 instead of the expected cubic function for a perfect sphere. To account for the uneven growth in each dimension, an effective diffusion length scale was calculated from

$$mass = \rho \frac{4}{3} \pi R_{eff}^3 = 0.52 R_{measured}^{2.14} \tag{3.1}$$

Where mass is in milligrams, $R_{measured}$ is half of the length of the longest crystal dimension in millimeters, and ρ is the crystal density, 1.29 g/cm^3. When normalized by R_{eff}, the micropore diffusion coefficients agree fairly well and give an average value of 5×10^{-10} m^2/s. This value is on the same order of magnitude as several other CO_2 diffusion rates reported in other MOFs.

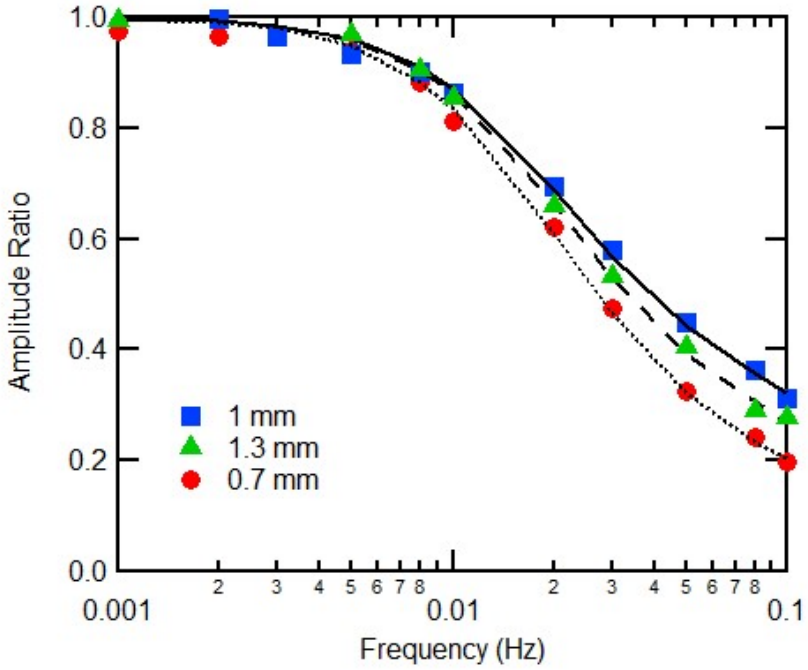

Figure 3.9 CSFR curves for different Cu-BTC crystal sizes at 0.5% CO_2 concentrations.

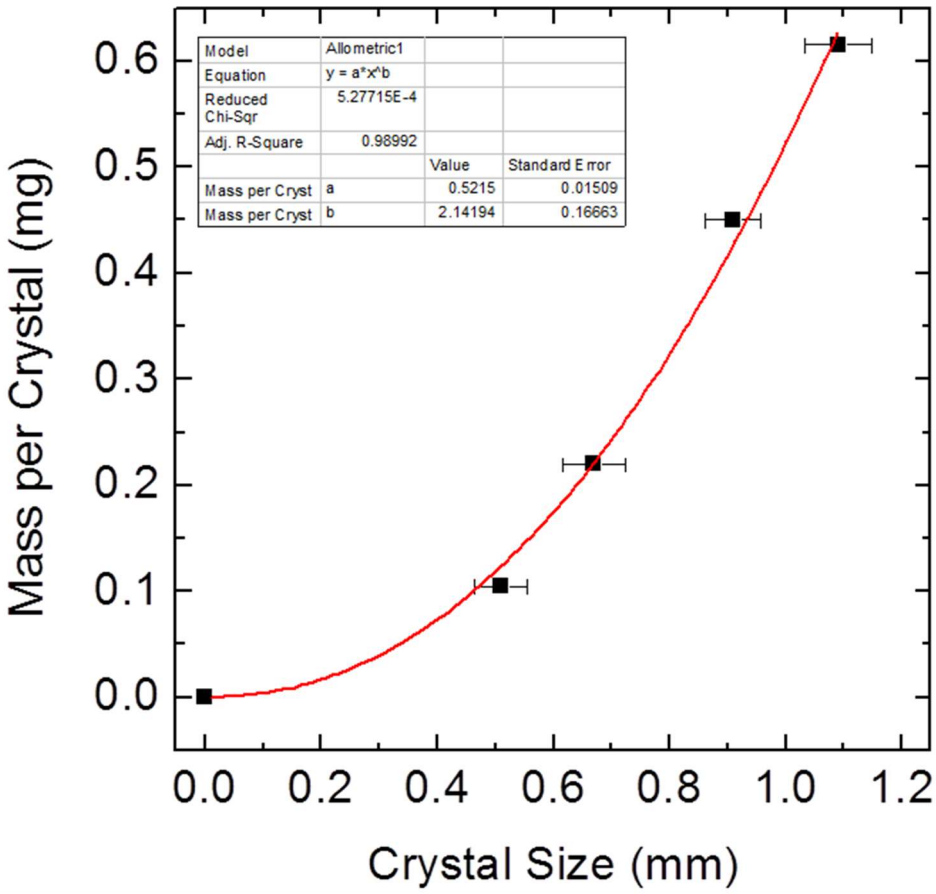

Figure 3.10 The correlation between the mass per crystal and the crystal dimension measured at NC State. The error bar indicates the standard deviation of the crystal sizes in a mass measurement group.

3.4 Conclusions

A new synthesis procedure to produce large millimeter size single crystals of Cu-BTC has been reported. Crystal size could be accurately controlled by length of the synthesis time. Properties measured by XRD, BET, TGA, and CO_2 isotherms on the Cu-BTC crystals agree well with Cu-BTC powders produced by traditional solvothermal synthesis. The increased length scale of the microporous domain makes diffusion measurements easier as it limits the impact of multiple mass transfer mechanisms. CSFR experiments were performed which verified micropore diffusion as the rate controlling diffusive mechanism. Diffusion coefficients measured at varying concentrations show very little dependence on loading up to about 0.1 bar, the highest pressure considered. At 0.5% gas-phase concentration of CO_2 in He, the measured diffusion coefficient is approximately 5×10^{-10} m^2/s.

References

1. Kim, J.; Chen, B.; Reinike, T. M.; Li, H.; Eddaoudi, M.; Moler, D. B.; O'Keeffe, M.; Yaghi, O. M. Assembly of Metal-Organic Frameworks from Large Organic and Inorganic Secondary Building Units: New Examples and Simplifying Principles for Complex Structures. *J. Am. Chem. Soc.* **2001**, 123, 8239-8247.
2. Furukawa, H.; Ko, N.; Go, Y. B.; Aratani, N.; Choi, S. B.; Choi, E.; Yazaydin, A. O.; Snurr, R. Q.; O'Keeffe, M.; Kim, J.; Yaghi, O. M. Ultrahigh porosity in metal-organic frameworks. *Science* **2010**, 329, 424-428.
3. Farha, O. K.; Yazaydin, A. O.; Eryazici, I.; Malliakas, C. D.; Hauser, B. G.; Kanatzidis, M. G.; Nguyen, S. T.; Snurr, R. Q.; Hupp, J. T. De novo synthesis of a metal-organic framework material featuring ultrahigh surface area and gas storage capacities. *Nat. Chem.* **2010**, 2, 944-948.
4. Farha, O. K.; Eryazici, I.; Jeong, N. C.; Hausert, B. G.; Wilmer, C. E.; Sarjeant, A. A.; Snurr, R. Q.; Nguyent, S. T.; Yazaydin, A. O.; Hupp, J. T. Metal-organic framework materials with ultrahigh surface areas: is the sky the limit? *J. Am. Chem. Soc.* **2012**, 134, 15016-15021.
5. Grunker, R.; Bon, V.; Muller, P.; Stoeck, U.; Krause, S.; Mueller, U.; Senkovska, I.; Kaskel, S. A new metal-organic framework with ultra-high surface area. *Chem. Commun.* **2014**, 50, 3450-3452.
6. Wang, T. C.; Bury, W.; Gomez-Gualdron, D. A.; Vermeulen, N. A.; Mondloch, J. E.; Deria, P.; Zhang, K.; Moghadam, P. Z.; Sarjeant, A. A.; Snurr, R. Q.; Stoddart, J. F.; Hupp, J. T.; Farha, O. K. Ultrahigh surface area zirconium MOFs and insights into the applicability of the BET theory. *J. Am. Chem. Soc.* **2015**, 137, 3585-3591.

7. Wilmer, C. E.; Leaf, M.; Lee, C. Y.; Farha, O. K.; Hauser, B. G.; Hupp, J. T.; Snurr, R. Q. Large-scale screening of hypothetical metal-organic frameworks. *Nat. Chem.* **2012**, 4, 83-89.
8. Li, J.-R.; Kuppler, R. J.; Zhou, H.-C. Selective gas adsorption and separation in metal-organic frameworks. *Chem. Soc. Rev.* **2009**, 38, 1477-1504.
9. Getman, R. B.; Bae, Y.-S.; Wilmer, C. E.; Snurr, R. Q. Review and analysis of molecular simulations of methane, hydrogen, and acetylene storage in metal-organic frameworks. *Chem. Rev.* **2012**, 112, 703-723.
10. Corma, A.; Garcia, H.; Xamena, L. I. Engineering metal organic frameworks for heterogeneous catalysis. *Chem. Rev.* **2010**, 110, 4606-4655.
11. Kreno, L. E.; Leong, K.; Farha. O. K.; Allendorf, M.; Van Duyne, R. P.; Hupp, J. T. Metal-organic framework materials as chemical sensors. *Chem. Rev.* **2012**, 112, 1105-1125.
12. Sumida, K.; Rogow, D. L.; Mason, J. A.; McDonald, T. M.; Bloch, E. D.; Herm, Z. R.; Bae, T.-H.; Long, J. R. Carbon dioxide capture in metal-organic frameworks. *Chem. Rev.* **2012**, 112, 724-781.
13. Li, J.-R.; Ma, Y.; McCarthy, M. C.; Sculley, J.; Yu, J.; Jeong, H.-K.; Balbuena, P. B.; Zhou, H.-C. Carbon dioxide capture-related gas adsorption and separation in metal-organic frameworks. *Coordin. Chem. Rev.* **2011**, 255, 1791-1823.
14. Keskin, S.; van Heest, T. M.; Sholl, D. D. Can Metal-Organic Framework Materials Play a Useful Role in Large-Scale Carbon Dioxide Separations? *ChemSusChem,* **2010**, 3, 879-891.
15. Chui, S. S.-Y.; Lo, S. M.-F.; Charmant, J. P. H.; Orpen, A. G.; Williams, I. D. A chemically functionalizable nanoporous material $[Cu_3(TMA)_2(H_2O)_3]_n$. *Science,* 1999, 283, 1148-1150.

16. Vishnyakov, A.; Ravikovitch, P. L.; Neimark, A. V.; Bulow M.; Wang, Q. M. Nanopore structure and sorption properties of Cu-BTC metal-organic framework. *Nano Lett.* **2003**, 3, 713-718.

17. Aprea, P.; Caputo, D.; Gargiulo, N.; Iucolano, F.; Pepe, F. Modeling carbon dioxide adsorption on microporous substrates: Comparison between Cu-BTC metal-organic framework and 13X zeolitic molecular sieve. *J. Chem. Eng. Data* **2010**, 55, 3655-3661.

18. Chowdhury, P.; Bikkina, C.; Meister, D.; Dreisbach, F.; Gumma, S. Comparison of adsorption isotherms on Cu-BTC metal organic frameworks synthesized from different routes. *Micropor. Mesopor. Mat.* **2009**, 117, 406-413.

19. Moellmer, J.; Moeller, A.; Dreisbach, F.; Glaeser, R.; Staudt, R. High pressure adsroption of hydrogen, nitrogen, carbon dioxide and methane on the metal-organic framework HKUST-1. *Micropor. Mesopor. Mat.* **2011**, 138, 140-148.

20. Yazaydin, A. O.; Benin, A. I.; Faheem, S. A.; Jakubczak, P.; Low, J. J.; Willis R. R.; Snurr, R. Q. Enhanced CO_2 adsorption in metal-organic frameworks via occupation of open-metal sites by coordinated water molecules. *Chem. Mater.* **2009**, 21, 1425-1430.

21. Yang, Q.; Zhong, C. Understanding hydrogen adsorption in metal-organic frameworks with open metal sites: a computational study. *J. Phys. Chem. B* **2006**, 110, 17776-17783.

22. Liu, B.; Smit, B. Comparative molecular simulation study of CO_2/N_2 and CH_4/N_2 separation in zeolites and metal-organic frameworks. *Langmuir* **2009**, 25, 5918-5926.

23. Yang, Q.; Xue, C.; Zhong C.; Chen, J.-F. Molecular simulation of separation of CO_2 from flue gases in Cu-BTC metal-organic framework. *AIChE J.* **2007**, 53, 2832-2840.

24. Cavenati, S.; Grande C. A.; Rodrigues, A. E. Metal organic framework adsorbent for biogas upgrading. *Ind. Eng. Chem. Res.* **2008**, 47, 6333-6335.

25. Liang, Z.; Marshall, M.; Chaffee, A. L. CO_2 adsorption-based separation by metal organic framework (Cu-BTC) versus zeolite (13X). *Energ. Fuel.* **2009**, 23, 2785-2789.

26. Adatoz, E.; Avci A. K.; Keskin, S. Opportunities and challenges of MOF-based membranes in gas separations. *Sep. Purif. Technol.* **2015**, 152, 207-237.

27. Salles, F.; Jobic, H.; Devic, T.; Llewellyn, P. L.; Serre, C.; Ferey, G.; Maurin, G. Diffusion of H_2, alkanes and CO_2 in rigid and flexible metal-organic framework materials using a combination of molecular dynamics and neutron scattering measurements. *ACS Nano* **2010**, 4, 143-152.

28. Sabouni, R.; Kazemian, H.; Rohani, S. Carbon Dioxide adsorption in microwave-synthesized metal organic framework CPM-5: Equilibrium and kintics study. *Micropor Mesopor Mater.* **2013**, 175, 85-91.

29. Saha, D.; Bao, Z.; Jia, F.; Deng, S. Adsorption of CO_2, CH_4, N_2O, and N_2 on MOF-5, MOF-177, and zeolite 5A. *Environ. Sci. Technol.* **2010**, 44, 1820-1826.

30. Zhao, Z.; Li, Z.; Lin, Y. S. Adsorption and diffusion of carbon dioxide on metal-organic framework (MOF-5). *Ind. Eng. Chem. Res.* **2009**, 48, 10015-10020.

31. Heinke, L.; Gu, Z.; Woll, C. The surface barrier phenomenon at the loading of metal-organic frameworks. *Nature Communications* **2014**, 5, 4562, 1-6.

32. Fletcher, A. J.; Cussen, E. J.; Prior, T. J.; Rosseinsky, M. J.; Kepert C. J.; Thomas, K. M. Adsorption dynamcis of gases and vapors on the nanoporous metal organic framework material Ni_2(4,4'-bipyridine)$_3$(NO_3)$_4$: Guest modification of host sorption behavior. *J. Am. Chem. Soc.* **2001**, 123, 10001-10011.

33. Hu, X.; Brandani, S.; Benin A. I.; Willis, R. R. Development of a Semiautomated Zero Length Column Technique for Carbon Capture Applications: Study of Diffusion Behavior of CO_2 in MOFs. *Ind. Eng. Chem. Res.* **2015**, 54, 5777-5783.

34. Liu, J.; Wang, Y.; Benin, A. I.; Jakubczak, P.; Willis, R. R.; LeVan, M. D. CO_2/H_2O adsorption equilibrium and rates on metal-organic frameworks: HKUST-1 and Ni/DOBDC. *Langmuir* **2010**, 26, 14301-14307.

35. Wang, Y.; LeVan, M. D. Nanopore diffusion rates for adsorption determined by pressure-swing and concentration-swing frequency response and comparison with Darken's equation. *Ind. Eng. Chem. Res.* **2008**, 47, 3121-3128.

36. Wang, Y.; LeVan, M. D. Master curves for mass transfer in bidisperse adsorbents for pressure-swing and volume-swing frequency response methods. *AIChE J.* **2011**, 57 (8), 2054-2069.

37. Zhao, J.; Nunn, W. T.; Lemaire, P. C.; Lin, Y.; Dickey, M. D.; Oldham, C. J.; Walls, H. J.; Peterson, G. W.; Losego, M. D.; Parsons, G. N. Facile Conversion of Hydroxy Double Salts to Metal-Organic Frameworks Using Metal Oxide Particles and Atomic Layer Deposition Thin-Film Templates. *J. Am. Chem. Soc.* **2015**, *137* (43), 13756–13759.

38. Li, L.; Sun, F.; Jia, J.; Borjigin, T.; Zhu, G. Growth of large single MOF crystals and effective separation of organic dyes. *Crystengcomm* **2013**, *15* (20), 4094–4098.

39. Hamon, L.; Jolimaitre, E.; Pirngruber, G. D. CO_2 and CH_4 separation by adsorption using Cu-BTC metal-organic framework. *Ind. Eng. Chem. Res.* **2010**, 49, 7497-7503.

40. Millward, A. R.; Yaghi, O. M. Metal-organic frameworks with exceptionally high capacity for storage of carbon dioxide at room temperature. *J. Am. Chem. Soc.* **2005**, 127, 17998-17999.

41. Wang, Q. M.; Shen, D.; Bulow, M.; Lau, M. L.; Deng, S.; Fitch, F. R.; Lemcoff, N. O.; Semanscin, J. Metallo-organic molecular sieve for gas separation and purification. *Micropor. Mesopor. Mat.* **2002**, 55, 217-230.

42. Wang, Y.; Mahle, J. J.; Furtado, A. M. B.; Glover, T. G.; Buchanan, J. H.; Peterson G. W.; LeVan, M. D. Mass transfer and adsorption equilibrium for low volatility alkanes in BPL activated carbon. *Langmuir* **2013**, 29, 2935-2945.

CHAPTER IV

DIFFUSION OF CO_2 AND ETHANE IN BIDISPERSE PELLETS OF UIO-66 AND AMINE FUNCTIONALIZED UIO-66

4.1 Introduction

Metal-organic frameworks (MOFs) are highly porous crystalline materials that contain metal clusters interconnected by organic linkers.[1] High porosity and surface area make MOFs good candidates for adsorption applications that currently use zeolites or carbons.[2] A major benefit of using MOFs is the high degree of tunability of physical and chemical properties that can be obtained by varying the metal center and organic linker building blocks;[3] simulations have shown that there are over 100,000 possible combinations.[4] In addition to the variation of building blocks, both the metal centers and organic linkers are amenable to chemical functionalization through methods such as solvent assisted ligand incorporation (SALI),[5] solvent assisted ligand exchange (SALE),[6] and cation exchange.[7] While these properties make MOFs promising candidates for next generation adsorbents, a major drawback compared to zeolites and carbons is chemical stability.[8]

Unlike many other MOFs, the zirconium (Zr) based UiO-66 is chemically stable under humid and acidic conditions.[9,10] This stability has led to interest of using functionalized UiO-66 analogs as adsorbents in chemical filters. Several MOFs have been tested as adsorbents for toxic industrial chemicals (TICs) and chemical warfare agent simulants.[11] UiO-66 and several functionalized UiO-66 analogs have been tested as filters for ammonia (NH_3) and cyanogen chloride (CNCl).[12,13] The analogs tested for NH_3 removal are UiO-66-OH, UiO-66-$(OH)_2$, UiO-

66-NO_2, UiO-66-SO_3H, UiO-66-$(COOH)_2$.[12] It was found that the acidic functionalities –COOH and –SO_3H are not beneficial for the adsorption of the basic NH_3 compound, possibly due to steric hindrance effects. The best ammonia adsorbents were the UiO-66-OH and UiO-66-NH_2 analogs.

UiO-66-NH_2 was further studied for the impacts of physical processing.[13] The synthesized powder form of the MOFs is undesirable in gas masks due to pressure drop across the adsorbent bed. UiO-66-NH_2 was pelletized at different pressures ranging from 5000 psi to 100,000 psi. It was found that pellets pressed up to 25,000 psi maintained similar physical characteristics such as surface area and pore volume.[13] Significant loss of cyrstallinity occurred at pressures above 25,000 psi as evidenced by XRD and FTIR. Despite the lack of physical differences in pellets pressed up to 25,000 psi, breakthrough curve testing revealed a loss of capacity in the pelletized samples as compared to the as-synthesized powder. This is hypothesized to be due to mass transfer limitations in the pellets.[13]

The purpose of this work is to better understand mass transfer in UiO-66 pellets. Two MOFs, UiO-66 and UiO-66-NH_2, were pelletized at different pressures and with different thicknesses, and tested for diffusion of non-reactive adsorbates. The MOF pellets represent a bidisperse adsorbent that has macropore interstices between small microporous crystallites. This morphology leads to the presence of multiple mass transfer mechanisms that can impact diffusion rates. Frequency response techniques can be used to help distinguish between the rate-limiting mass transfer mechanisms.[14] Volume-swing frequency response (VSFR) has been previously used to measure diffusion in zeolite pellets,[15] and concentration-swing frequency response (CSFR) has been used to measure CO_2 diffusion in pellets of the MOFs Cu-BTC and Ni-DOBDC.[16] In this paper, we use CSFR to measure diffusion of CO_2 and ethane in pellets of two UiO-66 analogs.

4.2 Experiments

4.2.1 Materials

UiO-66 and UiO-66-NH_2 were synthesized at the Edgewood Chemical Biological Center (ECBC) according to the procedure described by Peterson et al.[13] The synthesized powders were pelletized at ECBC using a Carver press. Research grade helium, carbon dioxide, 1% CO_2 in balance helium, and 1% ethane in balance helium gas tanks were purchased from Air Liquide.

4.2.2 Experimental Measurements

Pure CO_2 isotherms were measured at room temperature using a Micromeritics ASAP 2020. Approximately 100 mg of sample was degassed at 90 °C for at least 8 hours. The sample was then weighed and the isotherm was measured using volumetric methods.

Diffusion phenomena were measured using the CSFR apparatus shown in Figure 2.1. Approximately 25 mg of adsorbent was regenerated for 8 hours under vacuum at 90 °C for accurate weight measurement. The sample was then loaded into a shallow bed and placed under vacuum at room temperature with a 1 sccm He flow for 16 hours. A 1% CO_2 in He or a 1% ethane in He stream was mixed with a pure He stream upstream of the adsorbent bed. Both streams were controlled with MKS mass flow controllers to create a 1000 ppm steady-state concentration. The pressure in the adsorbent bed was controlled at 1 bar by a MKS Baratron pressure controller, and effluent gas from the adsorbent bed was sampled by an Agilent 5975 mass spectrometer.

The system was allowed to reach steady-state and then the mass flow controllers were used to introduce sinusoidal perturbations to the flowrates of each stream but 180 degrees out of phase. The resulting feed stream to the adsorbent bed had a constant flow rate with a sinusoidal concentration swing around the steady-state gas-phase concentration.

The perturbations were performed at different frequencies in the range of 0.002 to 0.1 Hz.

The collected data are presented as plots of the amplitude ratio (AR) as a function of the perturbation frequency, where the AR is calculated from the amplitude of the concentration oscillations in the gas exiting the adsorbent bed divided by the amplitude in the gas concentration entering the adsorbent bed. The diffusion mechanism and rate parameters can be extracted by fitting the data to a mathematical model derived from transfer functions.

4.2.3 Mathematical Model

Detailed mathematical models for a CSFR apparatus have been described elsewhere;[17] however, a brief description is provided here. For a bidisperse particle, the two main mass transfer mechanisms are for diffusion in the macropore region throughout the scale of the entire pellet and diffusion in microporous domains that are on the length scale of the powder crystallites. For micropore diffusion in a spherical domain, the differential mass balance is given by

$$\frac{\partial n}{\partial t} = \frac{1}{r^2}\frac{\partial}{\partial r}\left(D_s r^2 \frac{\partial n}{\partial r} \right) \tag{4.1}$$

$$n = n^* at \quad r = r_s \tag{4.2}$$

$$\frac{\partial n}{\partial r} = 0 \ at \ r = 0 \tag{4.3}$$

where n is the adsorbed phase concentration, n^* is the equilibrium adsorbed concentration which is known from equilibrium isotherms, r is the radial coordinate, r_s is the radius of the microporous domain, D_s is the micropore (surface) diffusivity, and t is time. For macropore diffusion, the governing equation is given by

$$\rho_p \frac{\partial n}{\partial t} + \varepsilon_p \frac{\partial c_p}{\partial t} = \frac{\varepsilon_p D_p}{r^2}\frac{\partial}{\partial r}\left(r^2 \frac{\partial c_p}{\partial r} \right) \tag{4.4}$$

$$c_p = c \quad \text{at} \quad r = R_p \tag{4.5}$$

$$\frac{\partial c_p}{\partial r} = 0 \quad \text{at} \quad r = 0 \tag{4.6}$$

where ρ_p is the particle density, ε_p is the macroporosity, c_p is the gas-phase concentration in the macropores, and R_p is the radius of the macropore domain. For a linearized system, the adsorbed phase concentration is in equilibrium with the gas phase concentration in the macropores such that

$$n = Kc_p \tag{4.7}$$

where K is the local isotherm slope.

Inserting equation 4.7 into 4.4 gives

$$\frac{\partial c_p}{\partial t} = \frac{D_p / r^2}{\rho_p K / \varepsilon_p + 1} \frac{1}{r^2} \frac{\partial}{\partial r}\left(r^2 \frac{\partial c_p}{\partial r} \right) \tag{4.8}$$

which has the same functional form as equation 4.1. As a result, any data set that can be fit by the micropore diffusion model will be fit equally well by the macropore diffusion model. Both the micropore and macropore model can be solved by Laplace transform to give the adsorbed phase transfer function[17]

$$G_n(s) = \frac{\overline{n}}{\overline{P}} = \frac{3K'}{s/\eta}\left[\sqrt{s/\eta}\coth\left(\sqrt{s/\eta} - 1\right)\right] \tag{4.9}$$

where K' is an isotherm slope parameter, η is a mass transfer parameter, and s is the Laplace domain complex argument. While the regressed K' and η will be the same for any given data set, they represent different parameters depending on the model chosen and are related by

$$K \Leftarrow K' \Rightarrow K + \varepsilon_p / \rho_p \tag{4.10}$$

$$D_s / r_s^2 \Leftarrow \eta \Rightarrow \frac{D_p / r_p^2}{\rho_p K / \varepsilon_p + 1} \tag{4.11}$$

where the micropore and macropore diffusion parameters are given by the left hand side and right hand side, respectively, of equation 4.10 and 4.11. Both models represent isothermal conditions

which is a good assumption for flow through systems.[18]

4.3 Results and Discussion

UiO-66 and UiO-66-NH_2 were both pressed into pellets at pressures of 5,000 psi and 25,000 psi with three different thicknesses at each pressure, resulting in a matrix of 12 samples. To evaluate the macropore diffusion model, the physical characteristics of each pellet, including macropore diffusion length scale, pellet density, and macroporosity are needed. The pellets were pressed into a cylindrical shape with a radius of 6.5 mm, and a caliper was used to measure the height of each pellet sample. Each sample was weighed and the dimensions were used to calculate the pellet density. An average density was calculated from the three thicknesses for each material and pressure combination. Macroporosity was estimated using

$$\varepsilon_p = 1 - \frac{\rho_p}{\rho_s} \tag{4.12}$$

where ρ_s is the skeletal density. Skeletal densities of 1238 and 1295 kg/m^3 were used for UiO-66 and UiO-66-NH_2 respectively, based on simulations of the ideal crystalline unit cell by Yang et al.[19] Table 4.1 summarizes these values.

When pressed, the pellet thickness is much less than the radius of the die set so, if used in whole pellet form, diffusion would best be described using a slab model and one-dimensional diffusion. However, the shallow adsorption bed used only has a 4 mm diameter, thus the pellets were broken up into smaller pieces with width and length dimensions of approximately 3 mm. For the thinnest pellets, there is still an order of magnitude difference between the thickness and the next smallest dimension so a one-dimensional slab model may still accurately describe diffusion; but in the thick pellets that assumption fails as all of the dimensions of the pellets are similar. In order to compare data from the different pellet sizes, as an approximation, an effective radius was

Table 4.1 Summary of pressed pellet physical characteristics.

Sample	*Pressure (psi)*	*Thickness (mm)*	ρ_p *(kg/m³)*	ε_p	r_p *(mm)*
UiO-66	5000	0.41	727	0.41	0.46
		0.87			0.83
		2.41			1.39
	25000	0.34	928	0.25	0.41
		0.69			0.71
		1.75			1.12
UiO-66-NH2	5000	0.39	686	0.47	0.46
		0.94			0.87
		1.93			1.27
	25000	0.25	989	0.24	0.32
		0.58			0.63
		1.28			1.04

calculated by equating the ratio of volume to surface area of an ideal spherical shape to a slab like shape as given by

$$\frac{V}{SA} = \frac{4\pi\, r_p^3 / 3}{4\pi\, r_p^2} = \frac{LWH}{2LW + 2LH + 2WH} \tag{4.13}$$

where the length and width are estimated to be 3 mm. In the limit as pellet thickness goes to zero, the effective macropore diffusion length scale is $3H/2$; as the pellets approach a cubic shape, the length scale goes to $H/2$. The effective macropore diffusion length is also given in Table 4.1.

Figure 4.1 shows amplitude ratio curves for CO_2 and ethane CSFR experiments on each pellet sample at 1000 ppm gas-phase concentration. All curves were fit with the spherical diffusion model and the regressed isotherm slope parameter, and mass transfer parameter are summarized in Table 4.2. For the majority of the pellet samples, the spherical diffusion model fits the data well. The exception is for experiments on the UiO-66 samples pressed at 5,000 psi. For these samples, the CSFR curves are steeper than the model predicts, which indicates very rapid uptake similar to powder samples.

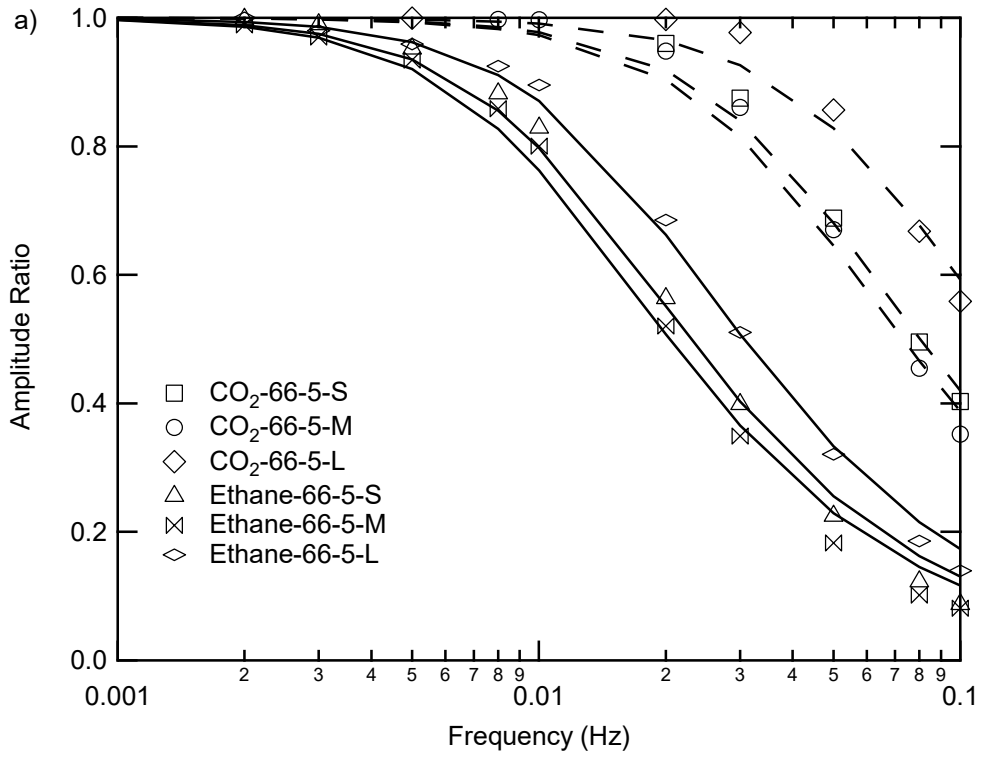

Figure 4.1 CSFR amplitude ratio curves for both CO_2 and ethane on varying thicknesses of (a) UiO-66 pressed at 5000 psi, (b) UiO-66-NH_2 pressed at 5,000 psi, (c) UiO-66 pressed at 25,000 psi, and (d) UiO-66-NH_2 pressed at 25,000 psi. The legend notation gives pellet thickness as S for the thinnest pellet, M for the medium thickness, and L for the thickest pellet.

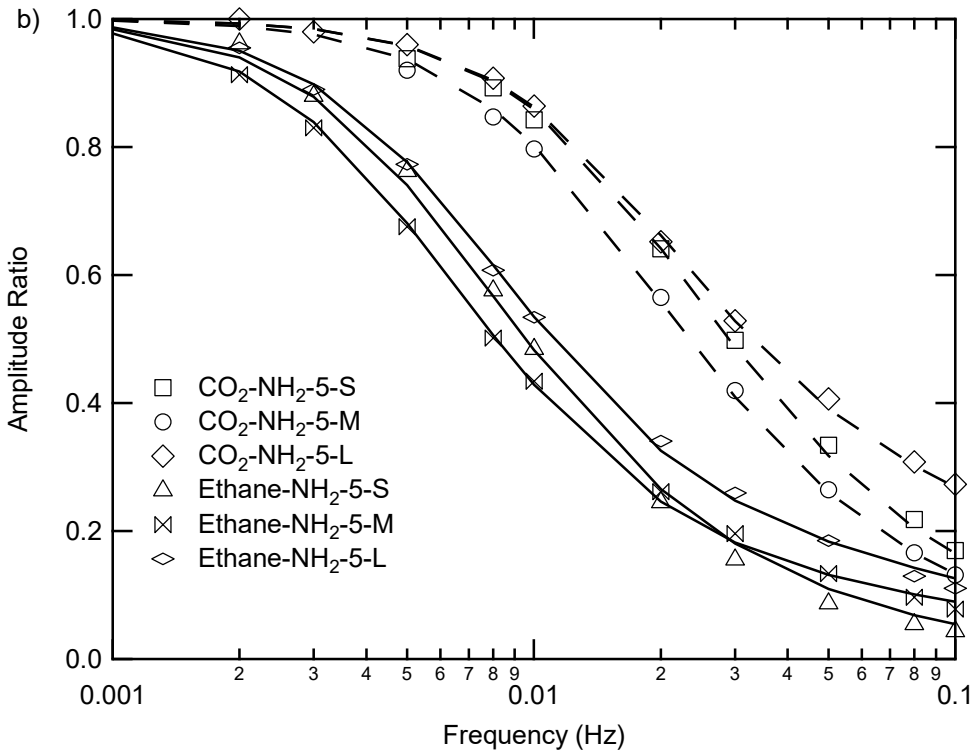
b)
1.0
0.8
0.6
0.4
0.2
0.0
Amplitude Ratio
CO2-NH2-5-S
CO2-NH2-5-M
CO2-NH2-5-L
Ethane-NH2-5-S
Ethane-NH2-5-M
Ethane-NH2-5-L
0.001
0.01
0.1
2 3 4 5 6 7 8 9
Frequency (Hz)

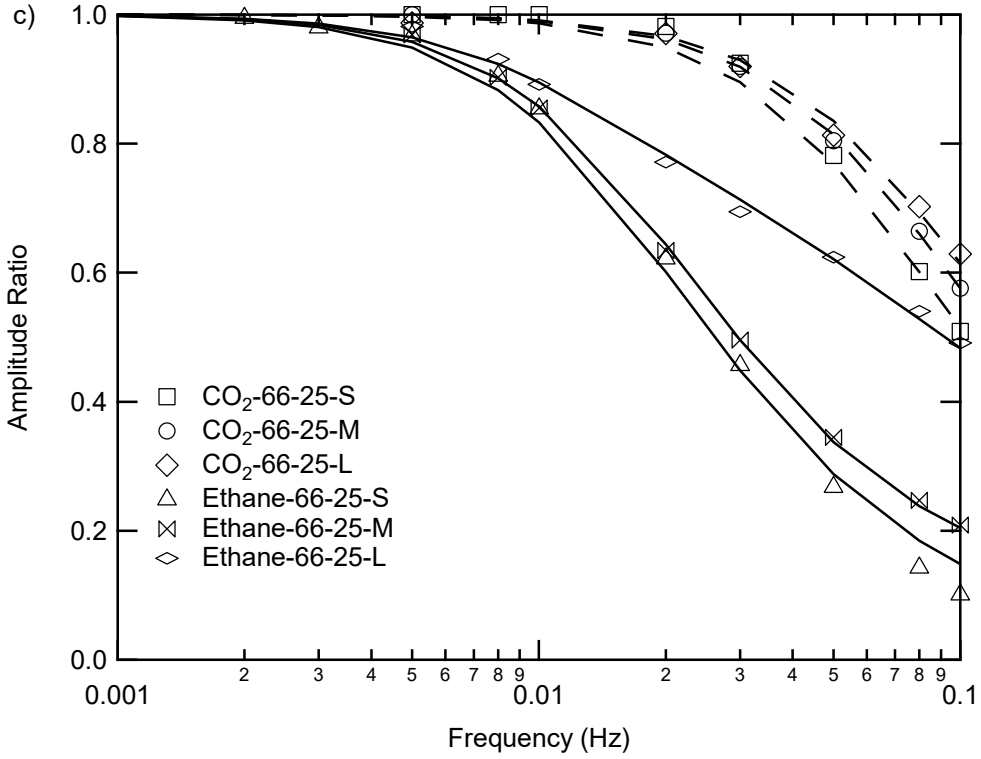
c)
1.0
0.8
0.6
0.4
0.2
0.0
Amplitude Ratio
CO2-66-25-S
CO2-66-25-M
CO2-66-25-L
Ethane-66-25-S
Ethane-66-25-M
Ethane-66-25-L
0.001
0.01
0.1
Frequency (Hz)

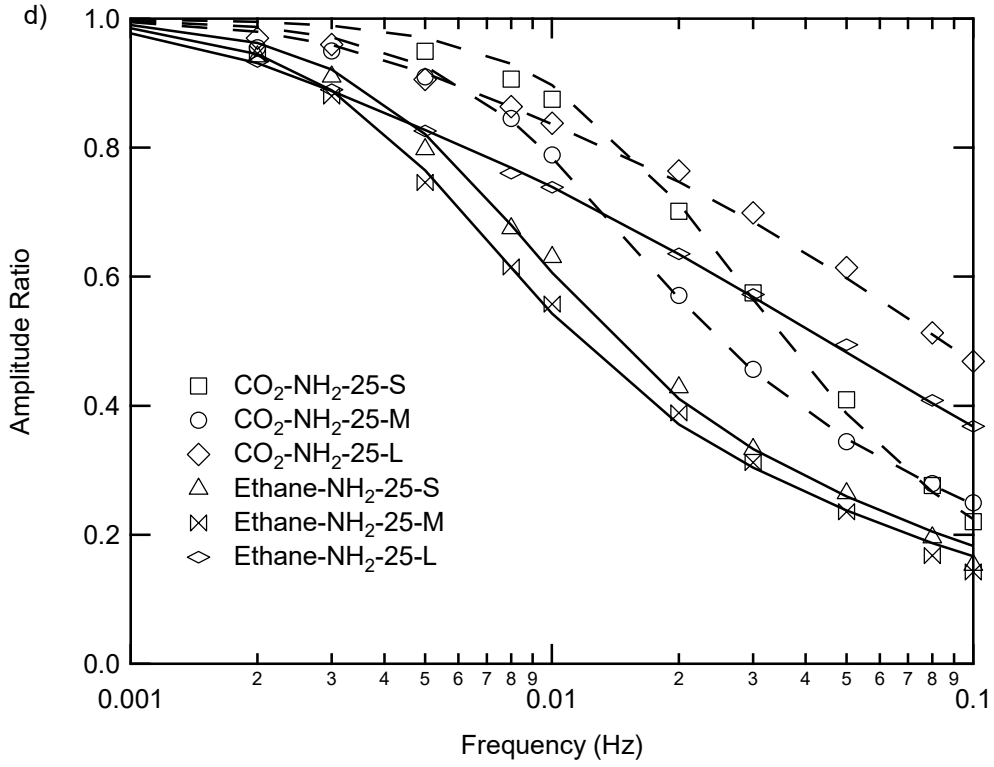
d)
Amplitude Ratio
1.0
0.8
0.6
0.4
0.2
0.0
0.001
0.01
0.1
2 3 4 5 6 7 8 9
2 3 4 5 6 7 8 9
Frequency (Hz)
CO2-NH2-25-S
CO2-NH2-25-M
CO2-NH2-25-L
Ethane-NH2-25-S
Ethane-NH2-25-M
Ethane-NH2-25-L

Table 4.2 Regressed isotherm slope parameter, *K'*, and mass transfer parameter, η, for ethane and CO_2 CSFR experiments on different size pellets of UiO-66 and UiO-66-NH_2 pressed at either 5,000 or 25,000 psi.

		K' (kg/m³)				*η (1/s)*			
Adsorbate	*Thickness*	*66 5K*	*66 25K*	*NH_2 5K*	*NH_2 25K*	*66 5K*	*66 25K*	*NH_2 5K*	*NH_2 25K*
Ethane	*S*	0.162	0.135	0.394	0.240	>0.03	>0.03	>0.03	0.0032
	M	0.152	0.108	0.375	0.245	>0.03	0.0108	0.0039	0.0017
	L	0.120	0.059	0.355	0.228	>0.03	0.0017	0.0019	0.00033
CO2	*S*	0.037	0.024	0.122	0.088	>0.03	>0.03	>0.03	0.0156
	M	0.037	0.017	0.132	0.110	>0.03	0.056	>0.03	0.0035
	L	0.022	0.016	0.113	0.103	>0.03	0.027	0.0055	0.00068

There are several trends in the both the isotherm slope parameter and the mass transfer parameter. For experiments on the same pellet sample but varying the adsorbate, the CSFR curves for ethane are shifted to much lower amplitude ratios compared to the CO_2 curves. This is reflected by a large increase in *K'* values, with *K'* defined in eq. 4-10. Another trend in the isotherm slope parameter is a large increase for UiO-66-NH_2 samples compared with UiO-66 when pressed at the same pressure. This indicates that the UiO-66-NH_2 samples adsorb significantly more ethane and CO_2 than UiO-66.

The last trend in the isotherm slope parameter is that *K'* decreases slightly for pellets of the same material but pressed at higher pressures. The micropore model has no way of reconciling the differences in *K'* between pellets pressed at different pressures since the actual isotherm slope is the same as the isotherm slope parameter. For the macropore model, Equation 4.10 shows that the actual isotherm slope is related to the isotherm slope parameter by a difference of the macroporosity divided by the pellet density. However, the macroporosity over the pellet density term is several orders of magnitude less than the regressed *K'*, essentially making the actual isotherm slope the same as the regressed isotherm slope parameter.

To validate the trends in the isotherm slope parameter, adsorption isotherms for CO_2 were

measured on the thickest pellets for each UiO analog at both pressures. Since this is an equilibrium experiment, mass transfer is not an issue and pellet thickness should not matter. Figure 4.2 shows the CO_2 isotherms at room temperature on both UiO-66 and UiO-66-NH_2 for both pellet pressures. The isotherms for the UiO-66-NH_2 give much higher capacities at each designated CO_2 pressure up to the measured range of 1 bar. The isotherms also show that capacities are slightly decreased for the samples pressed at 25,000 psi compared to the same material pressed at 5,000 psi. The trends in the adsorption isotherms show very good agreement with the regressed isotherm slopes from the CSFR experiments.

Table 4.2 also lists the regressed mass transfer parameter, η, which is defined in eq. 4-11. For several of the samples, including all of the thicknesses for UiO-66 pressed at 5,000 psi, the mass transfer through the pellet is too fast for the CSFR apparatus to measure accurately. This is demonstrated in Figure 4.3 using the ethane CSFR data for the thinnest and thickest UiO-66-NH_2 pellets pressed at 5,000 psi. For the thinner pellet, three fits are shown with the mass transfer parameter set at 0.003, 0.03, and 3 s^{-1}. The fit using 0.03 s^{-1} accurately describes the data; however, arbitrarily increasing the mass transfer parameter by two orders of magnitude gives the same fit in the frequency range of the data. When the mass transfer parameter is arbitrarily decreased, the fit significantly deviates from the data. This shows that at some point the model becomes insensitive to further increases in the mass transfer rate.

There are two ways to regain sensitivity of a frequency response system, either increase the diffusion length scale of the sample or increase the frequency range of the perturbations.[20] The thickest UiO-66-NH_2 pellet pressed at 5,000 psi is also shown in Figure 4.3 with 3 fits of 0.001, 0.0019, and 0.004 s^{-1}. The fit using 0.0019 s^{-1} accurately describes the data while fits using double and half that value show significant deviation, indicating that mass transfer is slow enough to

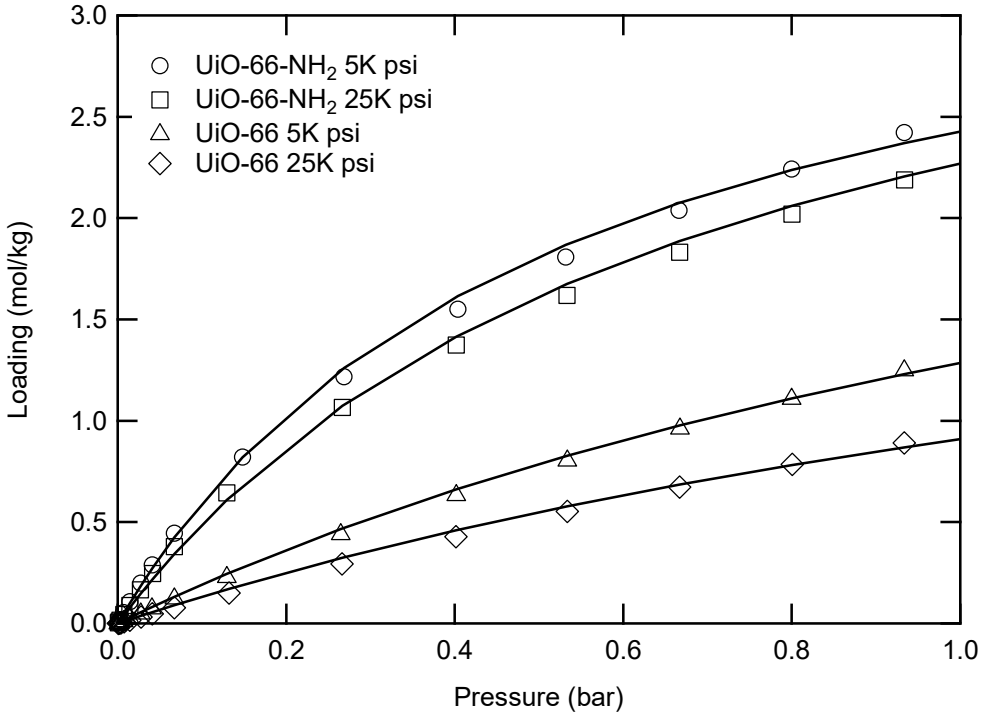

Figure 4.2 CO_2 isotherms on the thickest pellets of UiO-66 and UiO-66-NH_2 pressed at both 5,000 and 25,000 psi. Lines represent fits using a Langmuir isotherm model.

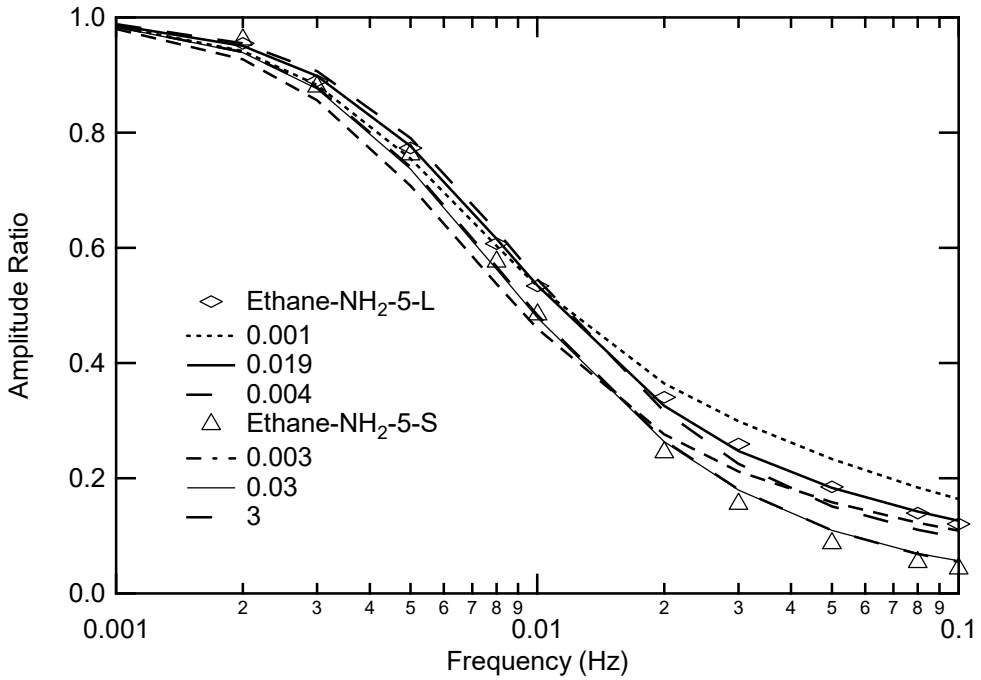

Figure 4.3 Amplitude ratio plots for ethane CSFR on the thinnest and thickest UiO-66-NH_2 pellets pressed at 5,000 psi and several fits showing the apparatus sensitivity.

measure accurately.

For the samples where the mass transfer parameter could be accurately measured, there are several trends. Ethane has lower η values than CO_2 for the same pellet samples, η decreases as pellet thickness increases, and η decreases for pellets of the same material pressed at higher pressure. The last two trends strongly point to macropore diffusion as the rate-limiting mass transfer mechanism. For micropore diffusion, the diffusion length scale is the radius of small crystallites in the pellet, and that length scale does not change as the pellet thickness increases. Therefore, the mass transfer parameter should be independent of the pellet thickness, which is not the case. Furthermore, pressing pellets at different pressures should only impact the macropores and not impact micropore diffusion. Again, this is opposite of the trends in the mass transfer parameter.

To confirm macropore diffusion as the rate-limiting mass transfer mechanism, the macropore diffusion coefficients were calculated from the η values using equation 4.11 and are listed in Table 4.3. The diffusion coefficients are approximately 3-5 times faster for pellets of UiO-66-NH_2 pressed at 5,000 psi compared to pellets pressed at 25,000 psi. The relation between the pellet macroporosity and diffusion coefficient clearly indicates macropore diffusion control. Further supporting macroporosity is that the diffusion coefficients are very similar for pellets of the same material pressed at the same pressure, regardless of pellet thickness. This trend encompasses both adsorbate molecules, which shows that different intermolecular interactions with the surface are not impacting diffusion. This makes sense as macropore diffusion is governed much more by collisions of gas molecules, similar to diffusion in the bulk fluid phase. To ensure that the diffusion of CO_2 and ethane in helium should be similar, low pressure binary gas-phase diffusion coefficients were predicted from Leonard-Jones potentials. The bulk diffusion

coefficients were 4.0 x 10^{-5} and 3.2 x 10^{-5} m^2/s for CO_2 and ethane, respectively; the similarity in the bulk diffusion coefficients agrees well with the similar macropore diffusion coefficients measured for CO_2 and ethane.

Table 4.3 Measured macropore diffusion coefficients.

		D_p x 10^6 (m^2/s)			
Adsorbate	*Thickness*	*UiO-66 5000 psi*	*UiO-66 25,000 psi*	*UiO-66-NH2 5,000 psi*	*UiO-66-NH2 25,000 psi*
Ethane	*S*	NA	NA	NA	0.3
	M	NA	2.2	1.6	0.7
	L	NA	0.5	1.6	0.3
CO2	*S*	NA	NA	NA	0.6
	M	NA	1.8	NA	0.6
	L	NA	2.4	1.5	0.3

4.4 Conclusions

Two analogs of a MOF, UiO-66, were pelletized at different pressures and thicknesses. The pellets were tested for mass transfer limitations of CO_2 and ethane using a CSFR apparatus. It was found that isotherm slopes and capacities were much higher for UiO-66-NH_2 compared to the unfunctionalized UiO-66 and that pressing the pellets at higher pressures had a slightly negative impact on capacity. Macropore diffusion was determined to be the rate-limiting mass transfer mechanism, and measured marcropore diffusion coefficients were greatly impacted by the pelletization pressure. Because the driving force for macropore diffusion is molecule collisions, similar to bulk diffusion, the macropore diffusion coefficients were essentially independent of the adsorbate and only impacted by the physical properties of the pellets.

References

1. Kim, J.; Chen, B.; Reinike, T. M.; Li, H.; Eddaoudi, M.; Moler, D. B.; O'Keeffe, M.; Yaghi, O. M. Assembly of Metal-Organic Frameworks from Large Organic and Inorganic Secondary Building Units: New Examples and Simplifying Principles for Complex Structures *J. Am. Chem. Soc.* **2001**, 123 (34), 8239-8247.
2. Furukawa, H.; Ko, N.; Go, Y. B.; Aratani, N.; Choi, S. B.; Choi, E.; Yazaydin, A. O.; Snurr, R. Q.; O'Keeffe, M.; Kim, J.; Yaghi, O. M. Ultrahigh porosity in metal-organic frameworks. *Science* **2010**, 329 (5990), 424-428.
3. M. Eddaoudi, J. Kim, N. Rosi, D. Vodak, J. Wachter, M. O'Keeffe, and O. M. Yaghi. Systematic design of pore size and functionality in isoreticular MOFs and their application in methane storage. *Science*, **2002**, 295, 469.
4. Wilmer, C. E.; Leaf, M.; Lee, C. Y.; Farha, O. K.; Hauser, B. G.; Hupp, J. T.; Snurr, R. Q. Large-scale screening of hypothetical metal-organic frameworks. *Nat. Chem.* **2012**, 4, 83-89.
5. P. Deria, J. E. Mondloch, E. Tylianakis, P. Ghosh, W. Bury, R. Q. Snurr, J. T. Hupp and O. K. Farha. Perfluoroalkane functionalization of NU-1000 via solvent-assisted ligand incorporation: synthesis and CO_2 adsorption studies. *J. Am. Chem. Soc.*, **2013**, 135, 16801.
6. M. Kim, J. F. Cahill, Y. Su, K. A. Prather and S. M. Cohen. Postsynthetic ligand exchange as a route to functionalization of inert metal-organic frameworks. *Chemical Science*, **2012**, 3, 126.
7. M. Kim, J. F. Cahill, H. Fei, K. A. Prather and S. M. Cohen. Postsynthetic ligand and cation exchange in robust metal-organic frameworks. *J. Am. Chem. Soc.*, **2012**, 134, 18082.
8. Burtch, N. C.; Jasuja, H.; Walton, K. S. Water Stability and Adsorption in Metal-Organic Frameworks. *Chem. Rev.* **2014**, 114, 10575-10612.

9. Cavka, J. H.; Jakobsen, S.; Olsbye, U.; Guillou, N.; Lamberti, C.; Bordiga, S.; Lillerud, K. P. A New Zirconium Inorganic Building Brick Forming Metal Organic Frameworks with Exceptional Stability. *J. Am. Chem. Soc*. **2008**, 130, 13850−13851.
10. DeCoste, J. B.; Peterson, G. W.; Schindler, B. J.; Killops, K. L.; Browe, M. A.; Mahle, J. J. The Effect of Water Adsorption on the Structure of the Carboxylate Containing Metal−Organic Frameworks Cu-BTC, Mg-MOF-74, and UiO-66. *J. Mater. Chem. A* **2013**, 1, 11922−11932.
11. DeCoste, J. B.; Peterson, G. W. Metal-Organic Frameworks for Air Purification of Toxic Chemicals. *Chem. Rev.* **2014**, 114, 5695-5727.
12. Jasuja, H.; Peterson, G. W.; DeCoste, J. B.; Browe, M. A.; Walton, K. S. Evaluation of MOFs for air purification and air quality control applications: Ammonia removal from air. *Chem. Eng. Sci.* **2015**, 124, 118-124.
13. Peterson, G. W.; DeCoste, J. B.; Fatollahi-Fard, F.; Britt, D. K. Engineering UiO-66-NH_2 for Toxic Gas Removal. *Ind. Eng. Chem. Res.* **2014**, 53, 701-707.
14. Karger, J.; Ruthven, D. M.; Theodorou, D. N. Diffusion in Nanoporous Materials. *Wiley-VCH*: Weinheim, **2012**.
15. Yasuda, Y. Determination of vapor diffusion coefficients in zeolite by the frequency response method. *J. Phys. Chem.* **1982**, 86, 1913-1917.
16. Liu, J.; Wang, Y.; Benin, A. I.; Jakubczak, P.; Willis, R. R.; LeVan, M. D. CO_2/H_2O Adsorption Equilibrium and Rates on Metal-Organic Frameworks: HKUST-1 and Ni/DOBDC. *Langmuir* **2010**, 26, 14301-14307.
17. Wang, Y.; LeVan, M. D. Master Curves for Mass Transfer in Bidisperse Adsorbents for Pressure-Swing and Volume-Swing Frequency Response Methods. *AIChE J.* **2011**, 57, 2054-2069.

18. Glover, T. G.; Wang, Y.; LeVan, M. D. Diffusion of Condensable Vapors in Single Adsorbent Particles Measured via Concentration-Swing Frequency Response. *Langmuir* **2008**, 24, 13406-13413.
19. Yang, Q.; Wiersum, A. D.; Llewellyn, P. L.; Guillerm, V.; Serre, C.; Maurin, G. Functionalizing porous zirconium terephthalate UiO-66(Zr) for natural gas upgrading: A computational exploration. *Chem. Commun.* **2011**, 47, 9603-9605.
20. Rees, L. V. C.; Song, L. Frequency Response Method for the Characterization of Microporous Solids in Recent Advances in Gas Separation by Microporous Ceramic Membranes (ed. N. K. Kanellopoulos), *Elsevier Science*: Amsterdam, **2000**, 139-186.

CHAPTER V

METAL-ORGANIC FRAMEWORKS FOR THE STORAGE OF OXYGEN

5.1 Introduction

Metal-organic frameworks (MOFs) have been of broad interest to the adsorption community for their wide variety of applications such as gas storage,[1] separations,[2] sensing,[3] catalysis,[4] and toxic gas removal.[5] However, to date there has been minimal focus on oxygen storage. The storage of oxygen has applications for use by first responders and military personnel, as well as in the medical and aerospace industries. In these applications there is a need to increase the amount of oxygen stored per unit volume at the same pressure or to reduce the oxygen storage pressure, due to safety concerns, while maintaining storage capacity.

This chapter outlines work that was a highly collaborative effort involving simulations and experiments. Simulations were performed at NuMat Technologies. Adsorbent materials were supplied by NuMat Technologies and the Edgewood Chemical Biological Center (ECBC). Experimental isotherms were measured at Vanderbilt with high pressure (140 bar) isotherms measured at NuMat Technologies due to safety concerns.

5.2 Experiments

5.2.1 Materials

All reagents were purchased from commercial sources and used without further purification unless otherwise noted. The activated carbon Norit SX ultra (Aldrich, 53663) was

purchased and used without any further modification. Zeolite NaX was supplied by UOP and used without any further modification.

HKUST-1 (Figure 5.1) was synthesized at NuMat by dissolving 1,3,5-benzene tricarboxylic acid (10.9 g, 51.8 mmol) and $Cu(NO_3)_2 \cdot 3H_2O$ (38.61 g, 166 mmol) in a mixture of ethanol (220 mL), H_2O (220 mL), and dimethyl formamide (DMF, 16 mL). This solution was heated at 80 °C for 20 h. HKUST-1 was isolated by filtration and washed with methanol (500 mL) which afforded 10.5 grams (67% yield based on BTC) after drying. Prior to sorption measurements, HKUST-1 was activated under high vacuum (10^{-3} Torr) at 150 °C.

First for NU-125 (Figure 5.2) the hexa-carboxylic acid linker was synthesized at NuMat as outlined by Wilmer et al.[6] and seen in Scheme 5.1. The hexa-carboxylic linker **5** (9.00 g, 11.66 mmol) and $Cu(NO_3)_2 \cdot 3H_2O$ (23.37 g, 96.7 mmol) were suspended in DMF (900 mL) in a 1000 mL pyrex screw-cap jar. After which, HBF_4 (18 mL, 0.138 mmol) was added and the pyrex jar was capped and heated in an oven at 80 °C for 14 h. The jar was cooled and the NU-125 crystals were isolated by filtration and suspended in acetone (200 mL). Every 4 h, the acetone was decanted and fresh acetone was added. This process was repeated 8 times. NU-125 was filtered affording 9.42 g (84% yield based on the linker) after drying. Prior to sorption measurements, NU-125 was treated under high vacuum (10^{-3} Torr) at 110 °C.

UiO-66 (Figure 5.3) was synthesized at ECBC by the procedure used by Peterson et al.[7] In short, benzene dicarboxylic acid (19.068 mmol), and $ZrCl_4$ (19.068 mmol) were dissolved in DMF (742 mL) in a glass beaker. The resulting mixture was divided equally into three 500 mL glass jars. The jars were placed in a preheated oven at 120 °C for 24 h. The solution was cooled to room temperature and the resulting solid was repeatedly washed with DMF. DMF was

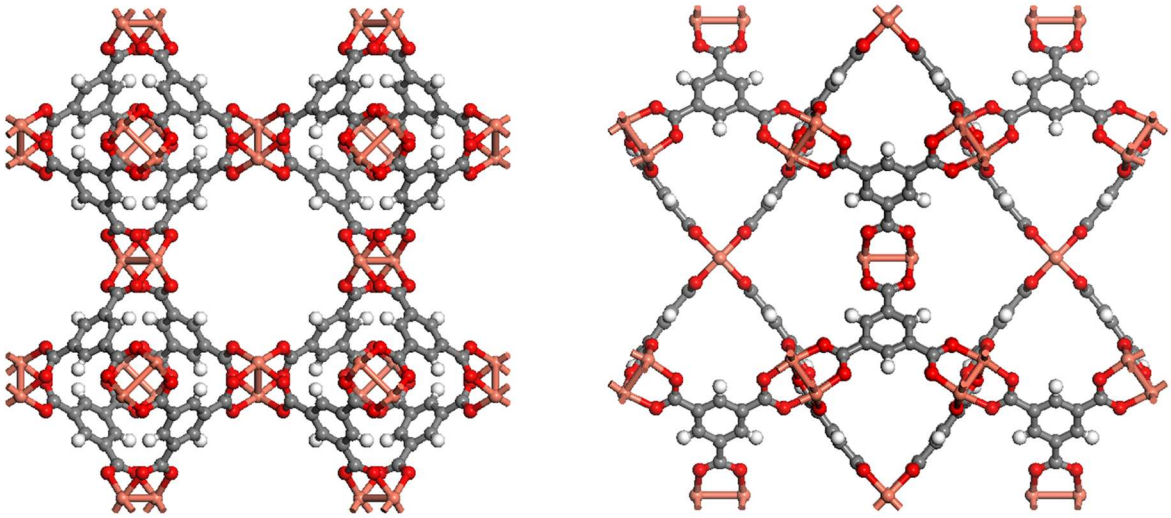

Figure 5.1 Structure of HKUST-1 viewed from two different axes to show the various pore structures. Carbon (gray), hydrogen (white), oxygen (red), and copper (brown) atoms can be seen.

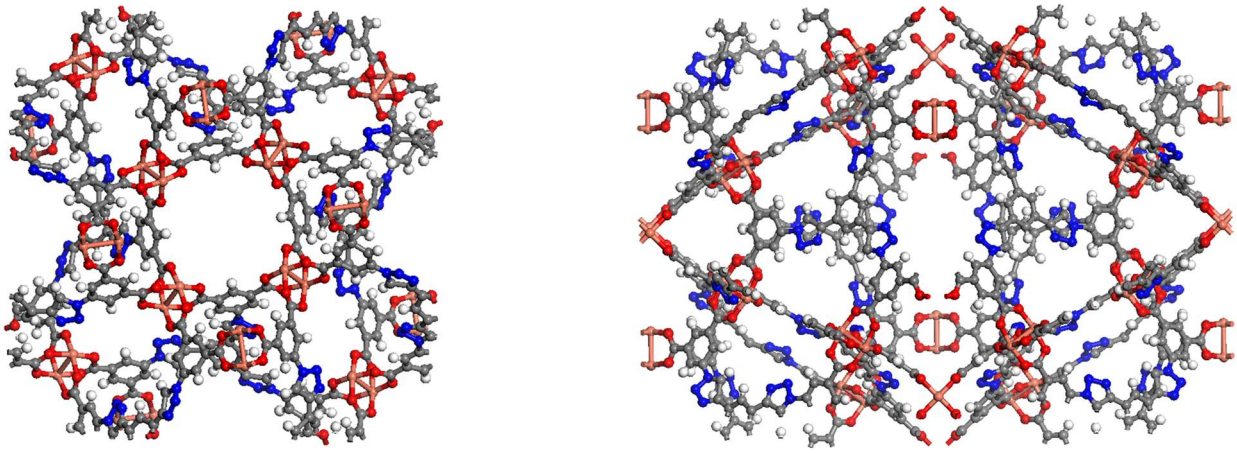

Figure 5.2 Structure of NU-125 viewed from two different axes to show the various pore structures. Carbon (gray), hydrogen (white), oxygen (red), copper (brown), and nitrogen (blue) atoms can be seen.

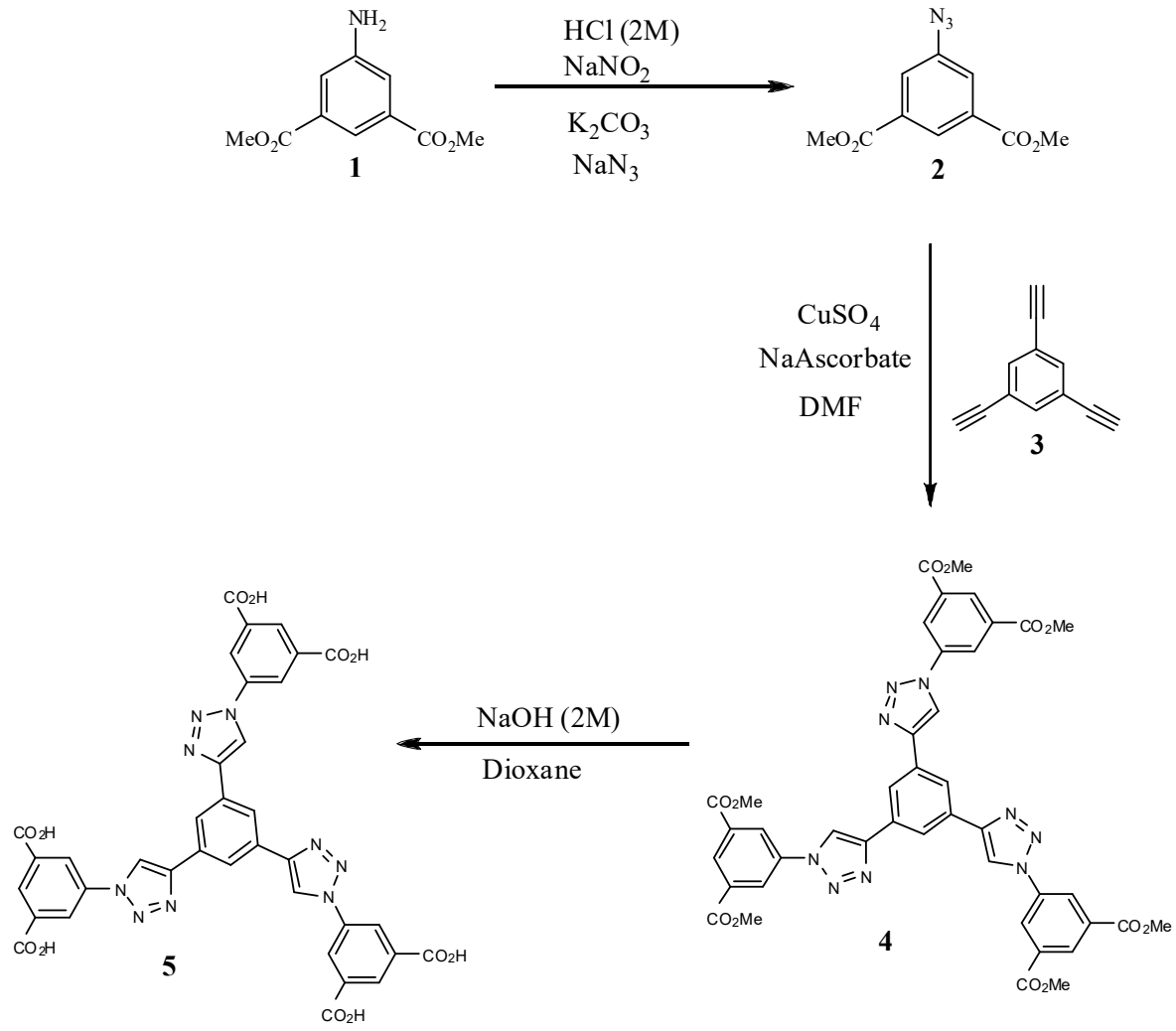

Scheme 5.1 Synthesis of the linker for NU-125.

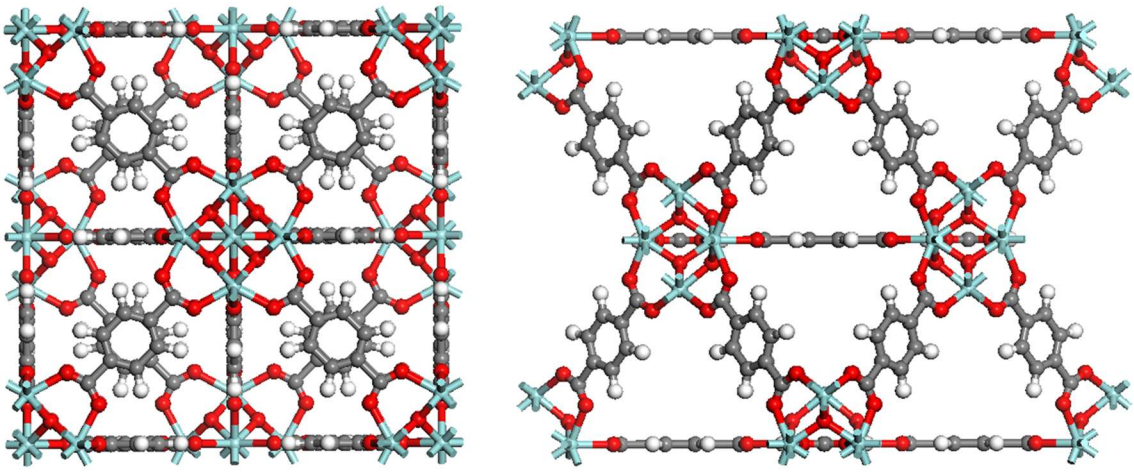

Figure 5.3 Structure of UiO-66 viewed from two different axes to show the various pore structures. Carbon (gray), hydrogen (white), oxygen (red), and zirconium (light blue), atoms can be seen.

subsequently exchanged with methanol and then activated under high vacuum (10^{-3} Torr) at 150 °C.

5.2.2 Oxygen Isotherms

A volumetric apparatus, described elsewhere,[8] was used to collect oxygen isotherms at 298, 313, and 348 K over the pressure range of 1 to 30 bar. Approximately 2 g of each sample was degassed using a Micromeritics ASAP 2020 porosimeter to provide an accurate sample weight and then loaded into the adsorption bed of the apparatus. Once loaded, the sample was degassed overnight in situ (423 K for HKUST-1, UiO-66, and N-AC; 383 K for NU-125). Research grade oxygen (99.9995%) was used to pressurize a buffer region inside the environmental chamber and allowed to equilibrate thermally. A pressure transducer with a range of 3000 psi was used to record the pressure. After equilibration of the buffer region, a pneumatic valve was opened to dose the adsorbent bed and the pressure was recorded after equilibration. Once equilibrated, the pneumatic valve was closed and the buffer region was dosed again. Excess loadings were calculated by material balance based on the pressure readings and the known volumes of the buffer region and bed void space.

The volumetric apparatus was also used to collect oxygen isotherms at 298 K after repeated adsorption/desorption cycles. Isotherms were collected before cycling and after cycles 5, 10, 20, and 50. For the first 10 cycles the sample was quickly charged to 30 bar and held for ~16 h, and vacuum was pulled for ~8 h at 298 K. For cycles 11 to 50, the samples were quickly charged to 30 bar and held for 15 min at 298 K. Before each isotherm was measured, the sample was degassed overnight at the appropriate temperature.

High pressure oxygen isotherms (up to 140 bar) were measured using a Micromeritics HPVA II-200 Volumetric Sorption Analyzer. Sample sizes between 500-750 mg were used in each

measurement.

5.3 Results and Discussion

Prior to performing experiments, a library of over 100,000 hypothetical MOF materials was simulated at NuMat for oxygen capacities in order to down select which MOFs to be studied experimentally. The database was created through the use of established high-speed MOF generation techniques and designed to maximize the breadth of material properties over a minimal set of frameworks.[9] Each material in the database was then run through a charging algorithm and a grand canonical Monte Carlo (GCMC) simulation, returning calculated room-temperature oxygen adsorbed quantities as a function of pressure, as depicted in Figure 5.4.[10,11] The most promising materials from this study were then curated, producing a final list of materials for experimental validation. From the information obtained in these simulations, it was determined that HKUST-1 and NU-125 were prime candidates to study further, based on their superior ability to adsorb oxygen and currently known synthesis techniques.

These MOFs, along with UiO-66, a zirconium based MOF known for its exceptional stability,[12] an activated carbon (Norit SX ultra, herein referred to as N-AC), and zeolite NaX were examined by measuring oxygen isotherms up to 30 bar at multiple temperatures at Vanderbilt and high pressure oxygen isotherms up to 140 bar at room temperature at NuMat. The 30 bar metric was chosen due to safety concerns with higher pressure oxygen at elevated temperatures (up to 348 K), while the 140 bar metric at ambient temperature was chosen based on the standard pressure used in medical oxygen tanks. N-AC was used as a baseline sorbent, as previous works have shown that activated carbons can provide high oxygen storage capacities.[13]

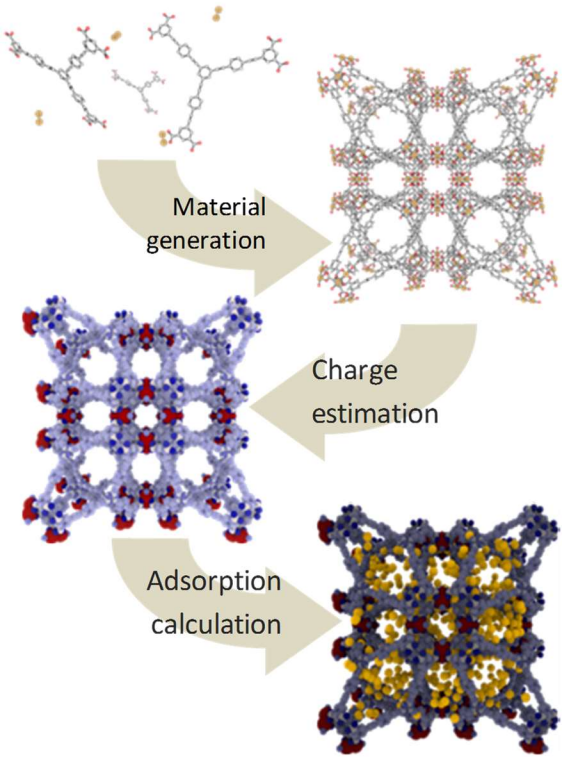

Figure 5.4 Schematic representation of how MOFs are generated and computationally screened for sorption characteristics.

Excess oxygen isotherms for HKUST-1, NU-125, and UiO-66 were measured for pressures up to approximately 30 bar at 298 K and are compared to N-AC and NaX in Figure 5.5. At pressures less than 5 bar, the inset shows that NU-125 and N-AC have similar O_2 capacities, while HKUST-1 has a slightly lower capacity. The isotherm for N-AC begins to curve slightly downward between 5 and 30 bar, while the HKUST-1 and NU-125 isotherms remain much more linear. At 30 bar NU-125, HKUST-1, and N-AC have excess O_2 capacities of 8.3, 6.0, and 5.0 $mol \cdot kg^{-1}$, respectively. In contrast, UiO-66 and NaX have significantly lower capacities of 3.5 and 2.0 $mol \cdot kg^{-1}$, respectively. Ideal materials exhibit oxygen isotherms characterized by low slopes at low pressures, indicating minimized sorbent-sorbate interactions at low pressures, and high overall capacities at high pressures, thereby maximizing working capacity.

The Toth equation can be used to describe the temperature and pressure dependence of adsorption over wide ranges.[14] At higher pressures, adsorption is not likely to form a monolayer assumed by a Langmuir model and the Toth equation allows an extra empirical parameter for fitting. The loading from the Toth isotherm is described as

$$n = \frac{n_s bP}{[1 + (bP)^t]^{(1/t)}} \tag{5.1}$$

where, n_s is the saturation loading, b describes the adsorption affinity, and t is a measure of the adsorbent heterogeneity. The temperature dependences of n_s, b, and t are given by

$$n_s = n_0 \exp\left[\chi\left(1 - \frac{T}{T_0}\right)\right] \tag{5.2}$$

$$b = b_0 \exp\left[\frac{Q}{RT_0}\left(\frac{T}{T_0} - 1\right)\right] \tag{5.3}$$

$$t = t_0 + \alpha\left(1 - \frac{T}{T_0}\right) \tag{5.4}$$

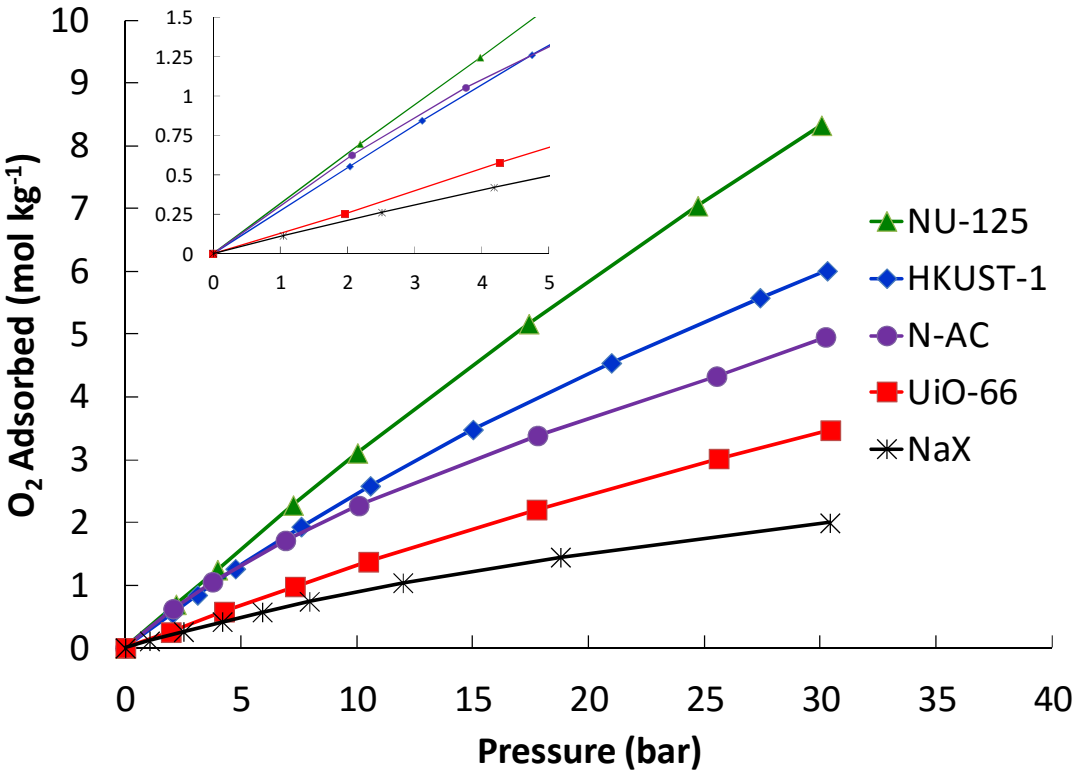

Figure 5.5 Excess oxygen isotherms measured at 298 K up to 30 bar.

where χ and α are empirical parameters, T_0 is a reference temperature, and Q is the isosteric heat of adsorption in the Henry's law limit. For the Toth isotherm, when the compressibility factor (z) is equal to 1, the isosteric heat of adsorption is given as[14]

$$\Delta H_{ads} = Q - \frac{\alpha R_0}{t}\left\{\ln(bP) - [1 + (bP)^t] ln\left[\frac{bP}{(1+(bP)^{1/t})}\right]\right\} \quad (5.5)$$

Due to it's monotonic form, the Toth equation cannot describe excess isotherm data that exhibit maxima. Therefore, the loading n used in equation 1 is the absolute loading given by

$$n = n_{ex} + \rho V_{ad} \quad (5.6)$$

where n_{ex} is the measured excess loading, ρ is the bulk gas density, and V_{ad} is the adsorbed phase volume, which is generally accepted as the micropore volume of an adsorbent.

Figure 5.6 shows excess oxygen isotherms measured at 298, 323, and 348 K for each MOF and N-AC. Using T_0 = 273.15 K as the reference temperature, the Toth parameters for oxygen were obtained via a least squares analysis and are given in Table 5.1. From these data, and the oxygen isotherms of NaX reported elsewhere,[8] the isosteric heat of adsorption of oxygen as a function of loading was calculated for each material at 298 K using eqn 5.5. The results are displayed graphically in Figure 5.7.

Table 5.1 Model parameters for multi-temperature Toth equation.

Material	n_s *(mol kg^{-1})*	b_0 *(bar^{-1})*	$Q/(RT_0)$	t_0	α	χ	ΔH_{ads} *(kJ mol^{-1})*
HKUST-1	28.6	0.0153	4.90	0.834	0.0154	0.0190	9.7
UIO-66	20.0	0.00951	3.67	0.984	0.0583	0.0210	8.3
NU-125	37.0	0.0134	3.91	0.982	0.0668	0.0262	6.9
NU-AC	19.3	0.0290	5.42	0.614	0.450	0	10.0
NaX	4.08	0.0533	3.59	1	0	1.77	14.0

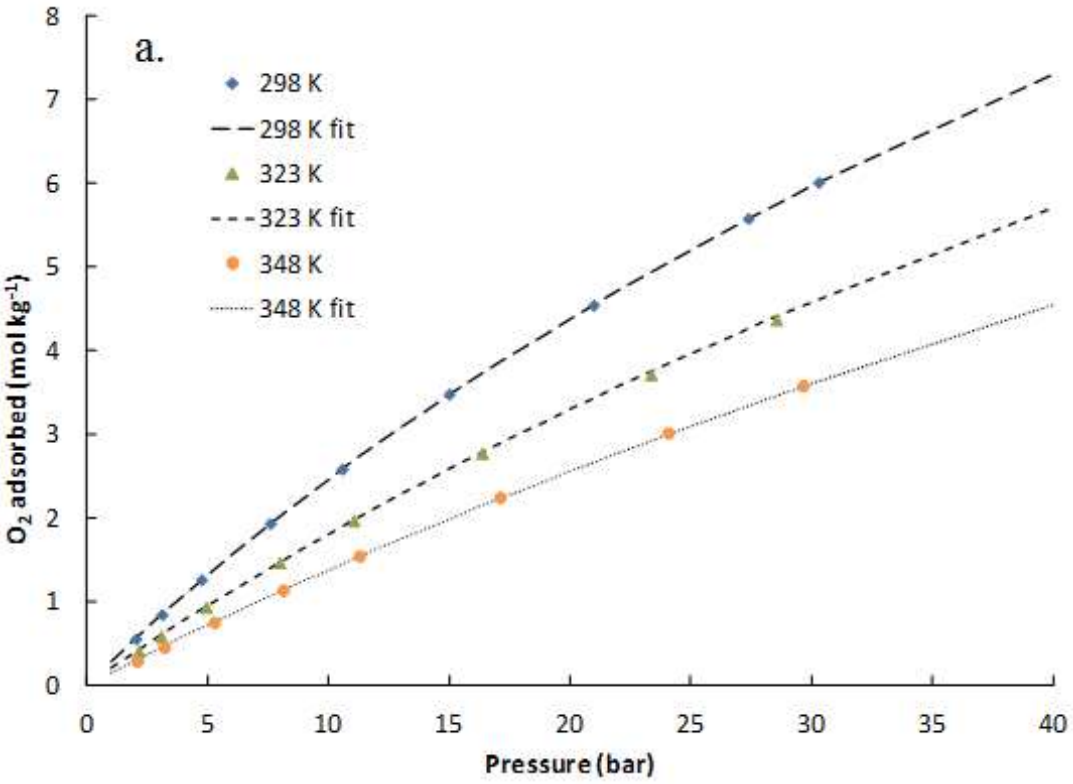

Figure 5.6 Excess oxygen adsorption isotherms of a. HKUST-1, b. NU-125, c. UiO-66, and d. N-AC taken at 298, 323, and 348 K and fit to the Toth model.

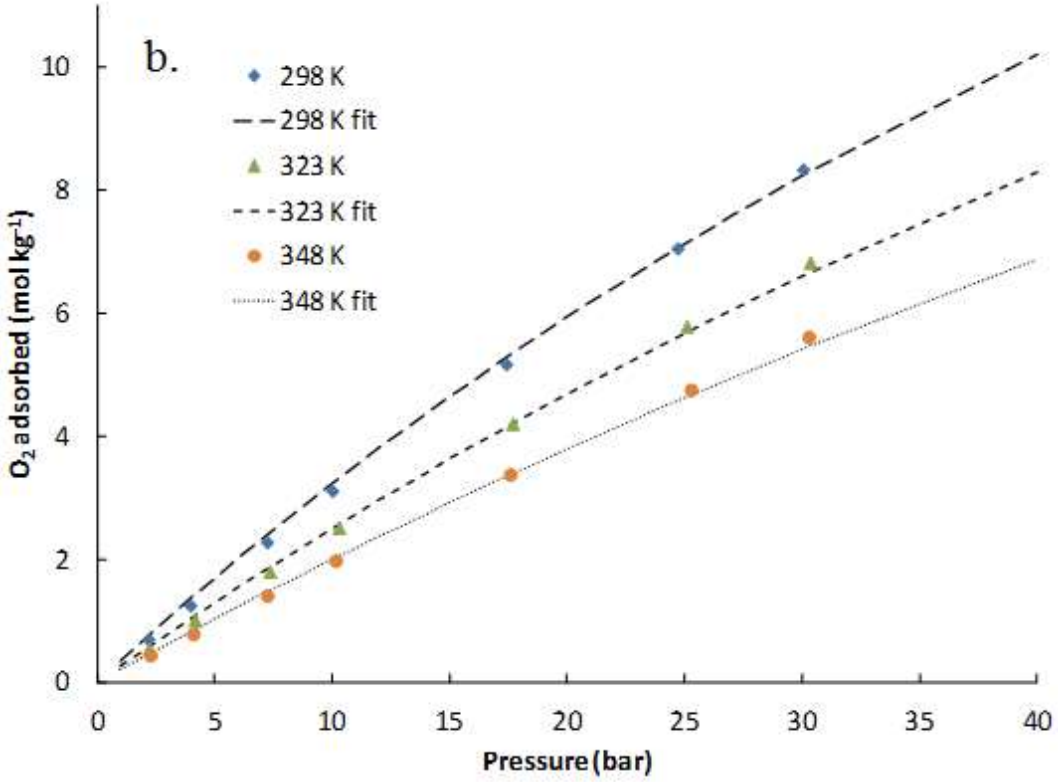
b.
298 K
298 K fit
323 K
323 K fit
348 K
348 K fit
O_2 adsorbed (mol kg^{-1})
Pressure (bar)
0
2
4
6
8
10
0
5
10
15
20
25
30
35
40

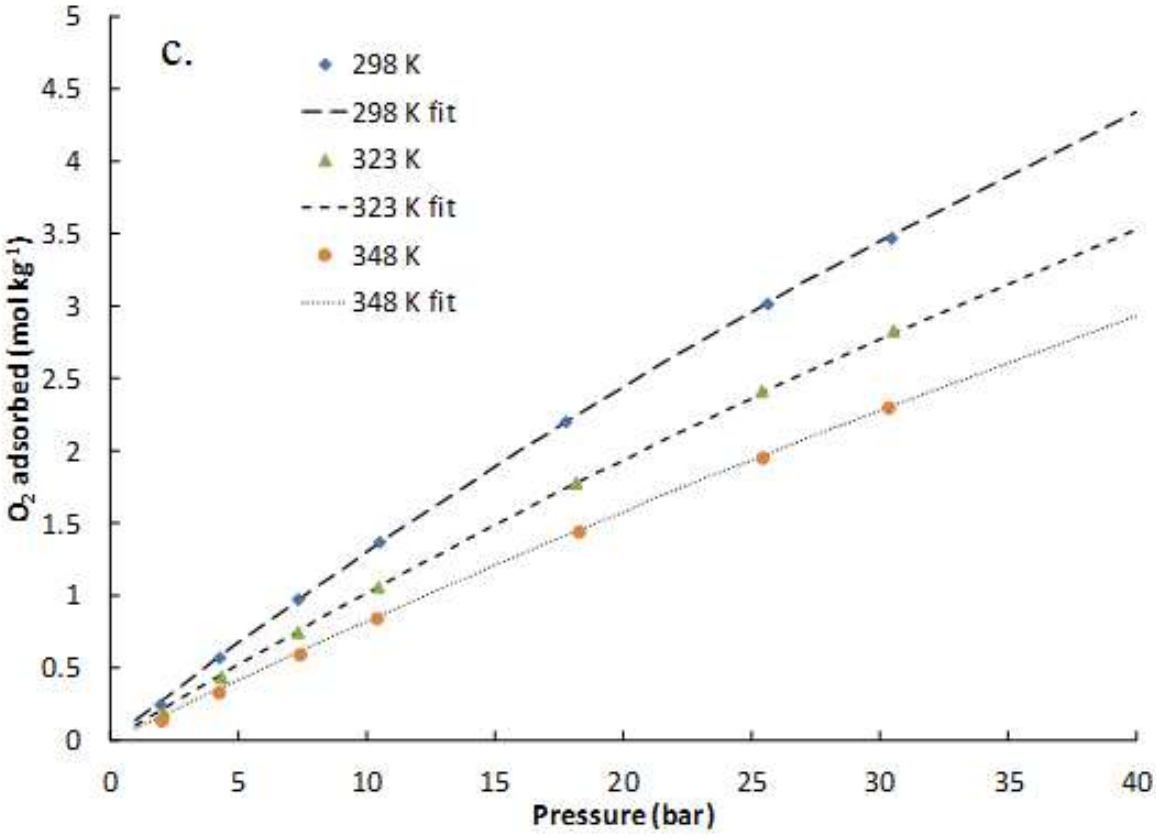
C.
298 K
298 K fit
323 K
323 K fit
348 K
348 K fit
O2 adsorbed (mol kg-1)
Pressure (bar)
0
0.5
1
1.5
2
2.5
3
3.5
4
4.5
5
0
5
10
15
20
25
30
35
40

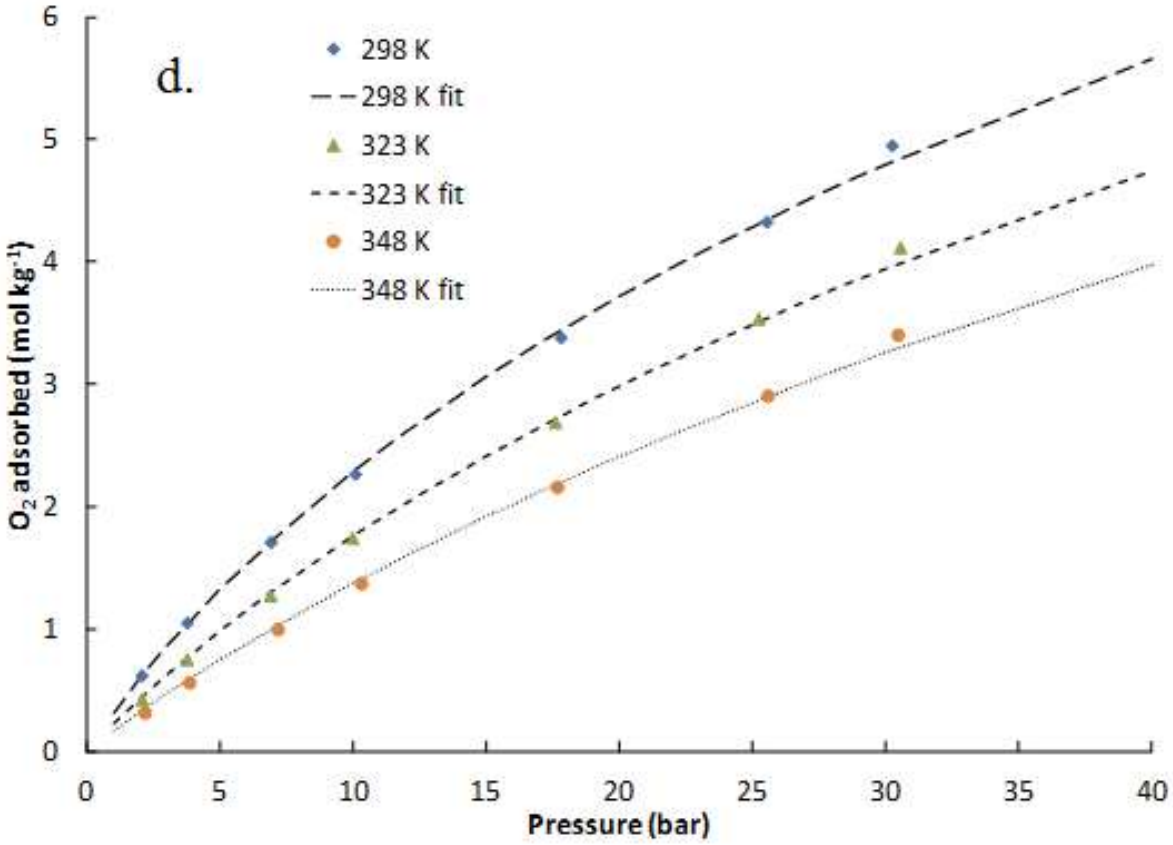
d.
298 K
298 K fit
323 K
323 K fit
348 K
348 K fit
O_2 adsorbed (mol kg^{-1})
Pressure (bar)
0
1
2
3
4
5
6
0
5
10
15
20
25
30
35
40

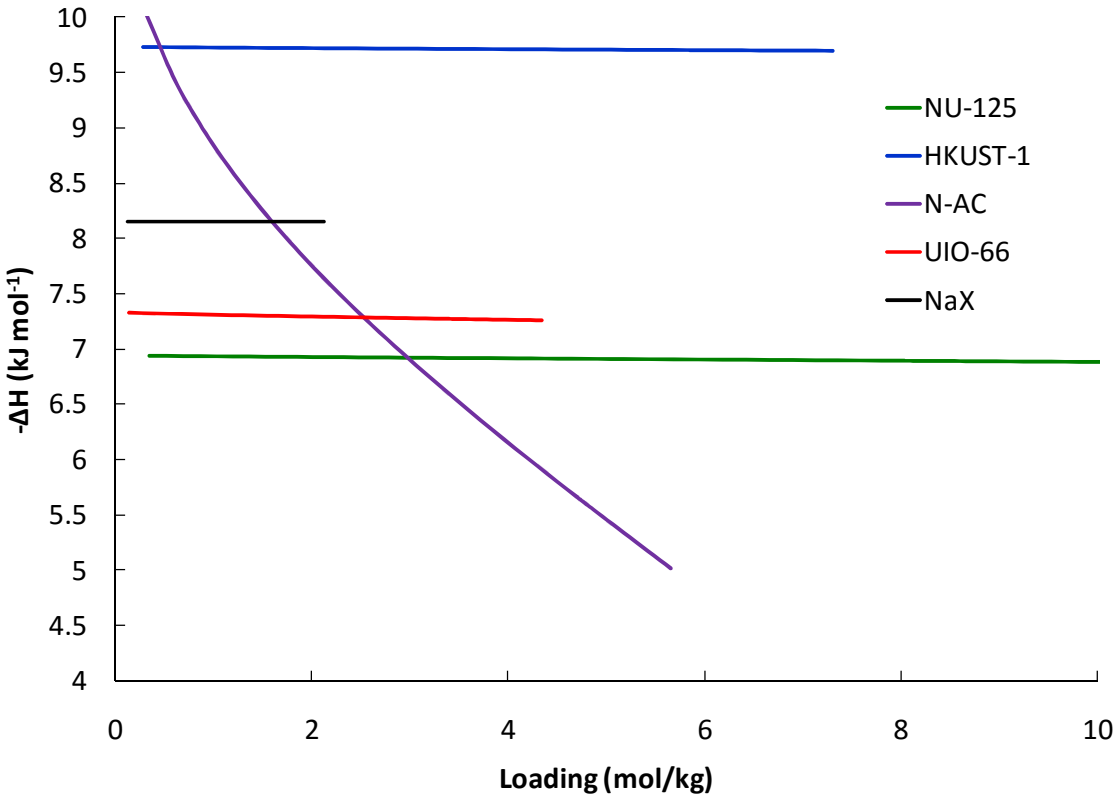

Figure 5.7 Isosteric heat of adsorption for oxygen as a function of loading at 298 K.

This work focuses on the adsorption of oxygen only at high pressures; therefore, data were not obtained below 1 bar. It was observed that the isosteric heat of adsorption for N-AC decreases as a function of increased loading at 298 K, indicative of adsorption that contains adsorbate-adsorbent interactions with a heterogeneous material. On the other hand, HKUST-1, NU-125, and NaX show a relatively unchanged isosteric heat of adsorption with increased loading at 298 K, indicative of adsorption dominated mainly by geometric phenomena on a homogeneous surface. Having a high capacity while minimizing the strong interactions of the material with adsorbate is important. These interactions typically dominate at pressures below the working pressure of gas cylinders, which in turn ultimately would not desorb from the material to be delivered to the desired destination.

Both HKUST-1 and NU-125 contain coordinatively unsaturated copper sites; however, these sites do not seem to preferentially adsorb oxygen at the high pressures studied here. The adsorption of oxygen was observed to be geometric in the GCMC calculations and oxygen did not cluster at the Cu sites. However, it has been shown that coordinatively unsaturated metal sites can enhance the adsorption of oxygen at low pressures.[15] Furthermore, the isosteric heat of adsorption for HKUST-1 is higher than for NU-125, likely due to the smaller pore size and therefore a higher concentration of Cu sites in HKUST-1.

Based on the isotherms studied up to 30 bar, we decided to investigate HKUST-1, NU-125, and N-AC further. These materials were studied up to pressures of 140 bar at room temperature and compared to NaX from Wang et al.,[8] with the absolute oxygen isotherms shown in Figure 5.8. Figure 5.9 shows that the isotherm for each material compares well to the predicted outcome from the Toth model and the oxygen isotherm predicted from the GCMC calculations (HKUST-1 and NU-125 only). NU-125 and HKUST-1 have excess capacities of 98% and 75% greater than that

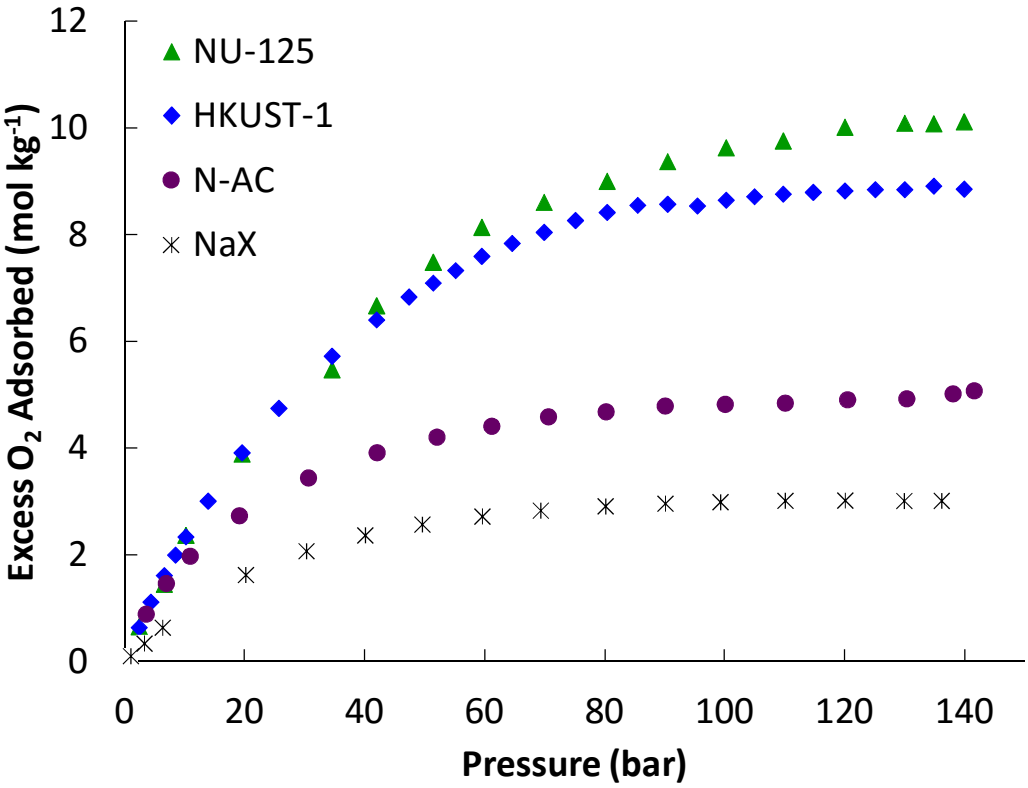

Figure 5.8 Excess oxygen adsorption isotherms measured at NuMat at room temperature up to 140 bar.

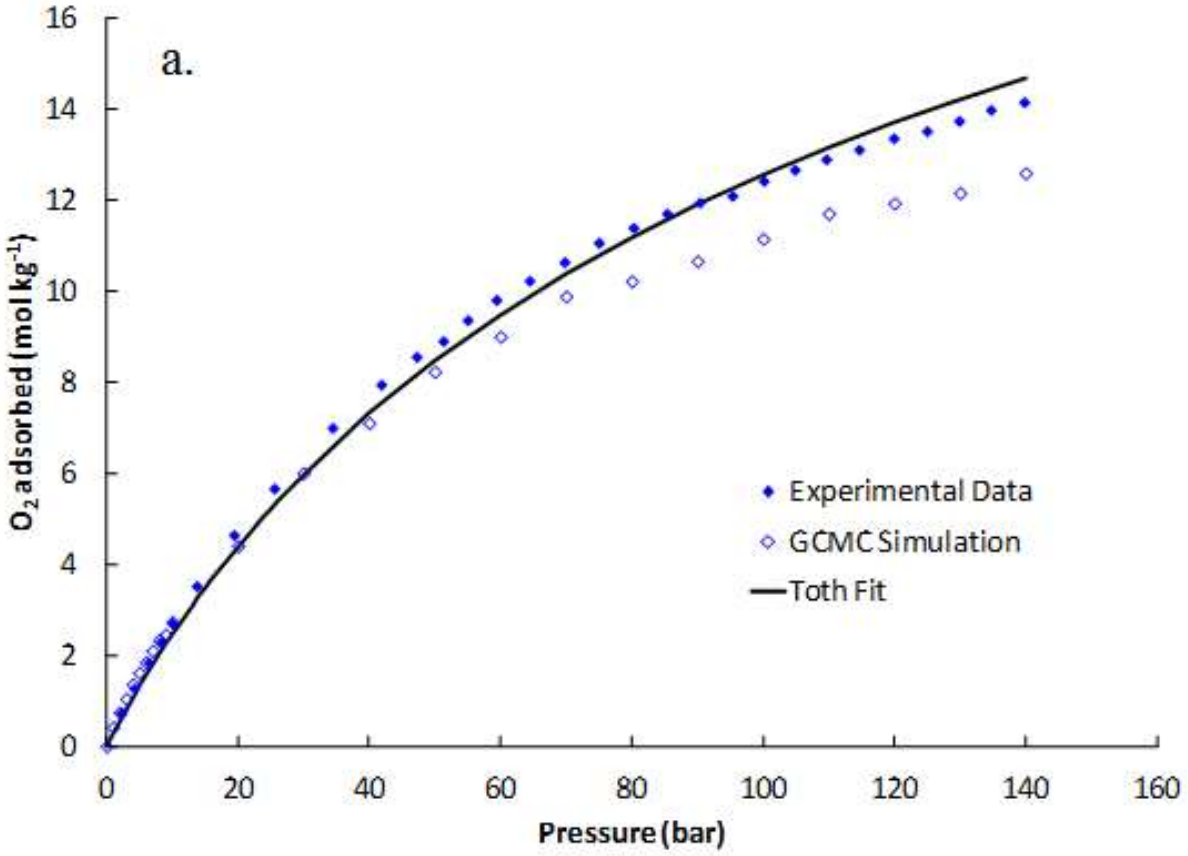

Figure 5.9 Absolute oxygen adsorption isotherms up to 140 bar at room temperature fit to the Toth model at 298K and compared to the simulated oxygen isotherm at 298K for a. HKUST-1, b. NU-125, c. N-AC, and d. NaX. Isotherms and simulations were performed at NuMat; Toth fit is based on multi-temperature isotherms measured at Vanderbilt.

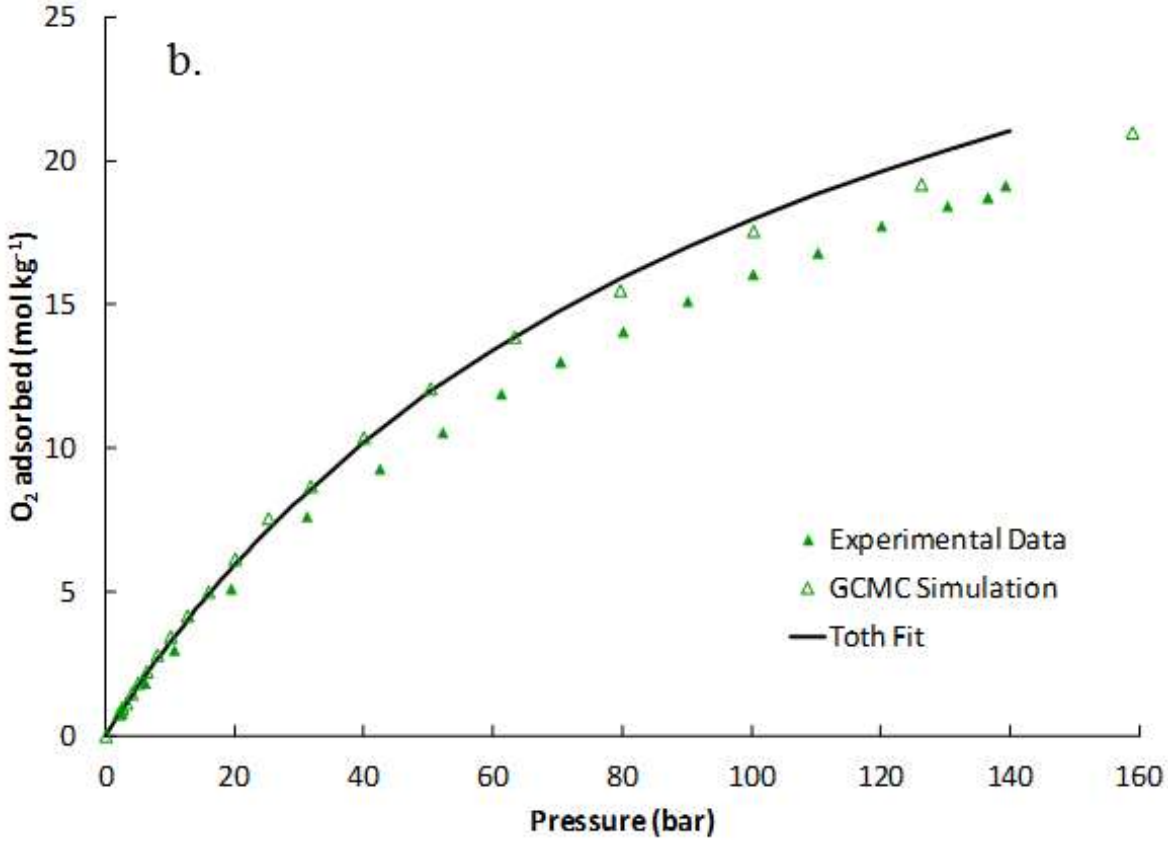
b.
25
20
15
10
5
0
O_2 adsorbed (mol kg^{-1})
0
20
40
60
80
100
120
140
160
Pressure (bar)
Experimental Data
GCMC Simulation
Toth Fit

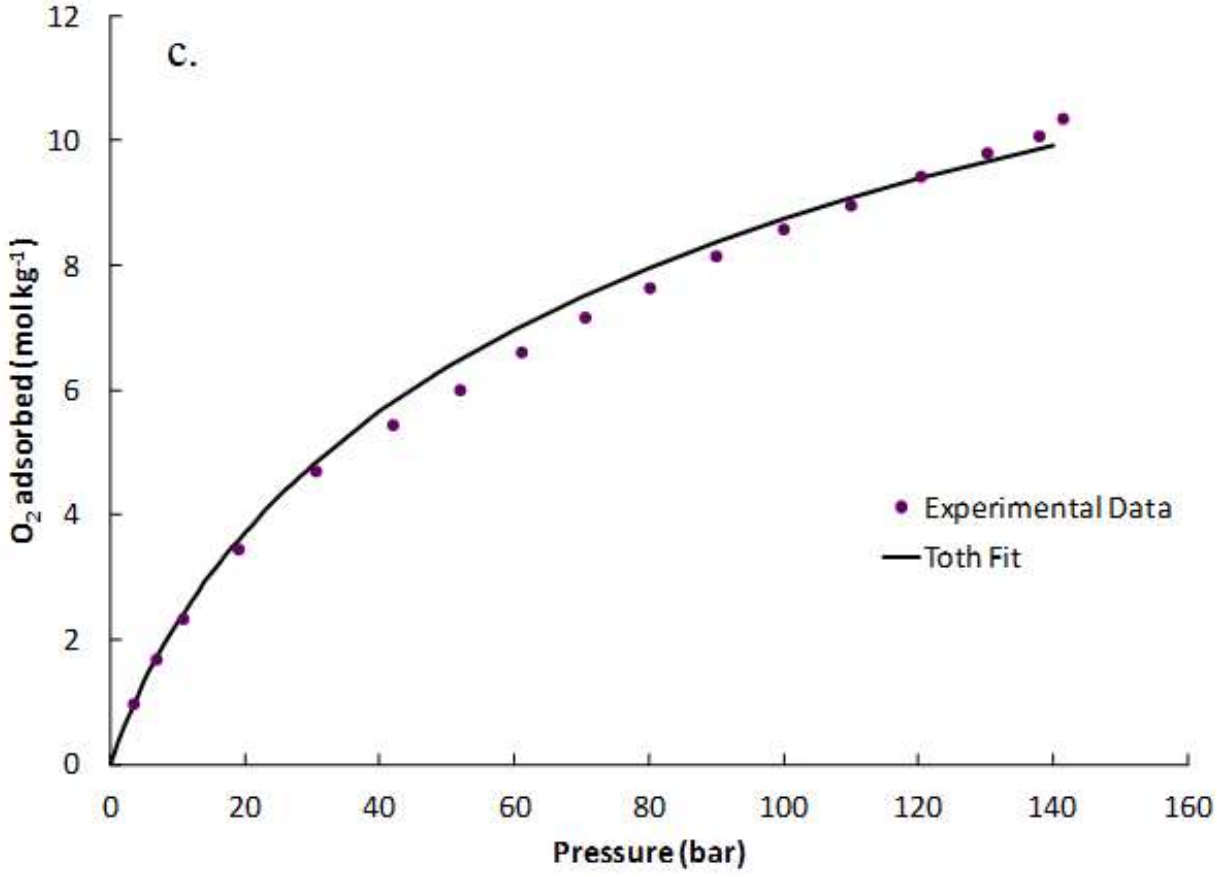
C.
12
10
8
6
4
2
0
0
20
40
60
80
100
120
140
160
O_2 adsorbed (mol kg^{-1})
Pressure (bar)
Experimental Data
Toth Fit

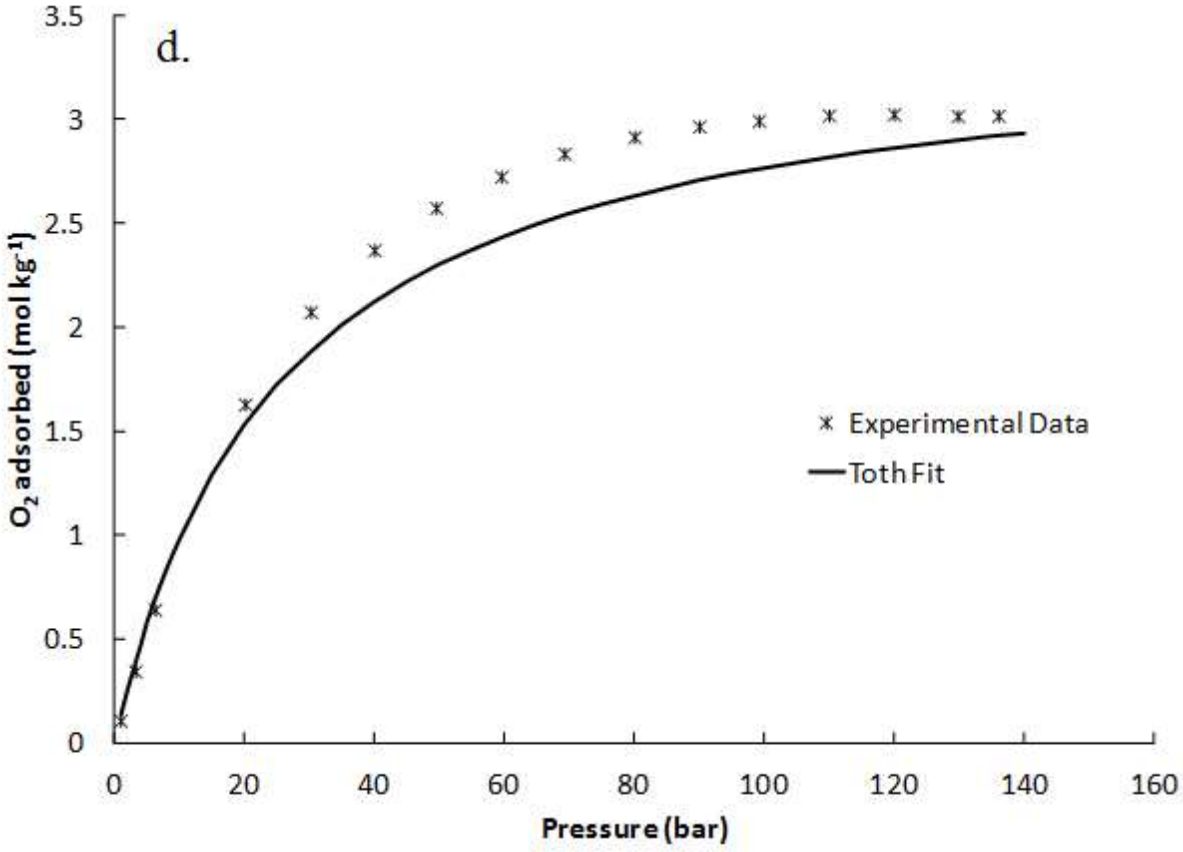
d.
3.5
3
2.5
2
1.5
1
0.5
0
O_2 adsorbed (mol kg^{-1})
0
20
40
60
80
100
120
140
160
Pressure (bar)
Experimental Data
Toth Fit

of the N-AC at 140 bar, respectively. Based on volumetric parameters, HKUST-1 and NU-125 have dramative increases over traditional empty oxygen cylingers pressurized to 140 bar.

NU-125 has the highest oxygen capacity reported in the literature. When compared to other adsorbents in the literature, NU-125 is comparable to the state of the art materials.[8,13,16] To date the best performing sorbents are primarily activated carbons, which are heterogeneous in nature. Shirasagi MSC-3R Type 172 carbon molecular sieve and AX-21 superactivated carbon exhibit similar excess oxygen adsorption capacities to one another of approximately 10 mol kg^{-1} at 100 bar.[13,16] It is important to note here that the MSC-3R and the AX-21 carbons have significantly different BET surface areas of approximately 750 and 3000 m^2 g^{-1}, respectively, showing that even though surface area can play a major role in the capacity of the material, it is certainly not the only factor. Other carbons, such as Takeda 3A CMS and BPL have been shown to have much lower capacities than MSC-3R and AX-21.[13,17]

For HKUST-1 and NU-125 adsorption and desorption cycles were performed to determine the structural integrity of the MOFs upon exposure to high pressure oxygen. It can be seen in Figure 5.10 that for each of the MOFs there is no appreciable loss in capacity over 50 cycles run up to 30 bar, and it can therefore be concluded that the structural integrity is maintained in the presence of oxygen at the pressures studied. This is important feature when considering recharging cycles.

5.4 Conclusions

The high capacities and ability to be cycled without a loss in capacity make HKUST-1 and NU-125 ideal potential adsorbents for oxygen storage. These MOFs are comparable to the current state of the art carbons and outperform zeolites for oxygen storage. A substantial increase in

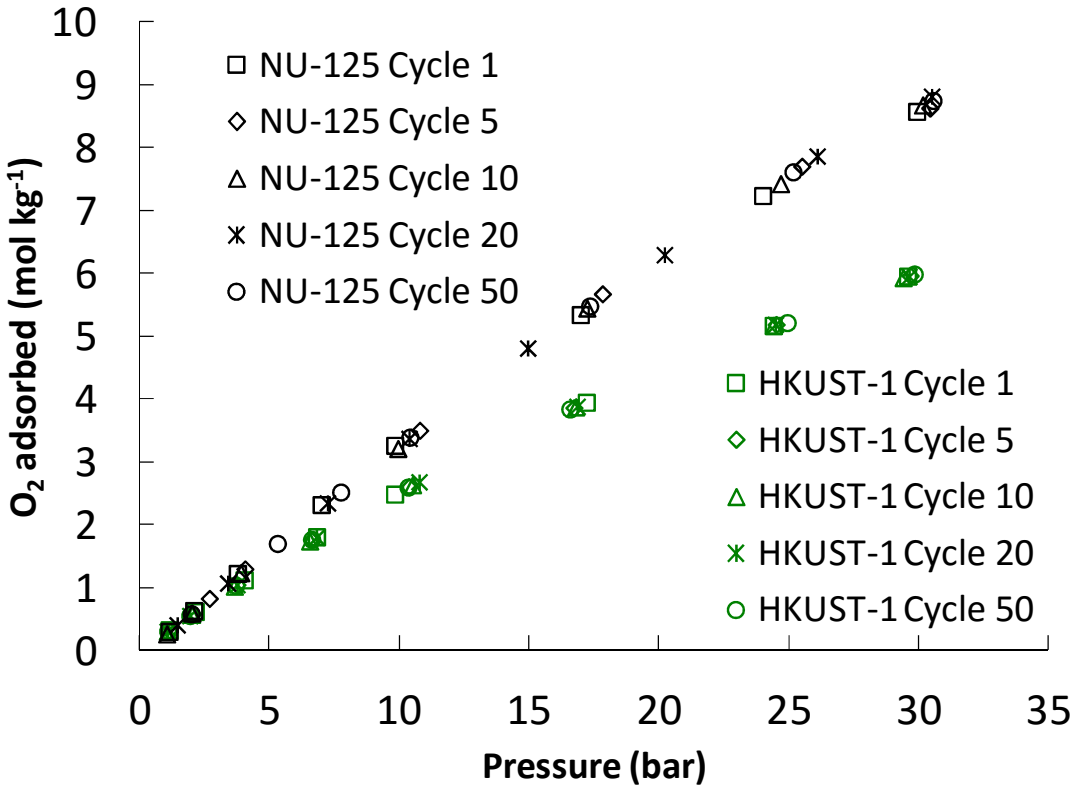

Figure 5.10 Excess oxygen adsorption isotherms measured over 50 adsorption and desorption cycles at 298 K and pressures up to 30 bar for HKUST-1 and NU-125.

capacity allows for a cylinder at high pressure to store much more oxygen, therefore requiring less frequent recharging, ultimately reducing the cost of oxygen storage, or even allow for smaller cylinders for easier transport. NU-125 has shown an increase in capacity at 140 bar of approximately 130% over an empty cylinder. These MOFs could also allow for one to obtain a similar capacity to an empty cylinder at a decreased pressure, which could allow for the use of less heavy-duty cylinder components, ultimately reducing the cost or total mass of the oxygen storage device. Ultimately increased capacities in oxygen cylinders can lead to longer dives for divers, more efficient storage for fighter pilots and astronauts, and a better quality of life for those who are dependent on medical oxygen.

References

1. Getman, R. B.; Bae, Y.-S.; Wilmer, C. E.; Snurr, R. Q. Review and Analysis of Molecular Simulations of Methane, Hydrogen, and Acetylene Storage in Metal-Organic Frameworks. *Chem. Rev.* **2012**, 112, 703-723.

2. Li, J.-R.; Kuppler, R. J.; Zhou, H.-C. Selective gas adsorption and separation in metal-organic frameworks. *Chem. Soc. Rev.* **2009**, 38, 1477-1504.

3. Kreno, L. E.; Leong, K. F. O. K.; Allendorf, M.; Van Duyne, R. P.; Hupp, J. T. Metal-Organic Framework Materials as Chemical Sensors. *Chem. Rev.* **2012**, 112, 1105-1125.

4. Corma, A.; Garcia, H.; Xamena, L. I. Engineering Metal Organic Frameworks for Heterogeneous Catalysis. *Chem. Rev.* **2010**, 110, 4606-4655.

5. DeCoste, J. B.; Peterson, G. W. Metal-organic frameworks for air purification of toxic chemicals. *Chem. Rev.* **2014**, 114, 5695-5727.

6. Wilmer, C. E.; Farha, O. K.; Yildirim, T.; Eryazici, I.; Krungleviciute, V.; Sarjeant, A. A.; Snurr, R. Q.; Hupp, J. T. Gram-scale, high-yield synthesis of a robust metal-organic framework for storing methane and other gases. *Energ. Environ. Sci.* **2013**, *6*, 1158-1163.

7. Peterson, G. W.; DeCoste, J. B.; Glover, T. G.; Huang, Y.; Jasuja, H.; Walton, K. S. Effects of palletization pressure on the physical and chemical properties of the metal-organic frameworks $Cu_3(BTC)_2$ and UiO-66. *Micropor. Mesopor. Mat.* **2013**, *179*, 48-53.

8. Wang, Y.; Helvensteijn, B.; Nizamidin, N.; Erion, A. M.; Steiner, L. A.; Mulloth, L. M.; Luna, B.; LeVan, M. D. High pressure excess isotherms for adsorption of oxygen and nitrogen in zeolites. *Langmuir* **2011**, 27, 10648-10656.

9. Wilmer, C. E.; Leaf, M.; Lee, C. Y.; Farha, O. K.; Hauser, B. G.; Hupp, J. T.; Snurr, R. Q. Large-scale screening of hypothetical metal-organic frameworks. *Nat. Chem.* **2012**, *4*, 83-89.

10. Duren, T.; Bae, Y.-S.; Snurr, R. Q. Using molecular simulation to characterise metal-organic frameworks for adsorption applications. *Chem. Soc. Rev.* **2009**, *38*, 1237-1247.
11. Wilmer, C. E.; Kim, K. C.; Snurr, R. Q. An extended charge equilibration method. *J. Phys. Chem. Lett.* **2012**, *3*, 2506-2511.
12. Cavka, J. H.; Jakobsen, S.; Olsbye, U.; Guillou, N.; Lamberti, C.; Bordiga, S.; Lillerud, K. P. A new Zirconium inorganic builing brick forming metal organic frameworks with exceptional stability. *J. Am. Chem. Soc.* **2008**, *130*, 13850-13851.
13. Mitchell, L. A.; Tovar, T. M.; LeVan, M. D. High pressure excess isotherms for adsorption of oxygen and argon in a carbon molecular sieve. *Carbon* **2014**, *74*, 120-126.
14. Do, D. D. *Adsorption Analysis: Equilibria and Kinetics*, Imperial College Press, London, **1998**.
15. Murray, L. J.; Dinca, M.; Yano, J.; Chavan, S.; Bordiga, S.; Brown, C. M.; Long, J. R. Highly-selective and reversible O_2 binding in Cr_3(1, 3, 5-benzenetricarboxylate)$_2$. *J. Am. Chem. Soc.* **2010**, *132*, 7856-7857.
16. Zhou, Y.; Wei, L.; Yang, J.; Sun, Y.; Zhou, L. Adsorption of oxygen on superactivated carbon. *J. Chem. Eng. Data* **2005**, *50*, 1068-1072.
17. Bae, Y.-S.; Lee, C. H. Sorption kinetics of eight gases on a carbon molecular sieve at elevated pressure. *Carbon* **2005**, *43*, 95-107.

CHAPTER VI

SUPPORTED LITHIUM HYDROXIDE FOR CARBON DIOXIDE ADSORPTION

6.1 Introduction

Although rare, accidental releases of toxic industrial chemicals (TICs) pose great risks to civilian populations and emergency first responders. Many TICs can be dispersed in the air and require air purifying gas masks for responders working in the vicinity of an accident. Traditional gas masks use impregnated activated carbon (IAC) adsorbents to filter toxic compounds out of the air that the user breathes.[1] This type of mask is severely limited by the efficiency of the adsorbent. TICs represent a broad spectrum of chemical compounds with various functional groups. Often times the specific threat is unknown and to guarantee protection from these compounds requires adsorbents capable of performing a wide range of chemistry. This often limits the IAC's capacity for any one specific chemical, thereby reducing the effective lifetime of the mask.

A way around the need for these adsorbents is to use stored oxygen rather than filter the surrounding air. However, scuba-type apparatuses where a user inhales oxygen from a tank and exhales to the surrounding environment are highly oxygen inefficient. This leads to very heavy equipment that is unsuitable for extended periods of use. A way to increase oxygen efficiency is through a rebreather apparatus that recycles the user's exhaled oxygen in a completely closed loop system. Figure 6.1 shows a schematic of a tactical rebreather (TACR) with the required breathing specifications. For typical human respiration from the atmosphere, approximately 20% oxygen is inhaled, a small fraction is converted to carbon dioxide, and then exhaled. Due to the CO_2 that is exhaled and must be removed from the closed loop to prevent build up to toxic levels, the TACR

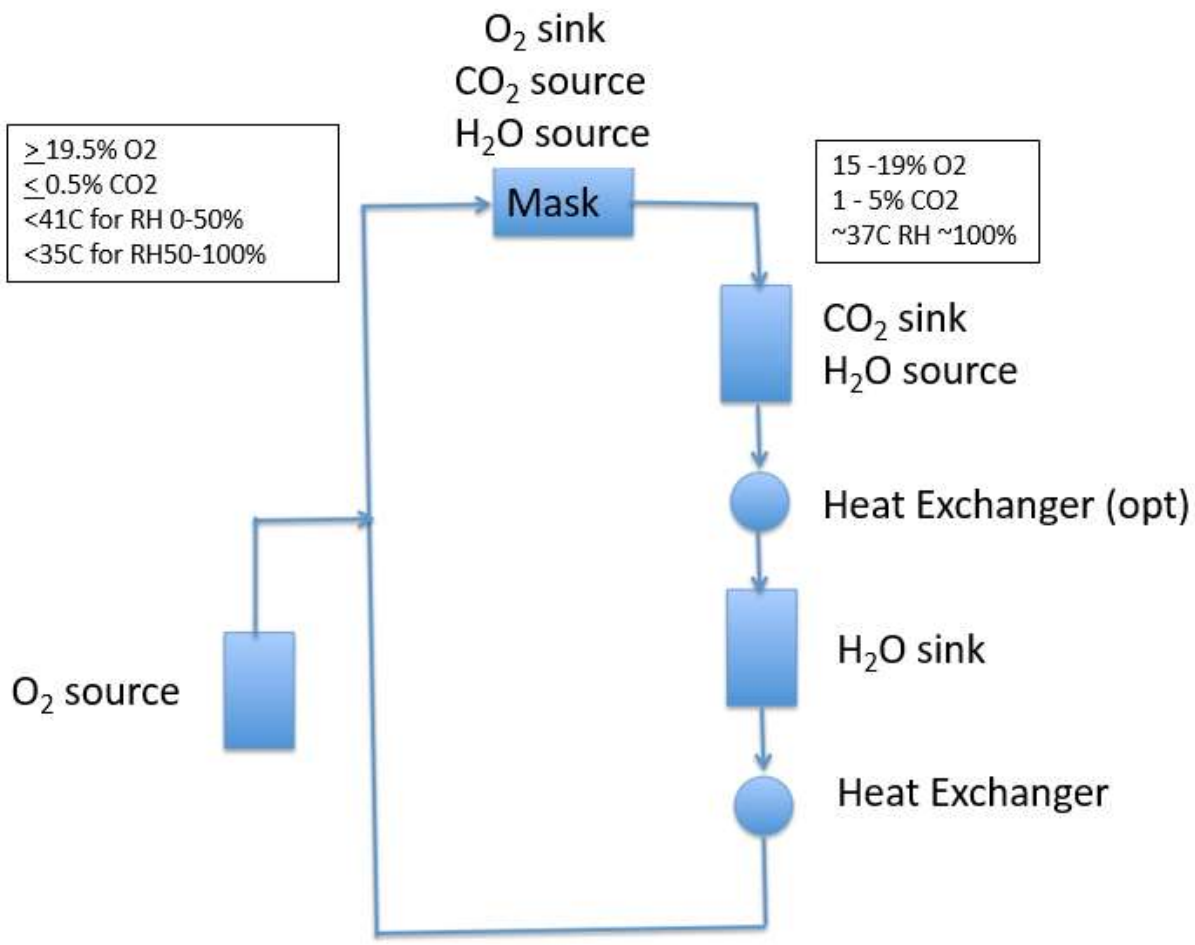

Figure 6.1 Schematic and breathing specifications for a tactical rebreather.

requires a CO_2 scrubbing mechanism. For a personal unit, the best way to remove CO_2 is with adsorbents.

Because CO_2 is the only compound that needs to be removed, an adsorbent can be specifically tailored for CO_2 capture to provide high capacity. However, there are several challenges in producing a CO_2 adsorbent for a TACR unit. The biggest need is a high CO_2 capacity despite low CO_2 partial pressures of less than 0.05 bar. Another requirement is that the unit must operate near room temperature. Lastly, the exhaled air will be saturated with water vapor, so the adsorbent must maintain CO_2 capacity in the presence of significant water concentrations.

There are many high surface area adsorbents such as zeolites[2-4] or MOFs[5-7] with large CO_2 capacities, but the physisorptive nature of these materials needs high CO_2 pressures to achieve the highest capacities. These adsorbents can also be hindered by coadsorption of water or stability issues.[8,9] Adsorbents based on chemisorption of CO_2 can have high capacities even at low concentrations. Solid-amines have been shown to have good capacities for direct CO_2 capture from ambient air;[10] however, these adsorbents typically have slow uptake rates that may not work in a TACR unit. Many metal oxides containing alkali or alkaline earth metals have been studied for CO_2 absorption to form carbonates at elevated temperatures.[11,12] At room temperature the uptake rates are extremely slow and unsuitable for TACR use.

LiOH was used for many years by NASA as a CO_2 adsorbent in life support systems of spaceships.[13] It offers permanent capture by conversion to lithium carbonate as given by

$$2LiOH + CO_2 \rightarrow Li_2CO_3 + H_2O \tag{6.1}$$

which gives a very high theoretical capacity of 20.8 moles CO_2 per kilogram LiOH based on stoichiometry.[14] The presence of water has been shown to facilitate this reaction by conversion to a lithium hydroxide monohydrate intermediate before reaction with CO_2.[15] However, water

saturated environments have a detrimental effect on CO_2 adsorption by LiOH pellets with reported efficiencies of 12% and 16% of theoretical capacity.[14,15] This is due to excess water dissolving the LiOH pellets, thereby losing porosity and creating Li_2CO_3 diffusion barriers for CO_2 to reach fresh LiOH. Similar diffusion barriers have been seen in lithium silicates.[16]

In this work, novel CO_2 adsorbents were developed for potential use in a TACR or similar conditions. Due to its light weight, LiOH still represents the best option for obtaining high capacities. Recently, Cho et al.[17] pressed mixed matrix pellets of LiOH and zeolite 13X and 5A. Their reported CO_2 capacities were high but still showed significant decrease under 100% humidity. To prevent the diffusion barriers that limit the efficiency of LiOH pellets under water saturated conditions, adsorbents were synthesized by depositing LiOH into the pores of carbon supports.

6.2 Experiments

6.2.1 Materials

The activated carbons Norit SX Ultra (lot 8031-4), Norit SX1G (lot 8005.5), Norit GSX (lot 8001.5), and Norit RX 1.5 Extra (lot 3519544) were provided by Cabot. BPL activated carbon (lot 4814-J) was supplied by Calgon Carbon Corp. MCM-41 was synthesized following the procedure from Janus et al.[18] LiOH powder was used as received from Sigma Aldrich. Research grade helium and 1% carbon dioxide in balance helium were purchased from Air Liquide.

6.2.2 Synthesis

LiOH was deposited onto multiple supports using a wet impregnation method. First, a 3 M aqueous solution of LiOH was prepared. Approximately 200 mg of the desired support was degassed at 100 °C for at least 1 hour to obtain water free weight. A micropipette was used to

dropwise add the LiOH solution to the support in a small glass vial. The amount of solution added would create a sample of nominal 10 wt% LiOH/support based on mass balance of the reagents. The mixture was then dried in a vacuum oven at 80 °C for 1 hour. The sample was allowed to cool and then more LiOH solution was dropwise added. This process was repeated until the desired amount of LiOH was deposited and then samples were dried overnight under vacuum at 80 °C. Samples of nominally 10, 20, 30, 40, and 50 wt% LiOH were synthesized.

6.2.3 Experiments

Surface area and pore volume were calculated from nitrogen isotherms collected using a Micromeritics ASAP 2020. X-ray diffraction spectra were measured using a Scintag X1h/h automated powder diffractometer. Elemental analysis of actual lithium content was measured by Galbraith Laboratories using ICP-AES.

Adsorption capacities were measured using a breakthrough apparatus depicted by Figure 6.2. Four inlet streams were controlled by MKS mass flow controllers. Two of the streams were pure helium with one of those streams flowing through a water sparger to become saturated with water vapor. The helium streams are mixed with the ratio of the two streams determining the relative humidity. A similar setup was used for streams that contained 1% CO_2 in helium. The pure helium and 1% CO_2 streams flow through a Cheminert two-position switching valve that controls which stream is feed to an adsorbent bed. Pressure in the adsorbent bed was controlled with an MKS Baratron type 640 pressure controller. Effluent from the adsorbent bed was sampled by an Agilent 5975 mass spectrometer.

To perform an experiment, approximately 50 mg of adsorbent was degassed at 100 °C to obtain accurate sample weight and then loaded into the adsorbent bed. The He stream at the desired relative humidity was used to condition the sample for 1 hour. At time zero, the switching valve

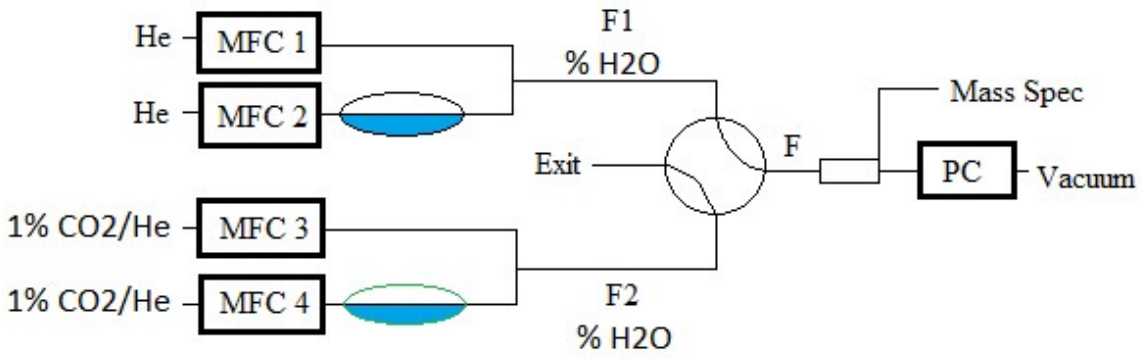

Figure 6.2 Breakthrough apparatus for testing CO_2 capacities under humid conditions.

was used to initiate flow of the 1% CO_2 stream at the same relative humidity that the sample was conditioned at. Adsorption capacities were calculated by integrating the concentration profile from the initial start time until the mass spectrometer signal plateaus. Unless otherwise noted, the experimental flow rate of the 1% CO_2 stream was 3 sccm.

6.3 Results and Discussion

The first support tested was the mesoporous silica MCM-41. There have been many studies on impregnated MCM-41 materials,[19-21] and the large uniform pores were expected to be ideal for the deposition of LiOH. The measured CO_2 capacities for LiOH supported on MCM-41 were much lower than expected. Table 6.1 shows the surface area and porosity measurements for MCM-41 and LiOH/MCM-41 at 10 and 20 wt% LiOH. Upon supporting the LiOH on MCM-41, both surface area and porosity are reduced to negligible amounts. Two possible reasons for this result could be the complete blockage of pores by unevenly deposited LiOH or the loss of pore structure during the synthesis. Figure 6.3 shows the XRD pattern for the samples. As can be seen by the lack of a significant diffraction pattern, the deposition of the highly basic LiOH solution causes a complete collapse of the silica pore structure. XRD of the zeolite mixed matrix pellets of Cho et al.[17] also showed the destruction of the zeolite pore structure. To prevent the issue of pore collapse, porous carbons that can withstand the basicity of the LiOH solution were tested.

Table 6.1 N_2 isotherm results for LiOH supported on MCM-41.

Sample	*Surface area* (m^2/g)	*Pore volume* (cm^3/g)
MCM-41	913.4	1.08
10 wt% LiOH	18.1	0.05
20 wt% LiOH	0.6	0.006

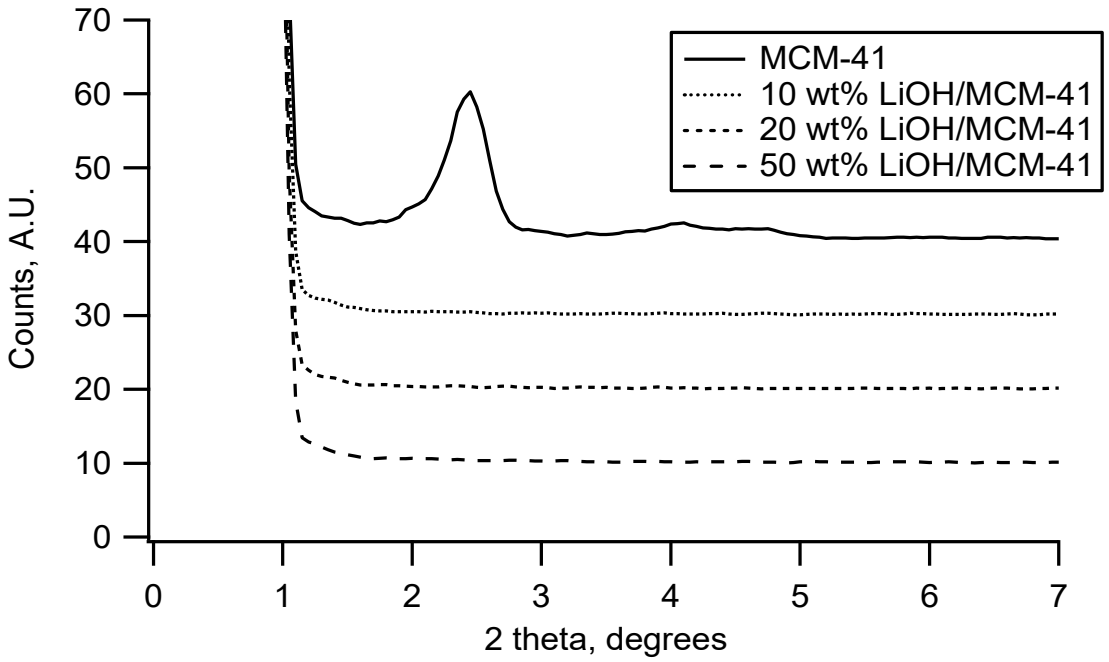

Figure 6.3 XRD patterns for MCM-41 and LiOH supported on MCM-41.

BPL activated carbon is a widely used bituminous coal-based adsorbent that is predominantly microporous. Table 6.2 shows CO_2 capacities and pore volumes for LiOH supported on BPL activated carbon. For the 10 wt% sample of LiOH on BPL, the CO_2 capacity increases over the plain support but not as high as expected for the amount of LiOH incorporated. For higher wt% LiOH samples, the measured CO_2 capacity actually decreases, which is opposite of what is expected. The nitrogen isotherms show significant decrease in the surface area and pore volume of the samples with higher LiOH content. This indicates a blockage of pores which likely results in a high amount of LiOH that is unavailable to react with CO_2. Furthermore, significant amounts of white precipitate on the synthesis glassware for the higher wt% LiOH samples indicate that much of the LiOH was not being incorporated into the samples. To try and resolve these issues, activated carbons with much higher pore volumes were tested.

Table 6.2 CO_2 breakthrough capacities and N_2 isotherm results for LiOH supported on BPL activated carbon.

LiOH content (wt%)	*BET SA (m^2/g)*	*Pore V (cm^3/g)*	*CO_2 capacity (mol/kg)*
0	939	0.550	0.07
10	860	0.476	0.35
20	658	0.368	0.25
50	505	0.298	0.28

A series of activated carbons were acquired to test as supports for LiOH. The activated carbons were Norit RX 1.5 Extra, Norit SX Ultra, Norit GSX, and Norit SX1G. In addition to having higher total pore volume than BPL activated carbon, the Norit carbons have different pore morphologies with varying degrees of microporosity and mesoporosity. Table 6.3 gives surface areas, total pore volume, percent of pore volume that is microporous for each carbon, and CO_2 capacity for 50 wt% LiOH supported. The two carbons with the worst CO_2 capacity when supporting LiOH are BPL and RX 1.5 extra which represent the lowest and highest total pore

volumes, respectively. Clearly, pore volume is not the sole indicator for effectiveness of depositing LiOH. Both BPL and RX 1.5 extra have over 90% microporosity, much higher than any of the other carbons. This result shows that micropores are not good for supporting large amounts of LiOH, likely due to significant pore blockage. The carbons SX Ultra and SX1G have similar degrees of microporsity but SX Ultra has significantly more pore volume and subsequently has much higher CO_2 capacity. SX Ultra and GSX have very similar total pore volumes and water saturated CO_2 capacities. SX Ultra has significantly more microporosity which, based on the low CO_2 capacities from BPL and RX 1.5 extra, should lead to reduced CO_2 capacity; however, this is not the case. SX Ultra has a much higher surface area than GSX, likely due to GSX having larger macropores and thereby limiting the amount of area that LiOH can be deposited onto. These results reveal that the ideal support for LiOH would have a high degree of mesoporosity with the pore diameter being large enough to prevent blockage but small enough to still have a large surface area to deposit onto. Based on this analysis, SX Ultra was singled out as a support for further study.

Table 6.3 BET surface area, pore volume, microporosity, and water saturated CO_2 capacity for 50 wt% LiOH deposited on different carbon supports.

Support	*Surface Area* (m^2/g)	*Pore Volume* (cm^3/g)	*% Micropores*	*CO_2 Capacity* (mol/kg)
RX 1.5 Extra	1523	0.82	94.4	1.59
SX Ultra	1081	0.78	49.1	3.36
GSX	719	0.75	29	3.31
SX1G	845	0.68	55.4	1.79
BPL	939	0.55	93.7	0.28

Figure 6.4 shows water saturated CO_2 capacities for different loadings of LiOH/SX Ultra. The samples tested were synthesized to be nominally 10, 20, 30, 40, and 50 wt% LiOH/SX Ultra. The CO_2 capacities increase linearly up to the 40 wt% sample and then plateau. Results between

different synthesis batches of each sample show good reproducibility. The plateau is an interesting result that could be caused by different factors. At some point increasing the LiOH content of a sample would completely fill all of the support pore space, thereby creating the same detrimental diffusion barriers that exist with pure LiOH pellets under high humidity. In this case, the plateau in capacity would be the result of a decrease in the adsorption efficiency of LiOH despite having a higher quantity of LiOH available. The plateau could also be the result of a maximum amount of LiOH that the synthesis method is capable of loading into the support.

To determine the cause of the plateau, elemental analysis of the Li content in the samples was performed. Table 6.4 gives the actual LiOH wt%, impregnation efficiency, CO_2 capacity under 100% relative humidity, and the CO_2 adsorption efficiency compared to the theoretical maximum. For the samples with lower LiOH loadings, only about 80% of the desired LiOH is actually deposited onto the support. This value further decreases for higher LiOH loadings. There is a maximum LiOH loading of approximately 25-30 wt% on Norit SX Ultra. Both the 40 and 50 wt% samples show this maximum loading, so both synthesis procedures make basically the same material, and reaching a maximum LiOH loading explains the plateau in CO_2 capacity at 3.4 mol/kg. Another interesting result is that for each loading, about 60% of the LiOH in the sample is used to adsorb CO_2 at 100% relative humidity.

Table 6.4 Elemental analysis results and lithium efficiency for CO_2 adsorption under saturated conditions.

Synthesis wt %	*Actual wt %*	*% expected*	*Capacity (mol/kg)*	*Li efficiency*
10	8.16	81.60	0.70	0.41
20	16.22	81.09	1.88	0.56
30	22.59	75.31	2.68	0.57
40	27.91	69.77	3.44	0.59
50	26.43	52.87	3.33	0.61

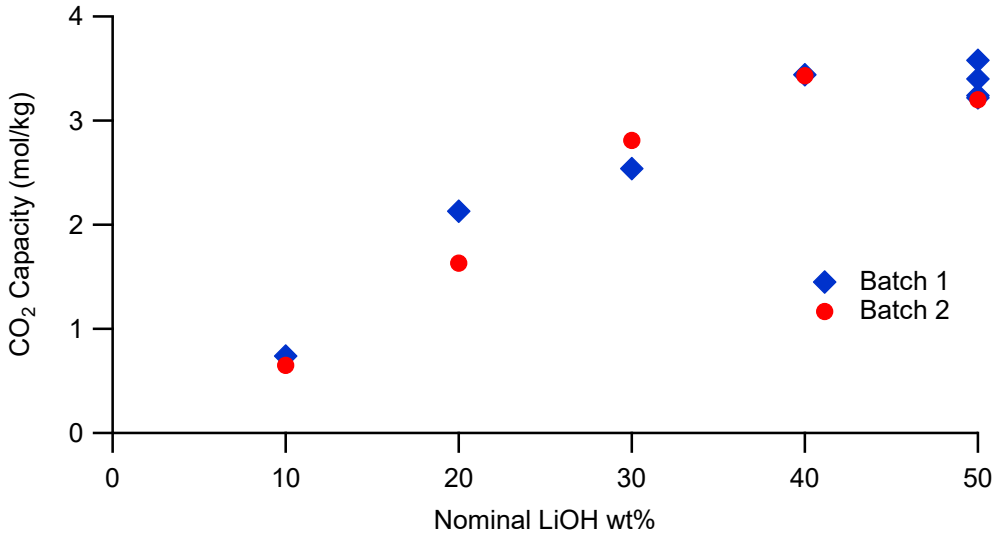

Figure 6.4 CO_2 capacities under water saturated conditions for samples of LiOH/SX Ultra synthesized with various LiOH loadings.

An important trend to study in these LiOH supported materials is the impact of relative humidity. The presence of water actually aids CO_2 adsorption on LiOH pellets until an excess of water limits adsorption efficiency.[14,15] Figure 6.5 shows CO_2 capacities at different relative humidity for the samples with the maximum loading of LiOH/SX Ultra. Under dry conditions, the CO_2 capacity is only 2.11 mol/kg. It increases with higher relative humidity to a maximum of approximately 4.5 mol/kg at 75% relative humidity before falling to 3.4 mol/kg under water saturated conditions. The increase in capacity in non-water saturated conditions shows that despite the deposition on porous supports, there are still diffusion barriers that prevent the complete use of the LiOH. The impact of diffusion was also seen upon adjusting flow rates. Increasing the feed stream flow rate to 10 sccm compared to 3 sccm resulted in a roughly 10% loss in CO_2 capacity under water saturated conditions. It should be noted, that even though there is still evidence of diffusion barriers in these new materials, the water saturated CO_2 adsorption efficiency of the supported LiOH is about 60% whereas the adsorption efficiency for pure LiOH pellets is below 20%.[14,15]

6.4 Conclusions

CO_2 adsorbents made from the deposition of LiOH into porous supports were tested using a breakthrough of a water saturated 1% CO_2 stream. Due to the highly basic conditions during the synthesis of the adsorbents, activated carbons were chosen as their chemical structure does not break down. Several carbons with varying pore sizes were tested and the best supports was deemed to be Norit SX Ultra due to a high degree a mesoporosity that prevents pore blockage but maintains high surface area. It was determined that the maximum amount of LiOH that can be successfully deposited in the pores is around 30 wt%. Under saturated water conditions, the highest CO_2

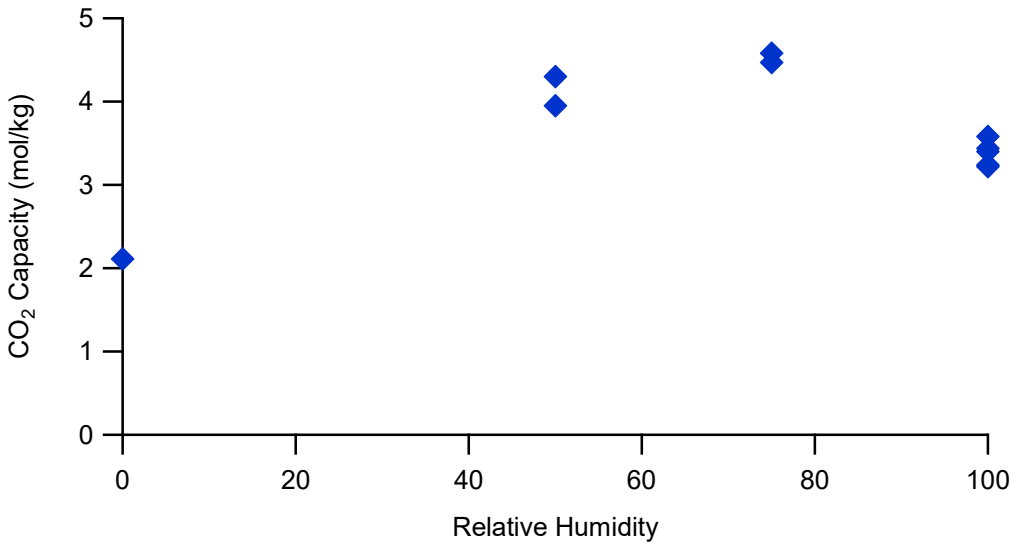

Figure 6.5 CO_2 adsorption capacities for the maximum loading of LiOH on SX Ultra at varying relative humidity.

capacity was recorded at 3.44 mol/kg which represents a 60% LiOH adsorption efficiency compared to the theoretical maximum.

References

1. Smith, J. W. H.; Romero, J. V.; Dahn, T. R.; Dunphy, K.; Croll, L. M.; Dahn, J. R. The effect of co-impregnated acids on the performance of Zn-based broad spectrum respirator. *J. Haz. Mater.* **2012**, 235, 279-285.
2. Pakseresht, S.; Kazemeini, M.; Akbarnejad, M. M. Equilibrium isotherms for CO, CO_2, CH_4, and C_2H_4 on the 5A molecular sieve by a simple volumetric apparatus. *Sep. Purif. Technol.* **2002**, 28, 53-60.
3. Lee, J. S.; Kim, J. H.; Kim, J. T.; Suh, J. K.; Lee, J. M.; Lee, C. H. Adsorption equilibria of CO_2 on zeolite 13X and zeolite X/activated carbon composite. *J. Chem. Eng. Data* **2002**, 47, 1237-1242.
4. Walton, K. S.; Abney, M. B.; LeVan, M. D. CO_2 adsorption in Y and X zeolites modified by alkali metal cation exchange. *Micro. Meso. Mater*. **2006**, 91, 78-84.
5. Mason, J. A.; Sumida, K.; Herm, Z. R.; Krishna, R.; Long, J. R. Evaluating metal-organic frameworks for post-combustion carbon dioxide capture via temperature swing adsorption. *Energy Environ. Sci.* **2012**, 4, 3030-3040.
6. Yazaydin, A. O.; Snurr, R. Q.; Park, T. H.; Koh, K.; Liu, J.; LeVan, M. D.; Benin, A. I.; Jakubczak, P.; Lanuza, M.; Galloway, D. B.; Low, J. L.; Willis, R. R. Screening of metal-organic frameworks for carbon dioxide capture from flue gas using a combined experimental and modeling approach. *J. Am. Chem. Soc.* **2009**, 131, 18198-18199.
7. Aprea, P.; Caputo, D.; Gargiulo, N.; Iucolano, F.; Pepe, F. Modeling carbon dioxide adsorption on microporous substrates: Comparison between Cu-BTC metal-organic framework and 13X zeolitic molecular sieve. *J. Chem. Eng. Data* **2010**, 55, 3655-3661.

8. Wang, Y.; LeVan, M. D. Adsorption equilibrium of binary mixtures of carbon dioxide and water vapor on zeolites 5A. *J. Chem. Eng. Data* **2010**, 55, 3189-3195.
9. Burtch, N. C.; Jasuja, H.; Walton, K. S. Water Stability and adsorption in metal-organic frameworks. *Chem. Rev.* **2014**, 114, 10575-10612.
10. Choi, S.; Gray, M. L.; Jones, C. W. Amine-Tethered Solid Adsorbents Coupling High Adsorption Capacity and Regenerability for CO_2 Capture from Ambient Air. *ChemSusChem* **2011**, 4, 628-635.
11. Yong, Z.; Mata, V.; Rodrigues, A. E. Adsorption of carbon dioxide at high temperature–a review. *Sep. Purif. Technol*. **2002**, 26, 195-205.
12. Kato, M.; Nakagawa, K.; Essaki, K.; Maezawa, Y.; Takeda, S.; Kogo, R.; Hagiwara, Y. Novel CO_2 Absorbents Using Lithium-Containing Oxide. *Int. J. Appl. Ceram. Tec.* **2005**, 6, 467-475.
13. Satyapal, S.; Filburn, T.; Trela, J.; Strange, J. Performance and properties of a solid amine sorbent for carbon dioxide removal in space life support applications. *Energy Fuels* **2001**, 15, 250-255.
14. Williams, D. D.; Miller, R. R. Effect of Water Vapor on the LiOH-CO_2 Reaction. Dynamic Isothermal System. *Ind. Eng. Chem. Fundam.* **1970**, 9, 454-457.
15. Boryta, D. A.; Maas, A. J. Factors influencing rate of carbon dioxide reaction with lithium hydroxide. *Ind. Eng. Chem. Process Des. Develop.* **1971**, 10, 489-494.
16. Mosqueda, H. A.; Vazquez, C.; Bosch, P.; Pfeiffer, H. Chemical sorption of carbon dioxide (CO_2) on lithium oxide (Li_2O). *Chem. Mater.* **2006**, 18, 2307-2310.
17. Cho, Y.; Lee, J.-Y.; Bokare, A. D.; Kwon, S. B.; Park, D.-S.; Jung, W.-S.; Choi, J.-S.; Yang, Y.-M.; Lee, J.-Y.; Choi, W. LiOH-embedded zeolite for carbon dioxide capture under ambient conditions. *J. Ind. Eng. Chem.* **2015**, 22, 350-356.

18. Janus, R.; Wach, A.; Kustrowski, P.; Dudek, B.; Drozdek, M.; Silvestre-Albero, A. M.; Rodriguez-Reinoso, F.; Cool, P. Investigation on the Low-Temperature Transformations of Poly (furfuryl alcohol) Deposited on MCM-41. *Langmuir* **2013**, 29, 3045-3053.
19. Kloetstra, K. R.; Bekkum, H. v. Base and acid catalysis by the alkali-containing MCM-41 mesoporous molecular sieve. *J. Chem. Soc., Chem. Commun.* **1995**, 1005-1006.
20. Xu, X.; Song, C.; Andresen, J. M.; Miller, B. G.; Scaroni, A. W. Preparation and characterization of novel CO_2 "molecular basket" adsorbents based on polymer-modified mesoporous molecular sieve MCM-41. *Micorpor. Mesopor. Mater.* **2003**, 62, 29-45.
21. Furtado, A. M. B.; Barpaga, D.; Mitchell, L. A.; Wang, Y.; DeCoste, J. B.; Peterson, G. W.; LeVan, M. D. Organoalkoxysilane-Grafted Silica Composites for Acidic and Basic Gas Adsorption. *Langmuir*, **2012**, 28, 17450-17456.

CHAPTER VII

CONCLUSIONS AND RECOMMENDATIONS

This dissertation focused on applying fundamental adsorption principles to measure and understand adsorption equilibria and mass transfer in specific applications of interest. Various experimental techniques were used to characterize the adsorbents and to measure adsorption and diffusion. The adsorbents studied had considerably different morphologies including amorphous materials with wide pore size distributions, crystalline materials with very uniform pores, bidisperse materials created from pelleted powders, and biphasic materials in which an active adsorbent phase was dispersed on a porous support. Various adsorbates were studied for applications ranging from separation of a dilute feed to high pressure storage of pure components.

The principle findings of this research are:

Steric effects on hydrocarbon diffusion in BPL activated carbon

- A concentration-swing frequency response apparatus was used to study diffusion rates of several C_{10} hydrocarbons with various ring and branched structures in BPL activated carbon.
- Micropore diffusion was the rate-limiting mass transfer mechanism for each adsorbate at various concentrations with micropore diffusion coefficients that are highly concentration dependent. The lower limit of diffusion for C_{10} hydrocarbons in BPL activated carbon is about 10^{-11} m^2/s, although values can be several orders of magnitude faster at higher concentrations.
- The order from fastest to slowest diffusion was n-decane > limonene > perfluorodecalin >

decalin > α-pinene.

- Size exclusion based sieving effects were not observed as the wide pore size distribution of BPL activated carbon was larger than any molecular dimensions; however, the steric factors of molecular rigidity and compactness showed good correlation with diffusivity.

CO_2 diffusion in large Cu-BTC crystals

- Properties of large millimeter size single crystals were measured by XRD, BET, TGA, and CO_2 isotherms and agree well with Cu-BTC powders.
- The increased length scale of the microporous domain makes diffusion measurements easier as it limits the impact of multiple mass transfer mechanisms. CSFR experiments verified micropore diffusion as the rate controlling diffusive mechanism.
- Diffusion coefficients measured at varying concentrations show very little dependence on loading up to about 0.1 bar, with measured diffusion coefficients of approximately 5×10^{-10} m^2/s.

CO_2 and ethane diffusion in bidisperse pellets of UiO-66

- Two analogs of a MOF, UiO-66, were pelletized at different pressures and thicknesses, and tested for mass transfer limitations of CO_2 and ethane using a CSFR apparatus.
- Regressed isotherm slopes and adsorption isotherms both showed that capacities were much higher for UiO-66-NH_2 compared to the unfunctionalized UiO-66 and that pressing the pellets at higher pressures had a slightly negative impact on capacity.
- Macropore diffusion was determined to be the rate-limiting mass transfer mechanism and measured macropore diffusion coefficients were greatly impacted by the pelletization pressure and were largely independent of the adsorbate.

Oxygen storage in MOFs

- Three MOFs were tested for oxygen storage by measuring high pressure oxygen isotherms.
- HKUST-1 and NU-125 showed capacities comparable to the current state of the art carbons and greater than zeolites.
- NU-125 gave an increase in working capacity of approximately 130% over an empty cylinder.
- The MOFs showed good stability and retained capacity after repeated charging and discharging cycles.

Novel adsorbents for a CO_2 scrubber in a tactical rebreather

- CO_2 adsorbents made from the deposition of LiOH into porous supports were evaluated using breakthrough testing with of a water saturated 1% CO_2 stream to simulate conditions in a tactical rebreather.
- Several carbons with varying pore sizes were tested, and the best support was deemed to be Norit SX Ultra due to a high degree of mesoporosity that prevents pore blockage but maintains high surface area. It was determined that the maximum amount of LiOH that can be successfully deposited in the pores is around 30 wt%.
- Under saturated water conditions, the highest CO_2 capacity was 3.44 mol/kg, which represents a 60% LiOH adsorption efficiency compared to the theoretical maximum.

Some recommendations that may provide potential opportunities to extend this work include:

- Many filtration applications use activated carbons impregnated with metals or other functionalities to provide chemical reactivity as a means of removing toxins instead of relying purely on physisorption. The strong concentration dependence of the hydrocarbon diffusion shows the impact of surface forces. Impregnants may add to these forces or cause pore blockage that could impact diffusion in these materials compared to unimpregnated samples. Testing impregnated activated carbons for diffusion may be a useful study in the future.
- Only the diffusion of non-reactive adsorbates was tested in the UiO-66 pellets. Due to the ability to be easily functionalized by different moieties, UiO-66 pellets could prove useful for the removal of toxic substances through reaction. However, molecules that are chemically bound by reaction to the surface may introduce new diffusive challenges. Diffusion of reactive gases could be studied in the future.
- For oxygen storage in MOFs, only parent MOF materials were used for adsorption. Because MOFs can be easily functionalized through processes such as solvent assisted ligand incorporation (SALI), solvent assisted ligand exchange (SALE), or cation exchange, different moieties can be incorporated to target specific adsorbates. The parent MOFs, Cu-BTC and NU-125, could be functionalized to further increase the high adsorption capacities of oxygen.